

# The X-ray Properties of Five Galactic Supernova Remnants Detected by the *Spitzer* GLIMPSE Survey

Thomas G. Pannuti

*Space Science Center, Department of Earth and Space Sciences, Morehead State  
University, 235 Martindale Drive, Morehead, KY 40351*

t.pannuti@moreheadstate.edu

Jeonghee Rho

*SETI Institute and SOFIA Science Center, NASA Ames Research Center, MS 211-3,  
Mountain View, CA 94035*

jrho@sofia.usra.edu

Craig O. Heinke

*Department of Physics, CCIS 4-183, University of Alberta, Edmonton, AB T6G 2E1,  
Canada*

heinke@ualberta.ca

and

William P. Moffitt

*Space Science Center, Department of Earth and Space Sciences, Morehead State  
University, 235 Martindale Drive, Morehead, KY 40351*

w.moffitt@moreheadstate.edu

## ABSTRACT

We present a study of the X-ray properties of five Galactic supernova remnants (SNRs) – Kes 17 (G304.6+0.1), G311.5–0.3, G346.6–0.2, CTB 37A (G348.5+0.1) and G348.5–0.0 – that were detected in the infrared by Reach et al. (2006) in an analysis of data from the Galactic Legacy Infrared Mid-Plane Survey Extraordinaire (GLIMPSE) that was conducted by the *Spitzer* Space Telescope. We present and analyze archival *ASCA* observations of Kes 17, G311.5–0.3 and G346.6–0.2, archival *XMM-Newton* observations of Kes 17, CTB 37A and

G348.5–0.0 and an archival *Chandra* observation of CTB 37A. All of the SNRs are clearly detected in the X-ray possibly except for G348.5–0.0. Our study reveals that the four detected SNRs all feature center-filled X-ray morphologies and that the observed emission from these sources is thermal in all cases. We argue that these SNRs should be classified as mixed-morphology SNRs (MM SNRs): our study strengthens the correlation between MM SNRs and SNRs interacting with molecular clouds and suggests that the origin of mixed-morphology SNRs may be due to the interactions between these SNRs and adjacent clouds. Our *ASCA* analysis of G311.5–0.3 reveals for the first time X-ray emission from this SNR: the X-ray emission is center-filled within the radio and infrared shells and thermal in nature ( $kT \sim 0.98$  keV), thus motivating its classification as an MM SNR. We find considerable spectral variations in the properties associated with the plasmas of the other X-ray-detected SNRs, such as a possible overabundance of magnesium in the plasma of Kes 17. Our new results also include the first detailed spatially-resolved spectroscopic study of CTB 37A using *Chandra* as well as a spectroscopic study of the discrete X-ray source CXOU J171428.5–383601, which may be a neutron star associated with CTB 37A. Finally, we also estimate such properties as electron density  $n_e$ , radiative age  $t_{rad}$  and swept-up mass  $M_X$  for each of the four X-ray-detected SNRs. Each of these values are comparable to archetypal mixed-morphology SNRs like 3C 391 and W44. In an analysis of the spectrum of Kes 17, we did not find evidence of over-ionization unlike other archetypal mixed-morphology SNRs like W28 and W44.

*Subject headings:* ISM: individual objects (SNR 304.6+0.1, SNR 311.5-0.3, SNR 346.6-0.2, SNR 348.5+0.1, SNR 348.5-0.0) – ISM: supernova remnants – X-rays: ISM

## 1. Introduction

Reach et al. (2006) presented a search for infrared counterparts to Galactic supernova remnants (SNRs) that were sampled by the Galactic Legacy Infrared Mid-Plane Survey Extraordinaire (GLIMPSE) Legacy survey (Benjamin et al. 2003). The GLIMPSE survey imaged the inner Galactic plane – specifically the Galactic latitude and longitude ranges of  $|b| < 1^\circ$  and  $10^\circ < |l| < 65^\circ$ , respectively – at four wavelength bands (3.6, 4.5, 5.8 and  $8.0 \mu\text{m}$ ) with the Infrared Array Camera (IRAC) (Fazio et al. 2004) aboard the *Spitzer Space Telescope* (Werner et al. 2004). The results presented by Reach et al. (2006) were very intriguing: of the 95 SNRs known (at the time) that were sampled by GLIMPSE, eighteen

SNRs were detected (many for the first time) and the infrared emission from these sources typically coincided (at least partially) with known radio structures. Reach et al. (2006) also presented simple models to generate template colors in the IRAC bands for the primary emission mechanisms expected from SNRs. These primary emission mechanisms include the following: (i) *molecular* line colors that were estimated using a three temperature component  $\text{H}_2$  excitation model based on numerous  $\text{H}_2$  lines detected toward IC 443 (Rho et al. 2001), (ii) *ionized* gas line colors that were estimated based on hydrogen recombination as well as the dominant fine-structure lines of iron and argon (assuming solar abundances) and (iii) interstellar medium (ISM) polycyclic aromatic hydrocarbon (PAH) colors that were estimated using a spectrum of the reflection nebula NGC 7023. In their analysis, Reach et al. (2006) found that the spectra of nine SNRs, three SNRs and four SNRs were dominated by molecular lines, fine-structure lines and PAHs, respectively. The spectra of the remaining SNRs indicated a mixture of ionic and molecular shocks, suggesting a combination of shock types.

Interestingly, many of the SNRs detected with IRAC also appear to be interacting with relatively dense gas. Evidence for such interactions is the excess emission detected from these SNRs at a wavelength of  $4.5\ \mu\text{m}$ : such an excess is likely produced by  $\text{H}_2$  and CO line emission and such line emission is associated with molecular shocks. Furthermore, follow-up spectroscopy observations conducted with the Infrared Spectrograph (IRS) aboard *Spitzer* (Houck et al. 2004) revealed  $\text{H}_2$  emission from all of the SNRs with IRAC by the survey conducted by Reach et al. (2006), suggesting that each of these SNRs are interacting with molecular clouds (Hewitt et al. 2009; Andersen et al. 2011). We shall refer to these SNRs as molecular SNRs for the remainder of the paper.

Several molecular SNRs are detected in the X-ray (see Vink (2012) for a review of X-ray emission from SNRs) and all of them belong to the class of sources known as mixed-morphology SNRs (MM SNRs). The distinguishing characteristics of MM SNRs are a center-filled thermal X-ray morphology paired with a well-defined radio shell (Rho & Petre 1998). Examples of well-known MM SNRs include W28, W44 and 3C 391: each of these SNRs was observed in the infrared with the Long Wavelength Spectrometer (LWS; Clegg et al. 1996) aboard the *Infrared Space Observatory* (ISO) (Kessler et al. 1996) and  $\text{H}_2$  emission was detected from all three SNRs (Reach & Rho 2000). Many of the molecular SNRs detected by Reach et al. (2006) have not been well-studied in the X-ray, probably because the Galactic column densities toward these sources are elevated ( $N_H \sim 10^{22}\ \text{cm}^{-2}$ ), causing them to appear to be faint in the X-ray. In this paper we describe the X-ray properties of five molecular SNRs detected by Reach et al. (2006): Kes 17 (G304.6+0.1), G311.5–0.3, G346.6–0.2, CTB 37A (G348.5+0.1) and G348.5–0.0. For this study, we use data from archival observations made with *ASCA*, *Chandra* and *XMM – Newton*. These SNRs had been studied

almost exclusively in the radio before the infrared observations made with *Spitzer*: they have not been detected in the optical most likely because of the high extinction toward these sources. We note that three of these SNRs (Kes 17, G346.6–0.2 and CTB 37A) have been the subjects of pointed *Chandra*, *XMM-Newton* and *Suzaku* observations that have been described and analyzed in separate publications (Aharonian et al. 2008; Combi et al. 2010; Sezer et al. 2011a,b; Gök & Sezer 2012; Yamauchi et al. 2013). Serendipitous observations made of G346.6–0.2, CTB 37A and G348.5–0.0 with *ASCA* have also been described by Yamauchi et al. (2008). In this paper, we present new analyses of the *ASCA* observations of Kes 17 and G311.5–0.3 (including the first reported detection of X-ray emission from this SNR) and a spatially-resolved spectroscopic analysis of the *Chandra* observation of CTB 37A. We will compare the results of our analyses with the results for all of the SNRs with the previously-published papers mentioned above.

The organization of this paper may be described as follows: the observations as conducted by each observatory and the subsequent data analyses are described in Section 2. In Section 3 we present a description of the five SNRs in our sample and the X-ray results – both imaging and spectroscopic – for each SNR. A summary of the plasma conditions of these sources as inferred from these X-ray observations is presented in Section 4. In Section 5 we discuss the phenomenon of overionization in mixed-morphology SNRs and comment on its applicability to the SNRs in our sample. In Section 6 we compare the properties of the SNRs in our sample and discuss the implications for SNR evolution. Finally, the conclusions reached by this work are presented in Section 7.

In Table 1 we list general properties – including RA (J2000.0), Dec (J2000.0), angular diameter, distance, physical size, column density  $N_H$  and optical extinction  $A_V$  – of the five SNRs considered in the present paper.

## 2. Observations and Data Reduction

### 2.1. X-ray Observations

#### 2.1.1. *ASCA* Observations and Data Reduction

All five of the SNRs studied in the present paper were sampled (either directly by pointed observations or indirectly by pointed observations that targeted other sources but included the SNR within the field of view) by the Advanced Satellite for Cosmology and Astrophysics (*ASCA* – Tanaka et al. (1994)). The instruments carried by *ASCA* included two Solid-State Imaging Spectrometers denoted as SIS0 and SIS1 (Burke et al. 1991) and two

Gas Imaging Spectrometers denoted as GIS2 and GIS3 (Makishima et al. 1996; Ohashi et al. 1996): these instruments were located at the focal planes of four thin-foil X-ray telescopes (XRT – Serlemitsos et al. (1995)). A single GIS unit sampled a field of view  $\sim 50'$  in diameter while a single SIS unit sampled a field of view approximately  $44' \times 44'$  in size. The nominal full-width at half-maximum (FWHM) angular resolution of both the GIS and the SIS at 1 keV was approximately 1 arcminute.

Data for all of the *ASCA* observations considered in the present paper were extracted from the archive located at the High Energy Astrophysics Science Archive Research Center (HEASARC<sup>1</sup>) and reduced using standard tools in the FTOOLS package<sup>2</sup>. However, only the observations of the Kes 17, G311.5–0.3 and G346.6–0.2 yielded enough counts from the particular SNRs for detailed spectral fitting. In the cases of the SNRs CTB 37A and G348.5–0.0 which appear adjacent to each other in the sky, these particular sources were located too close to the edges of the GIS fields of view to extract useful spectra. In addition, as noted by Yamauchi et al. (2008), contaminating stray flux from bright X-ray sources located out of the field of view and south of these two SNRs made it difficult to isolate their X-ray emission (see Section 3.5 for more details, particularly about our attempt to extract X-ray spectra for G348.5–0.0 from the *XMM-Newton* observation, which also contained contaminating stray X-ray flux). The angular extents of the three remaining SNRs for which we extracted *ASCA* spectra (that is, Kes 17, G311.5–0.3 and G346.6–0.2) were compact enough to fit within the fields of view of the GIS2 and the GIS3: in the case of Kes 17, the SNR was also compact enough to fit entirely within the fields of view of the SIS0 and the SIS1. Therefore, we also extracted SIS spectra of this SNR as well. Unfortunately the signal-to-noise of the extracted SIS1 source spectrum of Kes 17 was too poor for any detailed spectral fitting, so we do not consider it further in this paper. The data reduction was accomplished using another program available from the HEASARC site, `xselect` (Version 2.4b): standard REV2 screening was applied to both the GIS and SIS datasets. We used `xselect` to extract GIS2 and GIS3 spectra for Kes 17, G311.5–0.3 and G346.6–0.2: in the case of Kes 17, we also used `xselect` to extract an SIS0 spectrum as well. For spectral analysis, the standard GIS2 and GIS3 response matrix files (RMFs) were used while the FTOOL `sisrmg` was used to generate an RMF for the SIS0 spectrum of Kes 17. Lastly, the FTOOL `ascaarf` was used to create ancillary response files (ARFs) for each extracted GIS and SIS spectra. In Table

---

<sup>1</sup>HEASARC is a service of the Laboratory for High Energy Astrophysics (LHEA) at the National Aeronautics and Space Administration Goddard Space Flight Center (NASA/GSFC) and the High Energy Astrophysics Division of the Smithsonian Astrophysical Observatory (SAO). For more information on HEASARC, please see <http://heasarc.gsfc.nasa.gov>.

<sup>2</sup>[http://heasarc.gsfc.nasa.gov/docs/software/floods/ftools\\_menu.html](http://heasarc.gsfc.nasa.gov/docs/software/floods/ftools_menu.html)

2, we present a summary of the *ASCA* observations made of the SNRs that we consider in this paper.

### 2.1.2. *XMM-Newton* Observations and Data Reduction

While all five of the SNRs considered in the present paper were sampled (either directly by pointed observations or indirectly by pointed observations that targeted other sources but included the SNR within the field of view) by the *XMM-Newton* Observatory (Jansen et al. 2001), in the cases of two SNRs – G311.5–0.3 and G346.6–0.2 – the source was located so far from the centers of the fields of view and the exposure times of the observations were so short that no useful spectral data could be extracted for these SNRs by these observations. We therefore only consider the observations made by *XMM-Newton* of the other three SNRs in our study, namely Kes 17, CTB 37A and G348.5–0.0. The main science instruments aboard *XMM-Newton* are the pn-CCD camera (Strüder et al. 2001) and the Multi-Object Spectrometer cameras (Turner et al. 2001): we will refer to these instruments as the PN, MOS1 and MOS2 for the remainder of the paper and note that both of these instruments comprise the European Photon Imaging Camera (EPIC). The fields of view of the PN, MOS1 and MOS2 cameras are approximately 30 arcminutes and the nominal angular FWHM at 1 keV of all three cameras is  $\sim 6''$ .

Data for the observations was downloaded from the on-line *XMM-Newton* data archive<sup>3</sup>. The observations were reduced using standard tools in the Science Analysis System (SAS – Gabriel et al. (2004)) software package Version 11.0.0. The tool `emchain` was used to process data from the observations made by the MOS1 and the MOS2 cameras and the tool `mos-filter` was used to filter out background flares during the observation and to identify good time intervals. Similarly, the tool `epchain` was used to process data from the observations made by the PN camera and the tool `pn-filter` was used to identify background flares during the observation and to identify good time intervals. To extract MOS1, MOS2 and PN spectra for both source and background regions, the tool `evselect` was used and the extracted spectra were grouped to a minimum of 15 counts per channel. Subsequently, the tool `backscale` was run to compute the proper value for the BACKSCAL keyword in the extracted spectra. Finally, the tools `rmfgen` and `arfgen` were used to generate the RMFs and ARFs (respectively) for the spectra which are necessary for spectral fitting. In Table 3, we present a summary of the *XMM-Newton* observations made of the SNRs that we consider in this paper.

---

<sup>3</sup><http://xmm.esac.esa.int/xsa/>



### 2.1.3. *Chandra Observations and Data Reduction*

One of the SNRs studied in the present paper – CTB 37A – was the target of a pointed observation made with the *Chandra* X-ray Observatory (Weisskopf et al. 2002): the corresponding ObsID of this observation is 6721 and data for this observation was downloaded from the on-line *Chandra* data archive<sup>4</sup>. The observation of CTB 37A was conducted in VERY FAINT Mode on 2006 October 7 with the Advanced CCD Imaging Spectrometer (ACIS) at a focal plane temperature of  $-120^{\circ}$  C. The entire angular extent of the X-ray emitting plasma associated with SNR fit within the field of view of the ACIS-I array and the geometric center of this angular extent aligned roughly with the aimpoint of the observation. Properties of the ACIS chips (including the ACIS-I array) have been described by Garmire et al. (2003): to summarize, the ACIS-I array is composed of four front-illuminated CCD chips arranged in a  $2 \times 2$  array. Each chip has a field of view of  $8.3' \times 8.3'$ : thus, the entire array has a field of view of  $17' \times 17'$ . The chips are sensitive to photons with energies ranging from 0.4 to 10.0 keV and the full-width at half-maximum (FWHM) angular resolution of each chip at 1 keV is  $1''$ . The maximum effective collecting area of each chip is  $525 \text{ cm}^2$ : this maximum corresponds to photons with energies of 1.5 keV. Finally, the spectral resolution of each chip at 1 keV is 56.

The dataset from this observation was reduced using the *Chandra* Interactive Analysis of Observations (CIAO<sup>5</sup>) software package Version 4.3 (CALDB Version 4.4.1). Standard processing was applied to this dataset: to generate a new event file, the CIAO tool `acis_process_events` was used. This tool applies the latest temperature-dependent charge transfer inefficiency (CTI) correction, the latest time-dependent gain adjustment as well as the latest gain map: `acis_process_events` also flags bad pixels and applies background cleaning for datasets created in VERY FAINT mode, which is the case of the observation considered here. The new event file was further filtered for bad grades (that is, events which had GRADE values of 1, 5 or 7 were excluded) and proper status columns: in addition, the good time interval supplied by the pipeline was also applied. Finally, the event file was also screened for background flare activity using the CIAO tool `chips`<sup>6</sup>: background flares did not affect the observation at a significant level. The resulting total effective exposure time of the observation was 19.7 ks: in Table 4 we present a summary of the parameters of this observation.

---

<sup>4</sup><http://cda.harvard.edu/chaser/>.

<sup>5</sup>See Fruscione et al. (2006) and <http://cxc.harvard.edu/ciao/>.

<sup>6</sup><http://cxc.harvard.edu/chips/index.html>.

The CIAO tool `specextract` was used to extract spectra from different regions of the X-ray emitting plasma associated with CTB 37A (along with selected background regions located outside of the X-ray emitting plasma). In addition to extracting spectra for source and background regions, `specextract` also creates weighted ARFs and RMFs by initiating the CIAO tools `mkwarf` and `mkrmf`, respectively. Finally, `specextract` also initiates the CIAO tool `dmgroup` to group the source and background spectra: in the case of our spectral analysis, the spectra were all grouped to a minimum of 15 counts per channel. We used the CIAO wavelet detection routine `wavdetect` (Freeman et al. 2002) to identify unrelated discrete X-ray sources detected along the line of sight toward CTB 37A by the *Chandra* observation: such sources may contribute undesired contaminating flux that interferes with spectral analyses of the SNR itself. When regions of spectral extraction were defined, care was taken to exclude flux from the positions of these detected sources so that the analyzed spectra more faithfully represented the true emission from the SNR. The locations of these source and background regions as well as the analysis of these spectra are presented in Section 3.4.1.

## 2.2. Infrared Observations

We used *Spitzer* IRAC and MIPS images from Reach et al. (2006) and Andersen et al. (2011), respectively, of the five SNRs considered in this paper to compare the infrared morphologies of these sources with their X-ray and radio morphologies. For details on the IRAC and MIPS observations of these SNRs and the subsequent data processing and analyses of the images, the reader is referred to those papers.

## 2.3. Radio Observations

As part of our study, we also included radio maps of each SNR that were made at a frequency of 843 MHz by the Molonglo Observatory Synthesis Telescope (MOST<sup>7</sup>, Mills et al. 1981; Robertson 1991): these maps have been consolidated into the MOST Supernova Remnant Catalogue (MSC<sup>8</sup>). We obtained publicly-available reduced radio maps for each SNR

---

<sup>7</sup>The MOST is operated by The University of Sydney with support from the Australian Research Council and the Science Foundation for Physics within The University of Sydney.

<sup>8</sup><http://www.physics.usyd.edu.au/sifa/Main/MS>.



from the MGPS Web Page<sup>9</sup> for the purposes of the present research. The MSC contains known southern Galactic SNRs located within the area  $245^\circ \leq \ell \leq 355^\circ$ ,  $|b| \leq 1.5^\circ$  that were observed with the MOST during a survey conducted at the frequency of 843 MHz of the southern Galactic plane (Whiteoak & Green 1996). The angular resolution attained by these observations was  $43'' \times 43''$  csc  $\delta$ , the sensitivity was approximately 1-2 mJy/beam ( $1\sigma$ ) and the positional accuracy was 1-2''. For more information about MOST, MGPS and these observations the reader is referred to the above references.

### 3. Results and Discussion

We now present an analysis of the X-ray properties of each SNR. All spectra were analyzed using the *XSPEC* software package (Arnaud 1996) Version 12.6.0q.

#### 3.1. Kes 17 (G304.6+0.1)

Kes 17 (G304.6+0.1) was first identified as a discrete radio source by the survey conducted by Kesteven (1968a) at a frequency of 408 MHz with the Molonglo Cross Telescope. It was later classified as a radio SNR by Kesteven (1968b) based on its measured non-thermal radio spectral index ( $\alpha = -0.77^{10}$ ). An 843 MHz map of this SNR presented by Whiteoak & Green (1996) based on observations made with the MOST reveal an incomplete shell-like morphology with bright southern and northwestern rims: a gap in the radio shell is seen toward the northeastern boundary. Whiteoak & Green (1996) measured the angular extent of Kes 17 to be 8 arcminutes and reported an integrated flux density at 843 MHz for the SNR of 18 Jy. Frail et al. (1996) reported on the detection of hydroxyl (OH) maser emission at 1720 MHz from Kes 17 based on observations made with the Parkes 64-meter telescope. Based on HI absorption measurements along the line of sight to this source, Caswell et al. (1975) estimated a minimum distance to Kes 17 of 9.7 kpc: we will adopt this distance to this SNR for the remainder of this paper. Previously published analyses of X-ray observations of Kes 17 have been presented by Combi et al. (2010) and Gök & Sezer (2012) (who examined *XMM-Newton* and *Suzaku* observations, respectively): we compare our analyses with the results from those two papers in Section 3.1.2. Finally, Wu et al. (2011) reported

---

<sup>9</sup><http://www.astrop.physics.usyd.edu.au/MGPS/>.

<sup>10</sup>Here and for the remainder of the paper, we will adopt the convention for the measured radio spectral index  $\alpha$  to be defined as  $S_\nu \propto \nu^\alpha$ .

the detection of  $\gamma$ -ray emission from Kes 17 based on observations made by the Large Area Telescope (LAT) aboard the *Fermi*  $\gamma$ -ray Space Telescope (Atwood et al. 2009).

### 3.1.1. *ASCA and XMM-Newton Observations of Kes 17 (G304.6+0.1)*

In Figure 1 we present an *ASCA* GIS2 image of Kes 17 over the energy range from 0.7 to 10 keV. Kes 17 was offset by approximately seven arcminutes from the center of the field of view of the GIS detectors when the observation was conducted. Radio emission (as detected by the MOST at 843 MHz) is plotted as contours overlaying the X-ray emission. The observed emission is broadly contained within the radio shell but the poor angular resolution of the X-ray observation prevents a detailed description of the morphology of the X-ray emission. In Figure 2 we present an *ASCA* SIS0 image of Kes 17 (again, the radio emission from the SNR is shown with contours): in the GIS and SIS images, it is clear to see that the X-ray emission is contained within the radio shell and that the bright radio rims (as seen toward the southern and western portions of the SNR) are X-ray faint. We extracted GIS2, GIS3 and SIS0 spectra for Kes 17 using the extraction regions indicated with blue circles in Figures 1 and 2. For the GIS2 and GIS3, we used a source region approximately 5.5 arcmin radius and a background region approximately 9 arcmin in radius from a portion of the field of view away from the location of Kes 17 itself. For the SIS0, we extracted a source spectrum from a region approximately 5.5 arcmin in radius: because this source region filled virtually the entire field of view of the SIS0 chip, we extracted a background spectrum from a SIS0 blank sky observation. We fit the extracted source spectra with the thermal models APEC (Astrophysical Plasma Emission Code – see Foster et al. 2012) and NEI (Non-Equilibrium Ionization – see Borkowski et al. 2001): satisfactory fits were obtained using these models. Because a statistically acceptable fit was obtained with the APEC model (which describes a plasma in collisional ionization equilibrium – CIE) and because the ionization timescale parameter  $\tau$  derived for the NEI fit is rather high ( $\tau \sim 10^{13}$  s cm $^{-3}$  with lower limits of approximately  $\tau \sim 10^{10}$  -  $10^{11}$  s cm $^{-3}$ ) we conclude that the X-ray-emitting plasma associated with Kes 17 is in CIE. For the spectral fits for all datasets considered in this paper, the photoelectric absorption model PHABS will be used to account for Galactic photoelectric absorption along the lines of sight to the SNRs.

The quality of the fits (as measured by the  $\chi^2_\nu$  statistic) were improved in both cases if we allowed the abundance parameter to vary: in each case, the derived abundance was sub-solar (approximately 0.2). To investigate the possibility of variations in the abundances of particular elements, we also fitted the extracted spectra with the thermal model VAPEC – this model has as free parameters the abundances of particular elements. We generated

two acceptable fits with the VAPEC model: in the first fit, we found marginal evidence for enhancement in the abundance of magnesium ( $\text{Mg}=2.38^{+4.32}_{-1.58}$  – all quoted errors in the present paper for fit parameters correspond to 90% confidence levels) while the abundances of other elements remained frozen to solar values. In the second fit, we found evidence for subsolar abundances for silicon and sulfur ( $\text{Si}=0.47^{+0.27}_{-0.19}$  and  $\text{S}=0.21(<0.56)$ ) while the abundances of the other elements were left frozen to solar values. For all of our fits, both the column density  $N_H$  and the temperature  $kT$  parameters remained broadly consistent (approximately  $N_H \sim 3\text{--}4 \times 10^{22} \text{ cm}^{-2}$  and  $kT \sim 0.5\text{--}0.7 \text{ keV}$ ).

In Figures 3 we present the extracted GIS2, GIS3 and SIS0 spectra of Kes 17 as fit with the PHABS×APEC model with variable abundance and in Figure 4 we present confidence contour plots (namely  $N_H$  versus  $kT$  and  $kT$  versus abundance) for this fit. In Table 5 we present a summary of all of the spectral fits to the extracted *ASCA* spectra of Kes 17. Confidence contour plots for the  $N_H$ ,  $kT$  and the abundance parameters for the PHABS×APEC fit are presented in Figure 4.

In Figure 5 we present an *XMM-Newton* MOS1 image of Kes 17: once again, radio emission from the SNR is plotted with contours. With an angular resolution of approximately  $6''$ , the *XMM-Newton* observation of Kes 17 has yielded the highest angular resolution image ever produced of this SNR. Inspection of this image clearly shows that the diffuse X-ray emitting plasma is enclosed by the radio shell and that the bright radio rims are X-ray dim. Such a contrasting X-ray and radio morphology of this SNR strongly indicates that it belongs to the well-known class of SNRs known as the mixed-morphology SNRs (Rho & Petre 1998). We extracted MOS1, MOS2 and PN spectra of Kes 17 using a source extraction region approximately 4 arcminutes in radius and centered on the nominal center of the X-ray-emitting plasma: a background spectrum was extracted from an annulus surrounding the source extraction region and with a thickness of approximately 1 arcminute (the locations of these extraction regions are indicated in Figure 5). We then fit the extracted spectra with the same thermal models used in analyzing the extracted *ASCA* spectra: once again, statistically-acceptable fits were derived with the APEC and NEI models. In agreement with the analysis of the *ASCA* spectra, the derivation of statistically-acceptable fits with the APEC model and a high derived ionization timescale with the NEI model ( $\tau = 3.70^{+6.30}_{-1.70} \times 10^{11} \text{ s cm}^{-3}$ ) imply that the X-ray emitting plasma is close to CIE. In contrast to our fits derived in analyzing the *ASCA* spectra, thawing the elemental abundance as a free parameter in the APEC model still returns a value of the abundance which is broadly consistent with a solar value ( $0.53^{+0.77}_{-0.23}$ ) and did not improve the quality of the fit.

Extending our prior analysis of the *ASCA* spectra of Kes 17, in analyzing the extracted *XMM-Newton* spectra we also searched for variations in the abundances of particular el-

elements by using the VAPEC model. We again first fit the spectra with the magnesium abundance thawed and the abundances of the other elements frozen to solar values. Separately, we fit the spectra again with the VAPEC model but this time with the abundances of silicon and sulfur thawed and the abundances of the other elements frozen to solar values. In the case of the latter fit, the abundances of silicon and sulfur were both broadly consistent with solar values ( $\text{Si}=0.79^{+0.51}_{-0.27}$  and  $\text{S}=0.71^{+0.49}_{-0.29}$ ) but in the former case we again find marginal evidence for an overabundance of magnesium ( $\text{Mg}=2.75^{+2.20}_{-1.70}$ ). We also note that for all of our fits with thermal models, the values for both  $N_H$  and  $kT$  remain broadly similar (that is,  $N_H \sim 3 \times 10^{22} \text{ cm}^{-2}$  and  $kT \sim 0.80\text{--}1.10 \text{ keV}$ ). Finally, we fit the extracted spectra using the VAPEC model with the abundances of magnesium, silicon and sulfur all thawed: this new fit did not yield a significant improvement in the value of  $\chi^2_\nu$ . If the detection of an overabundance of magnesium in the X-ray emitting plasma associated with Kes 17 is verified, this SNR may be the newest member of the class of mixed-morphology SNRs which feature ejecta-dominated emission: another example of such a source is the mixed morphology SNR CTB 1, which was shown to feature an overabundance of oxygen in spectra extracted from a *Chandra* observation of the SNR (Pannuti et al. 2010).

In Figure 6 we present the MOS1, MOS2 and PN spectra of Kes 17 as fitted with the PHABS×APEC model as well as a confidence contour plot for column density  $N_H$  and temperature  $kT$  for this fit. In Table 6 we provide a summary of the fits to the extracted MOS1, MOS2 and PN spectra of Kes 17. In Figures 7 and 8 we present multi-wavelength images – X-ray, radio and infrared (namely *Spitzer* IRAC and MIPS images) – of this SNR.

### 3.1.2. Discussion of X-ray Properties of Kes 17

We first describe prior analyses made of the X-ray properties of Kes 17. Combi et al. (2010) presented a study of a pointed *XMM-Newton* observation of Kes 17 that included an analysis of MOS1, MOS2 and PN spectra of this SNR: we have analyzed this same observation in the present paper. Those authors divided the SNR into three regions and extracted spectra for each region while we have considered just the spectra of the entire diffuse emission. Combi et al. (2010) fit the extracted spectra using the absorption model WABS (Morrison & McCammon 1983) coupled with the non-equilibrium ionization model with constant temperature PSHOCK (Mazzotta et al. 1998) and a power law model with a photon index  $\Gamma$  (defined such that  $E^{-\Gamma}$ ). In addition, Combi et al. (2010) allowed the abundance of the PSHOCK model to vary. The values for  $N_H$ ,  $kT$ , abundances,  $\tau$ , and  $\Gamma$  obtained in the fits presented by Combi et al. (2010) show some variation, which was interpreted by those authors to indicate spectral variations from one portion of the SNR to

the other. We adopted mean values for these parameters and fit our extracted MOS1, MOS2 and PN spectra with these mean values in a WABS×(PSHOCK+POWER LAW) model: we present the results of the fit using these parameters for Table 6. We note that we obtain a marginally statistically acceptable fit to the MOS1+MOS2+PN spectra using this model with these fit parameters ( $\chi^2_\nu = 1.21$ ). The values for the parameters of the thermal model and the column density derived by Combi et al. (2010) are comparable to those that we obtained. Like Combi et al. (2010), we conclude that the X-ray emitting plasma associated with Kes 17 is in CIE (as indicated by their fitted value for  $\tau$ ), but unlike Combi et al. (2010), we do not require an additional power law component to obtain an acceptable fit to the extracted spectra. When we added the power law, the value of  $\chi^2_\nu$  was not improved (as listed in Table 6). The differences between our results and those published by Combi et al. (2010) may originate from the choice of background subtraction (we have chosen an annular region for the extraction of a background spectrum while Combi et al. (2010) extracted background spectra “from a region where no X-ray emission was detected”). After careful background subtraction, the detection of emission above 5 keV was marginal in the spectra.

Gök & Sezer (2012) presented an analysis of observations made of Kes 17 with the X-ray Imaging Spectrometers (XISs) aboard *Suzaku*. Those authors fitted the extracted spectra using the WABS absorption model coupled with the variable abundance thermal model VMEKAL (Mewe et al. 1985, 1986; Liedahl et al. 1995): the abundances of magnesium, silicon and sulfur were thawed by those authors during the fitting while the abundances of the other elements were frozen to solar values. In addition, Gök & Sezer (2012) used an additional power law component in their spectral fitting like Combi et al. (2010). To compare our results with those presented by Gök & Sezer (2012), we fitted our extracted MOS1+MOS2+PN spectra with the fit parameters published in that paper. We present the results of this fitting in Table 6: we obtain a statistically acceptable fit using these fit parameters ( $\chi^2_\nu = 1.11$ ) and again the values for the parameters  $kT$  and  $N_H$  derived by Gök & Sezer (2012) are similar to those obtained by Combi et al. (2010) and the present work. Gök & Sezer (2012) also concluded that the X-ray emitting plasma associated with Kes 17 is in CIE. We also attempted to include a power law component in the spectral fitting: although the improvement of the fit was not significant, the temperature did become lower (from 0.90 to 0.84 keV). The temperatures that we obtained were comparable to the temperatures published in those two papers. Since the qualities of the fits of the thermal model with or without a power law in the Combi et al. (2010) and Gök & Sezer (2012) were not compared, the essentiality of the power law is not clear in the X-ray energy range. Inspection of our high energy *XMM-Newton* image of Kes 17 (see Panel (c) of Figure 7) does suggest that some high energy X-ray emission is indeed associated with Kes 17 and the origin of this emission is uncertain. Possible origins for this particular emission include high energy

thermal emission from the SNR or synchrotron emission from an as yet undiscovered neutron star associated with Kes 17. Finally, we comment that Combi et al. (2010), Gök & Sezer (2012) and our present work all agree that the contrasting center-filled X-ray morphology and shell-like radio morphology of Kes 17 motivate its classification as a mixed-morphology SNR. We will return to the study of the MOS1+MOS2+PN spectra of Kes 17 when we discuss overionization in mixed-morphology SNRs in Section 5.

### 3.2. G311.5–0.3

G311.5–0.3 was first discovered during surveys made with the Parkes 64-meter radio telescope at 5000 MHz (Shaver & Goss 1970a) and the Molonglo radio telescope at 408 MHz (Shaver & Goss 1970b). It was first classified as a SNR by Shaver & Goss (1970c) based on its nonthermal spectral index ( $\alpha = -0.49$ ). Those authors also measured an angular diameter of 3.9 arcminutes for G311.5–0.3 and extrapolated a flux density at 1 GHz of 3.7 Jy from measured flux densities at 408 MHz and 5000 MHz. Using the flux density at 1 GHz, the measured angular extent and the surface-brightness diameter ( $\Sigma$ -D) relation for SNRs derived by Kesteven (1968b),<sup>11</sup> Shaver & Goss (1970c) calculated a distance of 12.5 kpc to this SNR and a corresponding diameter of 14 pc: we adopt this distance to G311.5–0.3 in this paper. We also note that Caswell et al. (1975) placed a lower limit of 6.6 kpc on the distance to this SNR based on its HI absorption profile. Additional radio observations made of a field including this SNR at the same two frequencies as Shaver & Goss (1970a) and Shaver & Goss (1970b) were described by Caswell & Barnes (1985): the values for the angular extent, flux densities and spectral index measured by those authors for the SNR were in good agreement with the values given by Shaver & Goss (1970c). A shell-like radio morphology for this SNR was first suggested by Retallack (1980): in addition, Whiteoak & Green (1996) described observations made of G311.5–0.3 at the frequency of 843 MHz using the MOST: they also reported a shell-like morphology for the source and measured a flux density of 2.9 Jy at 843 MHz for this SNR. Finally, Cohen & Green (2001) compared MOST observations made at this frequency with observations made at 8.3  $\mu$ m with the Midcourse Space Experiment (MSX, Mill et al. 1994) and reported that emission from G311.5–0.3 at this wavelength was not detected by MSX down to a limiting flux of  $1.0 \times 10^{-6} \text{ W m}^{-2} \text{ sr}^{-1} = 2.35 \times 10^{-13} \text{ ergs cm}^{-2} \text{ sec}^{-1}$ . Frail et al. (1996) included G311.5–0.3 among a set of Galactic SNRs that were observed with the intent of detecting maser emission from the OH satellite line at 1720.5 MHz with the Parkes 64-meter radio telescope, but no such emission was detected from G311.5–0.3. There have been no previously-published analyses of X-ray emission from this

---

<sup>11</sup> $\Sigma \propto D^{-4.5}$  when  $\alpha = -0.5$  which is approximately the same index as the one measured for G311.5–0.3



SNR.

### 3.2.1. *ASCA Observations of G311.5–0.3*

In Figure 9 we present a co-added *ASCA* GIS2+GIS3 image of G311.5–0.3: the SNR was offset by approximately 7 arcminutes from the nominal center of the field of view during the observation. Radio emission (as detected at the frequency of 843 MHz) is plotted as contours overlaying the X-ray emission. The work we describe here represents the first detection and analysis of X-ray emission from G311.5–0.3. The X-ray emission in fact is faint and – coupled with the poor angular resolution of the GIS instruments – prevents us from making very definitive statements about the X-ray morphology. To the limit of the existing data it appears that the emission is centrally-concentrated, in contrast to the shell-like radio morphology of the SNR. As shown below, our spectral analysis strongly indicates that the X-ray emission from G311.5–0.3 is thermal in origin. A centrally-concentrated thermal X-ray morphology coupled with a shell-like radio morphology strongly suggests that G311.5–0.3 is in fact an MM SNR, though additional X-ray observations with improved sensitivity and angular resolution are needed to investigate the true nature of the X-ray morphology of G311.5–0.3 more thoroughly.

GIS2 and GIS3 spectra were extracted for G311.5–0.3 using a circular aperture 5 arcminutes in radius and centered at a position corresponding to the apparent middle of the radio shell of this SNR. The corresponding background GIS2 and GIS3 spectra required for fitting were generated using the FTOOL `mkgisbgd`. The number of detected counts for both spectra were very modest (75 and 111 counts for the GIS2 and GIS3 after background subtraction, respectively), so we only used simple models (namely a power law model and the thermal plasma APEC model) to fit the spectra coupled with the PHABS model to account for photoelectric absorption along the line of sight. A summary of these fits is presented in Table 7: we find that both the power law model and the APEC model adequately fit the extracted spectra, with each fit featuring corresponding values for  $\chi^2_\nu$  of  $\sim 1.1$ . In addition, the values for the column density  $N_H$  returned by the two fits are comparable (ranging from  $N_H \sim 2.7 \times 10^{22} \text{ cm}^{-2}$  to  $N_H \sim 3.3 \times 10^{22} \text{ cm}^{-2}$ ). The value for  $kT$  as returned by the fit with the PHABS×APEC model is elevated but plausible for an SNR (that is,  $kT \sim 0.92^{+1.02}_{-0.22}$  keV) while the value for the photon index  $\Gamma$  returned in the PHABS×POWER LAW fit is steep enough ( $\Gamma = 3.10^{+2.10}_{-1.20}$ ) to also suggest a thermal origin of the X-ray emission rather than (for example) synchrotron radiation. In Figure 10 we present both the *ASCA* GIS2 and GIS3 spectra as fit by the PHABS×APEC model described above (and summarized in Table 7) and a confidence contour plot for this particular fit for the parameters  $kT$  and  $N_H$ .

We conclude that the *ASCA* spectra of G311.5–0.3 favor a thermal origin for the observed X-ray emission from this source: follow-up observations made with higher spectral resolution with sufficient counts are required to confirm this interpretation.

Our analysis of the *ASCA* observations of G311.5–0.3 represents the first detection of X-ray emission from this SNR. As mentioned above, the distance to this SNR is unknown: to help constrain the distance to this SNR more rigorously, we have examined CO data obtained from observations made toward G311.5–0.3. Data from a CO observation of this source (corresponding to a velocity of  $39.7 \text{ km s}^{-1}$ ) is presented in Figure 11: we note the presence of a giant molecular cloud (GMC) detected in proximity to this SNR. Andersen et al. (2011) have argued that G311.5–0.3 is interacting with molecular clouds based on the detection of  $\text{H}_2$  emission at infrared wavelengths. Based on this argument, we claim that G311.5–0.3 is associated with the GMC seen in projection toward G311.5–0.3: the particular velocity of  $39.7 \text{ km s}^{-1}$  for the GMC corresponds to a distance of 12.5 kpc. This distance matches our adopted distance to this SNR. The fitted column density toward this source as determined from our X-ray spectral fitting (that is,  $N_H = 2.7 \times 10^{22} \text{ cm}^{-2}$ ) and our calculated X-ray luminosities have been determined using this adopted distance. We also note that the distance toward G311.5–0.3 as adopted by Andersen et al. (2011) is also based on this high column density as suggested by the velocity of the GMC detected in CO: the uncertainty of the distance estimate is not known. In Figure 12 we present a *Spitzer* three-color IRAC image of G311.5–0.3 with X-ray contours (corresponding to the emission detected by the *ASCA* GIS2+GIS3 detectors) overlaid. The nearly-complete infrared emission with colors consistent with molecular shocks (see Andersen et al. 2011) and the center-filled thermal X-ray emission support the classification of this source as an MM SNR.

### 3.2.2. Discussion of X-ray Properties of G311.5–0.3

Based on its center-filled thermal X-ray morphology and its shell-like radio morphology, we suggest that G311.5–0.3 belongs to the class of MM SNRs. As noted above, the infrared properties of this SNR can be modeled with shocked molecular emission and we find evidence (based on a CO observation) of a cloud seen in projection toward G311.5–0.3: the large distance implied to this SNR based on the high column density (as derived from the spectral fitting) matches the implied distance to this cloud. The infrared colors of G311.5–0.3 imply that the SNR is a molecular SNR (Reach et al. 2006) and IRS follow-up spectroscopy confirmed that the *Spitzer* IRAC  $4.5\mu\text{m}$  band emission shown in Figure 12 is  $\text{H}_2$  emission (Hewitt et al. 2009) which likely originates from the interaction between the SNR and dense clouds. Our *ASCA* analysis of G311.5–0.3 revealed for the first time X-ray emission from

this SNR. The X-ray morphology of the emission is center-filled – lying within the radio and infrared shells of emission – and the X-ray emission is thermal with a temperature  $kT \sim 0.98$  keV. For these reasons, we suggest that G311.5–0.3 is an MM SNR, but because the number of photons in the *ASCA* observation of G311.5–0.3 is limited, future observations of this SNR with improved angular resolution and flux sensitivity are required to confirm this classification. Such observations may also help strengthen the correlation between the phenomenon of MM SNRs and SNRs interacting with adjacent molecular clouds.

### 3.3. G346.6–0.2

Like G311.5–0.3, G346.6–0.2 was first detected as a radio source and classified as an SNR based on surveys made with the Parkes 64-meter radio telescope at 5000 MHz and the Molonglo radio telescope at 408 MHz (Clark 1973; Clark et al. 1975). These observations – along with more recent radio observations made of the SNR by Dubner et al. (1993) using the Very Large Array (VLA) at 1.465 GHz as well as by Whiteoak & Green (1996) using the MOST at 843 MHz – reveal the SNR to be shell-like with a diameter of approximately 8.2 arcminutes. Dubner et al. (1993) measured a flux density of 8.1 Jy at 1.465 GHz and also estimated a spectral index of  $\alpha = -0.5$  for this SNR. Those authors also commented that the shell of radio emission from the SNR appeared to be flattened with a noticeable compression along the eastern and northwestern borders. Based on observations made with the VLA of the OH ground state transition at 1720 MHz, Koralesky et al. (1998) detected five masers along the southern rim of the SNR. Green et al. (1997) also reports the detection of OH maser emission at 1720 MHz from G346.6–0.2 as observed with the Parkes 64-meter telescope. Interestingly, the radio emission from the SNR is strongest from the northern, eastern and western portions of the shell but is noticeably weaker along the southern rim, where the masers are detected. Dubner et al. (1993) estimated the distance to G346.6–0.2 to be  $\sim 9$  kpc based on the  $\Sigma$ - $D$  relationship for SNRs that was presented by Huang & Thaddeus (1985) while Koralesky et al. (1998) provided lower and upper bounds on the distance to this SNR of 5.5 kpc and 11 kpc respectively based on the estimates of the rotational velocities of the molecular clouds argued to be interacting with G346.6–0.2 based on detected maser emission. We adopt a distance of 11 kpc to this SNR for the remainder of this paper: we note that a larger distance estimate to G346.6–0.2 is supported by the enhanced column density seen toward this SNR based on the results of our spectral fitting (see Section 3.3.1). Previously-published X-ray studies of G346.6–0.2 have been presented by Yamauchi et al. (2008) (who analyzed an *ASCA* observation of G346.6–0.2), Sezer et al. (2011b) and Yamauchi et al. (2013) (who both analyzed a *Suzaku* observation of this SNR). we compare our results in the present paper with the results published in those papers in Section 3.3.2.

### 3.3.1. *ASCA Observations of G346.6–0.2*

In Figure 13 we present a co-added *ASCA* GIS2+GIS3 image of G346.6–0.2: the center of the X-ray emission from the SNR was offset by approximately 14 arcminutes from the nominal center of the field of view during the observation. We have overlaid radio contours at a frequency of 843 MHz to illustrate the radio morphology of the shell: similar to the situation with G311.5–0.3 described previously, while G346.6–0.2 is only modestly detected by *ASCA*, the X-ray morphology appears to be center-filled while the radio emission is shell-like. Again, similar to the situation with G311.5–0.3, unfortunately the poor angular resolution of the GIS2 and GIS3 instruments and the modest detection of the SNR prevent us from making more conclusive statements about the general X-ray morphology of G346.6–0.2. As shown below, the X-ray emission detected from this SNR is predominately thermal in origin. The contrasting X-ray and radio morphologies of G346–0.2 coupled with the thermal nature of its X-ray emission motivate the classification of this source as a mixed-morphology SNR (which also parallels our results with G311.5–0.3). As mentioned previously, the detection of maser emission from this SNR strongly suggests that G346.6–0.2 is currently interacting with a molecular cloud: interactions with molecular clouds is another commonly-seen characteristic of MM SNRs.

GIS2 and GIS3 spectra were extracted for G346.6–0.2 using a circular aperture 5 arcminutes in radius and centered at a position corresponding to the apparent middle of the radio shell of this SNR. The region of spectral extraction is indicated in Figure 13: similar to our work in analyzing the GIS2 and GIS3 spectra of G311.5–0.3, we used the FTOOL `mkgisbgd` to generate background spectra needed for spectral fitting. Inspection of the extracted spectra revealed that there was a significantly greater amount of emission at higher energies compared to the extracted spectra of Kes 17 and G311.5–0.3. Note that our re-analysis of *ASCA* data of G346.6–0.2 produces higher quality spectra than those presented by Yamauchi et al. (2008). We first fitted the extracted spectra with a simple power law model: the photon index of the power law fit was  $\Gamma \sim 2.5$  but the fit was not statistically acceptable ( $\chi^2_\nu=1.34$ ). We then fitted the spectra with the plasma model APEC (with the abundance frozen to solar): the temperature of the fit was  $kT \sim 2.5$  keV but once again the fit was not acceptable ( $\chi^2_\nu=1.45$ ). We then fit the spectrum with the APEC model again, this time with the abundance parameter thawed: the fit returned by this model was significantly improved ( $\chi^2_\nu=1.22$ ) but still not statistically acceptable. The upper limit on the fitted elemental abundance was 0.4 (relative to solar) while the fitted temperature was  $kT \sim 3.4$  keV, which is higher than those typically measured for MMSN SNRs. If this estimated temperature for the SNR is indeed true, it may indicate that G346.6–0.2 is a particularly young SNR. We also attempted to fit the spectra with the VAPEC model: we obtained a statistically-acceptable fit with the VAPEC model ( $\chi^2_\nu=1.14$ ) though the only elemental

abundance that was found to exceed solar was neon, and in this case the fitted abundance was very high (with a lower limit of 26 times solar). However, because the low signal-to-noise of the extracted GIS spectra made it too difficult to search for variations in the abundances of specific elements in a rigorous manner, we discarded this PHABS×VAPEC fit. Next, we fit the spectrum with the non-equilibrium ionization plasma model NEI (with the abundance frozen to solar): an acceptable fit was obtained ( $\chi^2_\nu$  of the fit was 1.07) but again the fitted temperature ( $kT = 2.80^{+0.80}_{-0.50}$  keV) was high for an SNR while the ionization timescale ( $\tau = 7.27^{+6.23}_{-3.77} \times 10^9$  cm<sup>-3</sup> s) was lower than other MM SNRs. This result indicated that the X-ray-emitting plasma associated with G346.6–0.2 is not in CIE and motivated the use of an NEI model with thawed abundance coupled with a power law to fit properly model the high energy X-ray emission. Due to the low signal-to-noise in the spectrum that would make calculating the error bounds of many individual parameters difficult, we attempted fits where we froze values of  $\tau$  and  $\Gamma$  to physically realistic parameters (specifically  $10^{11}$  cm<sup>-3</sup> s for  $\tau$  to reflect the X-ray-emitting plasma being outside of CIE and 0.5 and 2.0 for  $\Gamma$  to reflect values obtained in fits of components of hard emission observed toward other Galactic SNRs). We attempted to analyze diagnostics of the NEI model using line ratios such as He $\alpha$  over Ly $\alpha$  for Mg, Si or S, but none of them show clear lines so such analysis was not possible. In considering the fits with high  $\tau$ , all appear to be statistically acceptable with approximately the same values of  $\chi^2_\nu$ : we believe that the fits made using adopted values for  $\Gamma$  and  $\tau$  of 0.5 and  $10^{11}$  cm<sup>-3</sup> s respectively might be the most physically reasonable because these values for these fit parameters may be the most physically accurate.

We present a summary of these fits in Table 8. In Figure 14 we present the *ASCA* GIS2 and GIS3 spectra as fit by the PHABS×(NEI+Power Law) model described above where we have frozen  $\tau$  and  $\Gamma$  to  $8 \times 10^{10}$  cm<sup>-3</sup> s and 0.5, respectively. The results of all of the fitting (including values for fit parameters) are listed in Table 8. Finally, in Figure 15 we present a multi-wavelength image – X-ray, radio and infrared (namely *Spitzer* MIPS) – of G346.6–0.2.

### 3.3.2. Discussion of X-ray Properties of G346.6–0.2

In a previous analysis of extracted GIS spectra of this SNR, Yamauchi et al. (2008) presented statistically-acceptable fits using a thermal component (WABS×MEKAL, with fitted values of  $N_H = 2.0^{+3.5}_{-1.6} \times 10^{22}$  cm<sup>-2</sup> and  $kT = 1.6^{+3.1}_{-1.2}$  keV) or a power law component (WABS×Power Law, with fitted values of  $N_H = 2.6^{+8.2}_{-2.2} \times 10^{22}$  cm<sup>-2</sup> and  $\Gamma = 3.7(>1.7)$ ). we find that we can obtain statistically acceptable fits to our extracted spectra using these models within the quoted error bounds. More recently, Sezer et al. (2011b) described an analysis of an observation made of G346.6–0.2 with *Suzaku*: those authors presented spectral fits to the

diffuse emission using several different thermal models (including VMEKAL, VNEI and the constant temperature plane parallel shock plasma model with variable elemental abundances VPSHOCK – see Mazzotta et al. (1998)) coupled with a power law model (the fitted values of the photon indices were  $\Gamma \sim 0.5-0.6$ ). The thermal models all featured abundances of several elements (namely magnesium, silicon, sulfur, and iron) which were all sub-solar while the abundance of calcium exceeded solar. We have fitted our extracted spectra with the models and the associated fit parameters published by Sezer et al. (2011b) and we present our results in Table 8. We obtain statistically acceptable fits to our extracted spectra using these models with these associated parameters: like Sezer et al. (2011b), we need a combination of a thermal component and a power law component to obtain a statistically acceptable fit with physically realistic parameters. Unfortunately our extracted GIS spectra lack sufficient signal-to-noise for a detailed analysis of the elemental abundances of the X-ray-emitting plasma as conducted by Sezer et al. (2011b). Using *ASCA* data, we confirm that the X-ray emitting plasma associated with G346.6–0.2 is thermal and that the X-ray morphology is center-filled within a radio shell. These facts motivate the classification of G346.6–0.2 as an MMSNR. Yamauchi et al. (2013) present a more detailed analysis of the *Suzaku* observations of G346.6–0.2 and argue that the X-ray spectrum of this SNR is best fit with a recombining plasma model, while such spectral analysis was not possible with the *ASCA* data due to the limited number of counts and the poorer spectral resolution.

Based on the measured elemental abundances in their fits to the extracted spectra, Sezer et al. (2011b) argued that the X-ray emission from G346.6–0.2 is ejecta-dominated and – by analyzing the relative abundances of the elements – that a Type Ia supernova explosion produced this SNR. We note, however, that the H<sub>2</sub> emission detected from this SNR by Hewitt et al. (2009) indicates the presence of a fast J-shock (with a velocity of approximately 150 km s<sup>−1</sup>): the spectral lines associated with shocked H<sub>2</sub> suggest a high preshock density, such as the elevated preshock density associated with molecular clouds. We argue that the presence of this shocked H<sub>2</sub> indicates an interaction between this SNR and the adjacent molecular cloud (as supported by the detection of maser emission from the perimeter of this SNR by Koralesky et al. (1998)). We therefore argue that G346.6–0.2 had a massive stellar progenitor and that the type of supernova that created this SNR was a Type Ib/Ic/II supernova (that is, the supernova types that are all associated with massive stellar progenitors). Such massive stellar progenitors are usually associated with MM SNRs. Future *XMM-Newton* and *Chandra* observations of G346.6–0.2 would be critical in confirming or refuting these conclusions.



### 3.4. CTB 37A (G348.5+0.1)

The CTB 37 radio complex was first cataloged as a radio source by a 960 MHz survey conducted by the Owens Valley Radio Observatory (Wilson & Bolton 1960; Wilson 1963). This complex was resolved into two discrete radio sources – CTB 37A and CTB 37B – by radio observations made at multiple frequencies by Milne & Hill (1969), who measured non-thermal radio spectral indices for both objects ( $\alpha=-0.55$  in each case) and thus classified the two sources as SNRs. Subsequent radio observations of CTB 37A (Milne & Dickel 1975; Downes 1984; Kassim et al. 1991) revealed this SNR to feature a shell-like morphology with bright northern and eastern rims. Milne & Hill (1969) estimated an integrated flux density for CTB 37A at 1410 MHz of approximately 76 Jy. Based on MOST observations of this SNR, Whiteoak & Green (1996) commented on the shell-like morphology of CTB 37A by noting that this source possessed one of the highest mean surface brightnesses of any SNR in the MOST catalog. Whiteoak & Green (1996) also estimated the angular extent of CTB 37A to be  $19 \times 16$  arcminutes and commented on the presence of faint emission associated with this SNR extending into the southwest: such an extension of emission is consistent with the expansion into a cavity. OH masers observed at a frequency of 1720 MHz have been detected along the northern, western and southern boundaries of this SNR as well as toward its center (Frail et al. 1996; Brogan et al. 2000; Hewitt et al. 2008), though a bimodal distribution of measured velocities was observed for these masers (specifically, masers with associated velocities of  $-65 \text{ km s}^{-1}$  were observed toward the center of the SNR as well as the eastern and southern boundaries while masers with associated velocities of  $-24 \text{ km s}^{-1}$  were observed toward the northern boundary). Caswell et al. (1975) estimated a distance of  $10.2 \pm 3.5$  kpc to CTB 37A based on its observed HI absorption profile while Reynoso & Mangum (2000) derived a distance to the SNR of 11.3 kpc based on a putative interaction between this SNR and adjacent molecular clouds, as observed by emission from the carbon monoxide (CO)  $J=1$  to 0 transition at approximately 115 GHz). More recently, Tian & Leahy (2012) bounded the distance to CTB 37A between 6.3 and 9.5 kpc based on the absorption profile along the line of sight toward the SNR. Those authors concluded that CTB 37A lies in front of the far side of the molecular cloud seen toward this SNR. In the present paper, we adopt a distance of 8 kpc toward this SNR, approximately the mean of the lower and upper distance bounds proposed by Tian & Leahy (2012). We also note that Aharonian et al. (2008) detected  $\gamma$ -ray emission from CTB 37A using the Cherenkov telescopes of the High Energy Stereoscopic System (HESS – see Bernlöhner et al. (2003)): specifically, those authors associated the  $\gamma$ -ray source HESS J1713–385 with CTB 37A (in particular with the region of hard emission seen toward the northwestern rim of the SNR). Based on fits to the spectrum of HESS J1713–385, Aharonian et al. (2008) speculated that the observed emission had a hadronic origin (that is, it is produced by the decay of pions that are created by collisions between cosmic-ray

protons and protons in an adjacent molecular cloud). Regarding previous X-ray observations of CTB 37A, published work based on observations made with *ASCA* (Yamauchi et al. 2008), *Chandra*, *XMM* (both presented by Aharonian et al. (2008)) and finally *Suzaku* (Sezer et al. 2011a) have all appeared previously in the literature: we compare our results with the results presented in those papers in Section 3.4.2.

### 3.4.1. *XMM-Newton* and *Chandra* Observations of CTB 37A

In Figure 16 we present an *XMM-Newton* MOS1 image of CTB 37A over the energy range from 0.7 to 10.0 keV: contours depicting the detected radio emission at 843 MHz as detected by MOST are overlaid. The X-ray emission detected by *XMM-Newton* is indeed extended and appears to lie interior to the radio shell: a similar description of the X-ray morphology of CTB 37A was also presented by Aharonian et al. (2008) and Sezer et al. (2011a). In Figure 17 we present a *Spitzer* IRAC 5.8  $\mu\text{m}$  image of CTB 37A with *XMM-Newton* MOS1 X-ray emission overlaid with contours. We have extracted MOS1, MOS2 and PN spectra for the entire diffuse emission (except for a region to the northwest which is known to feature a significantly harder spectrum than the diffuse emission from the rest of the SNR – see the description below). This extraction region was approximately four arcminutes in diameter and was centered on the nominal center of the observed diffuse X-ray emission. For the purposes of spectral fitting, a background spectrum was extracted from an annular region extending approximately 0.5 arcminutes in radius beyond the region of source extraction and with the same center. These regions of extraction are depicted in Figure 16. We also attempted to fit extracted MOS1, MOS2 and PN spectra of the northwest region known to feature hard emission, but our extracted spectra lacked a sufficient signal-to-noise ratio suitable for detailed spectral analysis. We will discuss the properties of this source in more detail when we discuss an analysis of its *Chandra* ACIS-I spectrum below.

The MOS1, MOS2 and PN spectra of the diffuse emission were fitted with the APEC and NEI models: statistically acceptable fits were derived with both models. Because the APEC model returned a statistically acceptable fit and because the ionization timescale returned by the NEI fit was elevated ( $\tau \sim 10^{13} \text{ s cm}^{-3}$  with a lower bound of  $\sim 10^{11} \text{ s cm}^{-3}$ ), we conclude that the X-ray emitting plasma is close to thermal equilibrium. We also allowed the abundances of the APEC and NEI models to vary to see if the quality of the fits could be improved. In fact, small improvements in the quality of the fit (as measured by the  $\chi^2_\nu$  parameter) were realized as sub-solar values for the abundances were derived (approximately 0.3-0.4). We also tried fitting the spectra with the VAPEC and VNEI models: only in the cases where silicon was varied were modest improvements in the value of  $\chi^2_\nu$  attained. In

those cases, the abundance of silicon was sub-solar (approximately 0.5-0.6). In Table 9 we present a summary of the parameters for the different model fits to the MOS1, MOS2 and PN spectra of CTB 37A. In Figure 18 we present a plot of the MOS1, MOS2 and PN spectra of CTB 37A as fit with the PHABS×APEC model with variable abundances. We also present in that figure confidence contour plots that depict  $N_H$  versus  $kT$  as well as  $kT$  versus abundance.

In Figure 19 we present an exposure-corrected *Chandra* ACIS-I image of CTB 37A over the energy range from 0.5 through 10.0 keV: contours depicting the detected radio emission at 843 MHz as detected by MOST are overlaid. Similar to the morphology seen in Figure 16 where the X-ray emission detected by the *XMM-Newton* MOS1 is detected, the X-ray emission from CTB 37A as detected by the *Chandra* ACIS-I appears to lie interior to the well-defined radio shell: the emission is brightest toward the eastern half of the SNR. In Figure 20 we present a three-color exposure-corrected *Chandra* ACIS-I image of CTB 37A with the soft (0.5-1.5 keV), medium (1.5-2.5 keV) and hard (2.5-10.0 keV) emission depicted in red, green and blue, respectively. We have extracted spectra from three particular regions of CTB 37A: we denote these regions as the northwest region, the northeast region and the southeast region, respectively, and in Figure 21 we show these regions of spectral extraction (along with the accompanying regions where background spectra were extracted). To the best of our knowledge, this is the first spatially-resolved spectroscopic study of the X-ray emission from this SNR. Through this analysis (as described below), we have identified spectral variations between the northeastern and southeastern regions of the SNR.

We first discuss our analysis of the northwest region: inspection of Figure 21 clearly indicates that this source emits primarily hard X-rays: we obtained an adequate fit to this spectra using a simple power law with  $\Gamma = 1.18^{+0.42}_{-0.33}$  and  $N_H = 4.08^{+1.32}_{-0.88} \times 10^{22} \text{ cm}^{-2}$ . These fit parameters are consistent with those obtained by Aharonian et al. (2008) who also extracted and fit the spectrum of this source (which they denoted as CXOU J171419.8–383023 – we shall use this designation for the remainder of the paper) with a PHABS×POWER LAW model. Aharonian et al. (2008) also speculated that this hard X-ray source is associated with the  $\gamma$ -ray source HESS J1714–385 and – regarding the true nature of this source – considered such scenarios as the high energy emission originating from an interaction between the SNR and the adjacent molecular cloud complex or from a pulsar wind nebula, with the latter scenario seeming more plausible.

In the cases of the spectra of the northeast and southeast regions, we obtained acceptable fits using the thermal models APEC and NEI. Statistically-acceptable fits were obtained with both models: because acceptable fits were obtained with the APEC model and because the ionization timescales derived by the NEI models were high ( $\tau \sim 10^{11} \text{ s cm}^{-3}$  with lower limits

of  $10^{10} \text{ s cm}^{-3}$  or higher), we conclude that the X-ray emitting plasma in both regions is close to ionization equilibrium. The fitted column densities for both regions are comparable ( $N_H \sim 3 \times 10^{22} \text{ cm}^{-2}$ ). This fitted value is lower than the column density derived toward CXOU J171419.8–383023 but – within the error bounds – the estimated column densities for all three regions are comparable. Interestingly, a difference in temperatures is seen, with the fitted temperatures of the northeast region ( $kT = 0.55\text{--}0.57 \text{ keV}$ ) being noticeably higher than the southeast region ( $kT = 0.78\text{--}0.83 \text{ keV}$ ). Again, compared to the fit to the extended thermal emission from CTB 37A as derived by Aharonian et al. (2008), our derived column densities for both regions are comparable and our derived temperature for the northeast region is quite similar but our temperature for the southeast region is noticeably lower. We also find differences in the fitted values for the abundances of the two regions: while superior fits to the spectra of the northeast region are obtained with both the APEC and NEI models when the value of the abundance is sub-solar ( $\sim 0.4$ ), the derived values of the abundances obtained from the fits to the spectra of the southeast region with both the APEC and NEI models are consistent with a solar abundance. The detection of a reduced value of the abundance is consistent with the result seen previously for the extracted *XMM-Newton* spectra of CTB 37A. In Table 10 we present a summary of the fit parameters for the spectra of these three regions. In Figure 22 we present the extracted *Chandra* ACIS-I spectrum of CXOU J171418.8–383023 as fit with the PHABS×POWER LAW model and a confidence contour plot for this fit for the parameters  $N_H$  and  $\Gamma$ . In Figure 23 we present the extracted *Chandra* ACIS-I spectrum of the northeast region as fit with the PHABS×APEC model with a thawed abundance as well as confidence contour plots for the parameters  $N_H$  and  $kT$  as well as abundance and  $kT$ . Lastly, in Figure 24 we present the extracted *Chandra* ACIS-I spectrum of the southeast region as fitted with the PHABS×APEC model as well as a confidence contour plot for the parameters  $N_H$  and  $kT$ .

We comment on the discrete X-ray source located at RA (J2000.0)  $17^h 14^m 28.6^s$ , Dec (J2000.0)  $-38^\circ 36' 01''$ : it is seen in both the *XMM* MOS1 and the *Chandra* ACIS-I images of Figure 19. In the latter image, the source appears to be blue, indicative of a hard spectrum for this source: it was also detected by Aharonian et al. (2008) and cataloged by those authors as CXOU J171428.5–383601. We will adopt that designation for the source for the remainder of the paper. It is possible that this source may be the neutron star produced by the supernova explosion that created the SNR CTB 37A itself. To investigate this possibility, we extracted an ACIS-I spectrum for this source and fitted it with a power law coupled with the photoelectric absorption model PHABS: we obtained a statistically-acceptable fit ( $\chi_\nu^2 = 0.73$ ) using this model. The photon index of the fit is flat ( $\Gamma < 1.3$ ) – consistent with a spectral index expected for a pulsar (Weisskopf et al. 2007) – and the fitted column density ( $N_H < 4.6 \times 10^{22} \text{ cm}^{-2}$ ) is consistent with the values for  $N_H$  derived from thermal fits to

extracted spectra for portions of the X-ray emitting plasma of CTB 37A. We present in Figure 25 the extracted spectrum for CXOU J171428.5–383601 and the confidence contours for the PHABS×Power Law fit described here: it is possible that this source is the neutron star associated with CTB 37A but additional observations are required to determine its true identity.

For the purposes of completeness, in Figure 26 we present *ASCA* GIS and SIS images of CTB 37A and the adjacent SNR G348.0–0.0 (the latter object is seen as a radio filament in these images and is discussed in more detail in Section 3.5). The image shows some hints of emission from both of these SNRs, but because the signal-to-noise ratios of these images are poor, we have instead concentrated on the more sensitive *XMM-Newton* and *Chandra* observations of these SNRs.

### 3.4.2. Discussion of Physical Properties of CTB 37A

Previous X-ray spectral analyses of CTB 37A have been published in the literature based on data from *ASCA* GIS observations (Yamauchi et al. 2008), *Chandra* and *XMM* (Aharonian et al. 2008) and finally *Suzaku* (Sezer et al. 2011a). In the case of the *ASCA* observations, Yamauchi et al. (2008) fit the extracted combined GIS spectrum (where the authors had merged the GIS2 and GIS3 spectra to boost the signal-to-noise) with a WABS×MEKAL model with elemental abundances frozen to solar, a WABS×MEKAL model with silicon abundance thawed and other elemental abundances thawed and a WABS×Power Law model. Because the signal-to-noise of the fitted spectrum was poor, the fit parameters were poorly constrained: fitted values for  $N_H$ ,  $kT$  and  $\Gamma$  ranged from  $1.7 \times 10^{22}$  to  $2.4 \times 10^{22}$ , 2.2 keV to 2.8 keV and 2.4 to 3.6, respectively. We attribute the differences between these fit results and the fit results presented in this paper to the poor signal-to-noise of the merged GIS spectrum and significant contaminating flux from bright sources located outside the field of view. Aharonian et al. (2008) presented spectral fits to the extracted *Chandra* and *XMM-Newton* spectra of the entire diffuse emission associated with CTB 37A. Those authors derived a column density  $N_H = 3.15^{+0.13}_{-0.12} \times 10^{22} \text{ cm}^{-2}$  and a temperature  $kT = 0.81 \pm 0.04 \text{ keV}$ . We find that while our derived value for  $N_H$  ( $\sim 3 \times 10^{22} \text{ cm}^{-2}$ ) is comparable to the value derived by Aharonian et al. (2008), our derived values for the temperature ( $kT \sim 0.5\text{--}0.7 \text{ keV}$ ) are slightly lower. We argue that our fit values are broadly consistent with the results published by Aharonian et al. (2008): we also note that Yamauchi et al. (2008) applied the fit parameters derived by Aharonian et al. (2008) to their extracted merged GIS spectrum and were able to obtain a statistically-acceptable fit.

Sezer et al. (2011a) presented a spectral analysis of the whole X-ray emission detected from CTB 37A using data obtained from a pointed observation made of the SNR by *Suzaku*. Those authors fit the extracted XIS spectra using a WABS $\times$ (VMEKAL+Power Law) model: their derived fit parameters were  $N_H \sim 3 \times 10^{22} \text{ cm}^{-2}$ ,  $kT \sim 0.6 \text{ keV}$  and  $\Gamma = 1.6$ : they obtained a statistically-acceptable fit with all elemental abundances frozen to solar values. We have fit our extracted *XMM-Newton* spectra with this model and present the results of this fit in Table 9: we obtain a statistically-acceptable fit (with a reduced  $\chi^2$  value of 1.13) using the parameters derived by Sezer et al. (2011a). Regarding the additional power law component present in the Sezer et al. (2011a) fit: we do not require such a component to adequately fit the MOS1+MOS2+PN spectrum of CTB 37A. We attribute the differences between the spectral fit that we derived and the spectral fit derived by Sezer et al. (2011a) to different selections of regions to extract background spectra. Sezer et al. (2011a) chose a background region which had the lowest X-ray flux available (see Figure 1 in their paper), not from a region accurately reflecting the Galactic X-ray background behind the SNR. We argue that our choice of region for extraction of a background spectrum is more appropriate.

### 3.5. G348.5-0.0

G348.5–0.0 was first identified as a “jet”-like feature extending from the eastern edge of the bright radio rim of CTB 37A in early radio observations made by Milne et al. (1979). While those authors favored the scenario where the jet was a radio feature generated by CTB 37A, subsequent work by Downes (1984) instead argued that the jet was a separate SNR seen in projection toward CTB 37A. The classification of G348.5–0.0 as a distinct SNR was confirmed by Kassim et al. (1991) based on radio observations made at the frequencies of 333 MHz, 1443 MHz and 4835 MHz. The high angular resolution radio maps provided by those authors of G348.5–0.0 reveal that the morphology of the SNR may be described as a concave rim pointed downward with an angular extent of approximately 3.5 arcminutes. A similar morphology for the SNR is described by Whiteoak & Green (1996) based on their observations made with the MOST of this SNR at a frequency of 843 MHz. Kassim et al. (1991) estimated the flux density and the spectral index of the SNR to be 6.2 Jy at 1443 MHz and  $-0.4 \pm 0.1$ , respectively: however, those authors stressed that their estimated flux density at 1443 MHz (and at the other frequencies as well) must be interpreted as a lower limit because observations of this source at frequencies greater than 1000 MHz (including their own observation at 4835 MHz) resolve out much of the flux density of the source. For the same reason, the calculated spectral index should be treated as a lower limit as well (that is,  $\alpha > -0.4 \pm 0.1$ ). Hewitt et al. (2008) described observations made with the Green Bank Telescope (GBT) of a sample of Galactic SNRs (including G348.5–0.0) at the frequencies



corresponding to all four ground-state transitions of the OH radical (namely the frequencies of 1612.231, 1665.4018, 1667.359 and 1720.530 MHz). Those authors identified two masers that were spatially coincident with the SNR. Reynoso & Mangum (2000) favored a distance of 13.5 kpc to this SNR based on a putative association between a weak CO concentration observed toward the west of the radio rim. However, Tian & Leahy (2012) instead argued for an upper limit on the distance to G348.5–0.0 of 6.3 kpc based on the HI absorption profile observed along the line of sight toward this SNR. We therefore adopt a distance of 6.3 kpc to G348.5–0.0 for the remainder of this paper.

A clear detection of X-ray emission from G348.5–0.0 (in particular, from the luminous southern radio rim) has proven to be challenging with the datasets which are currently available for this SNR. In Figure 26 we present *ASCA* GIS and SIS images of G348.5–0.0: emission from this SNR is not clearly seen in either of these images. As noted previously, Yamauchi et al. (2008) stated that the *ASCA* datasets are badly confused by contaminating stray flux originating from a bright source located just south of the field of view. For this reason, we were not able to detect clearly X-ray emission from the radio rim using the *ASCA* GIS data. While the pointed *Chandra* observation of CTB 37A which was conducted with the ACIS-I array also included the radio rim of G348.5–0.0, unfortunately much of this rim fell into a gap between chips in the ACIS-I array (see Figures 20 and 21). This situation – coupled with the short exposure time of the observation – prevented the clear detection of X-ray emission from the radio-luminous limb of this SNR as well.

The pointed *XMM-Newton* observation made of CTB 37A also sampled G348.5–0.0 and we were able to extract MOS1+MOS2+PN spectra for the luminous radio rim (though the short exposure time of the observation and the contaminating stray flux severely limited the quality of the data). An elliptical region with radii of 3.52 arcminutes  $\times$  2.19 arcminutes was used to extract X-ray spectra while a region with the same linear dimensions and position angle located approximately 5 arcminutes to the south was used to extract a background spectrum. The locations of these extraction regions are shown in Figure 16: we also note that in Figure 17 we depict X-ray emission as detected by MOS1 overlaid in contours on a *Spitzer* IRAC 5.8 $\mu$ m of a field containing both CTB 37A and G348.5–0.0 (infrared emission from the latter SNR is visible as the concave-downward arc visible at the eastern edge of the image). After background subtraction, we estimate the total number of counts in the extracted MOS1, MOS2 and PN spectra of G348.5–0.0 over the energy range of 0.5 to 10.0 keV to be 68, 26 and 31, respectively. These numbers of counts are unfortunately not sufficient for a sophisticated spectral analysis. We placed an upper limit on X-ray flux and luminosity of G348.5–0.0 over this energy range using the following method. We used the

standard program COLDEN<sup>12</sup> to determine that the nominal Galactic column density  $N_H$  seen toward this SNR is  $\sim 1.7 \times 10^{22} \text{ cm}^{-2}$ . Adopting half of this value as the column seen toward G348.5–0.0 (because the value returned by COLDEN corresponds to the value seen all the way through the Galactic disk) and assuming a Raymond-Smith thermal plasma model (Raymond & Smith 1977) with solar abundances and a temperature of  $kT \sim 0.5 \text{ keV}$ , we used the Portable, Interactive Multi-Mission Simulator (PIMMS<sup>13</sup>) Version 4.2 to estimate a corresponding unabsorbed flux of  $\sim 6.9 \times 10^{-13} \text{ ergs cm}^{-2} \text{ sec}^{-1}$  for G348.5–0.0. Assuming a distance to G348.5–0.0 of 6.3 kpc, we estimate an upper limit for the unabsorbed X-ray luminosity of the luminous radio rim to be  $L_X \sim 3 \times 10^{33} \text{ ergs sec}^{-1}$  (over the energy range of 0.5–10.0 keV). The true X-ray luminosity of G348.5–0.0 may be far below this value. Unfortunately, we still have not clearly detected X-ray emission from this SNR: new X-ray observations conducted with greater sensitivity may be more fruitful in detecting such emission.

#### 4. Plasma Conditions of the SNRs

We now discuss the properties of each SNR in turn. We derive and comment upon such physical properties of the SNRs as age ( $t$ ), hydrogen nuclei density  $n_H$ , electron density  $n_e$  (we will assume that  $n_e = 1.2 n_H$ ), pressure  $P$  and swept-up X-ray-emitting mass  $M_X$  for each SNR. We pattern the discussion in the present paper with the discussion we presented in a previous work (Pannuti et al. 2010) where we derived and commented upon these properties for two other Galactic MM SNRs, HB 21 (G89.0+4.7) and CTB 1 (G116.9+0.2). We use the following equations for our analysis. Values for  $n_e$  and  $n_H$  may be calculated from the value obtained for the normalization of thermal components in fits to the extracted X-ray spectra of the SNRs based on the equation

$$\text{Normalization (cm}^{-5}\text{)} = \frac{10^{-14}}{4\pi d^2} \int n_e n_H dV, \quad (1)$$

where  $d$  is the distance to the SNR in cm and  $V = \int dV$  is the total volume of the SNR (we will adopt uniform densities for  $n_e$  and  $n_H$  – expressed here in  $\text{cm}^{-3}$  – and spherical volumes for the SNRs). We estimated the remnant age  $t_{rad}$  assuming the SNRs are in the snowplow stage of evolution (see Rho & Borkowski 2002) using the following relation

$$t_{rad}(10^4 \text{ yr}) = 0.3 R/V_s = 30 R_s(\text{pc})/V_s(\text{km/s}), \quad (2)$$

---

<sup>12</sup>COLDEN is a standard tool in the CIAO software package that may be accessed on-line at <http://cxc.harvard.edu/toolkit/colden.jsp>.

<sup>13</sup>PIMMS may be accessed on-line at <http://cxc.harvard.edu/toolkit/pimms.jsp>

where  $V_s$  is the shock velocity of the SNR. Values of  $V_s$  were measured from ionic lines detected in the infrared spectra by Hewitt et al. (2009) and Andersen et al. (2011) of the five SNRs considered in this paper (all of these SNRs are in the radiative phase of evolution). We also consider the ratio  $P/k$  (where  $k$  is Boltzmann’s constant) and calculate this ratio using the equation

$$P/k \text{ (K cm}^{-3}\text{)} = 2 n_e T \quad (3)$$

Lastly  $M_X$  is calculated from the equation

$$M_X = f m_H n_H V \quad (4)$$

where  $f$  is the volume filling factor of the X-ray emitting plasma (assumed to be unity in this paper) and  $m_H$  is the mass of a hydrogen nucleus. We discuss these calculated properties for each SNR below: in Table 11 we present our calculated values for each property in the cases of the SNRs Kes 17, G346.6–0.2 and CTB 37A. For comparison, we include other published values for these same properties of these SNRs (we compare our results with these other publications in the text below). In Table 12 we present a summary of the properties of the diffuse emission of the SNRs considered in this paper (including the values of  $V_s$  used in our calculations). We will discuss Table 12 in more detail in Section 6.

*Kes 17:* Based on the derived parameters from our X-ray spectral fits (namely the PHABS×APEC fits to the extracted MOS1+MOS2+PN spectra of Kes 17), we have applied Equations 1, 2, 3 and 4 to calculate an electron density of the X-ray-emitting plasma to be  $n_e = 0.42 \text{ cm}^{-3}$ , a hydrogen density  $n_H = 0.35 \text{ cm}^{-3}$ , an age  $t_{rad}=2.3\times10^4$ , a pressure  $P/k = 5.6\times10^6 \text{ K cm}^{-3}$  and a swept-up mass  $M_X$  of  $52 M_\odot$ .

*G311.5–0.3:* Through inspection of our spectral fit values and using the equations above, we calculate the following values for the properties of G311.5–0.3:  $n_e=0.20 \text{ cm}^{-3}$ ,  $n_H=0.17 \text{ cm}^{-3}$ ,  $t_{rad}=2.5\text{--}4.2\times10^4 \text{ yr}$ ,  $P/k = 4.4\times10^6 \text{ K}$  and  $M_X = 13 M_\odot$ .

*G346.6–0.2:* Using the values of the fit parameters that we derived for the GIS spectra of G346.6–0.0 using the PHABS×(NEI + Power Law) model (specifically where we froze the values of  $\tau = 10^{11} \text{ cm}^{-3} \text{ s}$  and  $\Gamma=0.5$ ), we calculate  $n_e = 0.24 \text{ cm}^{-3}$ ,  $n_H = 0.20 \text{ cm}^{-3}$ ,  $t_{rad} = 4.7\times10^4 \text{ yr}$ ,  $P/k = 1.7\times10^7 \text{ K cm}^{-3}$  and  $M_X = 84 M_\odot$ . We note that this is the only SNR considered in this paper which features X-ray spectra that indicate that the SNR is far from ionization equilibrium.

*CTB 37A:* Based on the fit parameters derived through analysis of the extracted MOS1+MOS2+PN

spectra for the whole SNR, we estimate the following properties for CTB 37A:  $n_e = 0.77 \text{ cm}^{-3}$ ,  $n_H = 0.64 \text{ cm}^{-3}$ ,  $t_{rad} = 3.2\text{--}4.2 \times 10^4 \text{ yr}$ ,  $P/k = 8.2 \times 10^6 \text{ K cm}^{-3}$  and  $M_X = 76 M_\odot$ . All of these parameters are calculated based on spectral analysis of the X-ray bright portion of the northern half of the SNR. We emphasize that the angular extent of this SNR as defined by the extended radio emission includes a southwestern portion (a possible “blow-out” region): no X-ray emission has been detected from this southwestern portion. This region may in fact feature X-ray emission which has remained undetected up to this point by pointed X-ray observations of the SNR. We therefore view our estimate of the X-ray emitting mass associated with this SNR as a lower limit.

## 5. Are the X-ray Emitting Plasmas of These SNRs Overionized?

The phenomenon of overionization has been observed in the X-ray-emitting plasmas associated with numerous Galactic MM SNRs (as well as other Galactic SNRs). Overionization occurs when the electron temperature ( $T_e$ ) is lower than the ionization temperature ( $T_i$ ) of the plasma: in such cases, the recombination process is dominant. Examples of MM SNRs that feature overionized X-ray-emitting plasmas are IC 443 (based on observations made by *ASCA*, *XMM-Newton* and *Suzaku* – see Kawasaki et al. (2002), Troja et al. (2008) and Yamaguchi et al (2009)), W28, W44, W49B and G359.1–0.5 (all based on observations made by *Suzaku* – see Sawada & Koyama (2012), Uchida et al (2012), Ozawa et al (2009), Ohnishi et al. (2011), respectively). Reviews of the phenomenon of overionized X-ray-emitting plasmas associated with SNRs is provided by Vink (2012).

Observationally, overionization of the X-ray-emitting plasma associated with an SNR is manifested by significant residuals that appear when spectra of the plasmas are fitted with CIE and NEI models. For example, in the case of W44, Uchida et al (2012) found significant residuals at  $\sim 1.5 \text{ keV}$  and  $\sim 2 \text{ keV}$ , which are attributed to the Mg-Ly $\alpha$  line and the Si-Ly $\alpha$  line, respectively. In the cases of W44 (Uchida et al 2012), IC 443 (Yamaguchi et al 2009) and G359.1-0.5 (Ohnishi et al. 2011), residuals that emerged after fitting with CIE models are seen at 2.7 and 3.5 keV: lines at these energies are associated with H-like Si (2.67 keV) and H-like S (3.48 keV), respectively. Finally, in the case of W49B, Ozawa et al (2009) identified residuals at the energies of 5.6, 6.2, 6.7, 6.9, 7.9, 8.5 keV: these lines are attributed to Cr K $\alpha$ , Mn $\alpha$  and four Fe lines (of He $\alpha_{rec}$ , Ly $\alpha$ , He $\beta_{rec}$  and He $\gamma$ ), respectively.

We have examined the X-ray spectra of the SNRs in our sample to search for evidence of overionized plasmas associated with these sources. Unfortunately, in the case of CTB 37A, the extracted *Chandra* spectra do not have sufficiently high signal-to-noise to reveal significant residuals (if present): therefore, there is no clear evidence that the X-ray emitting

plasma associated with this SNR is overionized. Recently, Yamauchi et al. (2013) analyzed *Suzaku* spectra of G346.6–0.2 and argued that the plasma associated with this SNR is overionized. Unfortunately the signal-to-noise of our *ASCA* spectra of G346.6–0.2 is insufficient for a study of the overionization of this SNR. Inspection of the *ASCA* spectra reveals a hint of residual dips at 1.5 keV (note the residuals between 1.5–2.5 keV as shown in Figure 14). The residual at 1.5 keV (which is consistent with the Mg Ly $\alpha$  line) could be evidence of over-ionization as seen in W44 (Uchida et al 2012) but the scatter is too large to quantify the overionization. Lastly, the signal-to-noise of our *ASCA* spectra of G311.5–0.3 is too poor to identify any lines, while G348.5–0.0 was not clearly detected by any of the X-ray observations considered here.

Examination of the MOS1+MOS2+PN spectra of Kes 17 (as shown in Figure 6) reveals evidence for residuals at 1.5 keV (a positive dip) and 1.9 keV (a negative dip). Based on the presence of these residuals, we have investigated whether or not the X-ray-emitting plasma associated with Kes 17 is indeed overionized. We conducted a spectral analysis patterned after the analysis presented by Yamauchi et al. (2013) where those authors determined that the X-ray-emitting plasma associated with G346.6–0.2 is overionized. Using the SPEX software package (Kaastra et al. 1996), those authors fitted the extracted *Suzaku* XIS spectra of the SNR using the `neij` model. As described by Yamauchi et al. (2013), this model describes an X-ray emitting plasma where initially the ion temperature  $kT_Z$  and the original electron temperature  $kT_{e1}$  were the same (that is,  $kT_Z = kT_{e1}$ ) and the plasma itself was in collisional ionization equilibrium. Over time, the electron temperature drops to  $kT_{e2}$  due to rapid electron cooling. Such a model can reflect accurately a rapid electron cooling as predicted in models of SNR evolution. In addition, the `neij` model was multiplied by the `absm` model to account for interstellar absorption (also consistent with the work of Yamauchi et al. (2013)).

We first used the SPEX (Version 2.03.03) tool `trafo` (Version 1.02) to convert the extracted *XMM-Newton* spectral files for the whole SNR into `.spo` files suitable for analysis by the software package. We were unable to generate a statistically-acceptable fit with the `neij` model that is superior (in other words, with an improved value for  $\chi^2_\nu$ ) to the fits obtained with the thermal models described above. The residuals of the fits obtained with the `neij` model originate from inconsistencies between the different datasets and because of these limitations the overionization model cannot improve the fit. Thus, the poor signal-to-noise of the datasets prevent us from testing sufficiently whether or not the X-ray-emitting plasma is overionized. A deeper X-ray observation is required to investigate more rigorously the possibility that Kes 17 belongs to the class of overionized MM SNRs.

## 6. Comparison of Properties of the Sampled SNRs: Implications for SNR evolution

In Table 12 we present a summary of the properties of the diffuse emission associated with the four SNRs examined in this paper that were detected in the X-ray. We find that the X-ray properties of three of these SNRs – Kes 17, G311.5–0.3 and CTB 37A – are similar to those of such archetypal MM SNRs as 3C 391 and W44 (Rho et al. 1994; Rho & Petre 1996; Shelton et al. 2004). Specifically, the X-ray temperatures of these three SNRs range from  $kT \sim 0.7$  keV to  $kT \sim 1$  keV, the abundances of the diffuse emission associated with each SNR are approximately solar and all of the SNRs are middle-aged (that is, the ages of all of the SNRs are  $t_{rad} \sim 10^4$  yr old). Lastly, all three of these SNRs are known to produce infrared emission that originates from shocked molecular hydrogen (that is, warm  $H_2$ ): this indicates that these SNRs are interacting with dense ( $10^4 - 10^5 \text{ cm}^{-3}$ ) molecular clouds (Hewitt et al. 2009; Andersen et al. 2011). Therefore, we conclude these three particular SNRs in our sample are similar to the archetypal MM SNRs listed above and others (see Rho & Petre 1996). The X-ray properties of G346.6–0.2 differ somewhat from both those of these three MM SNRs as well as those of the archetypal MM SNRs.

While G346.6–0.2 does feature a center-filled thermal X-ray morphology with a contrasting well-defined shell-like radio morphology that typifies MM SNRs, the X-ray spectrum of this SNR is harder with a higher temperature and the presence of a second harder spectral component is implied. The morphology shows center-filled X-ray emission within a well-defined radio shell like those in other MM SNRs. However, the X-ray spectrum is harder than these other MM SNRs (with a higher temperature,  $kT \sim 2.5\text{--}3.4$  keV) and the fitted ionization timescale is rather lower. We do note however that an age estimate based on the observed infrared line emission from this SNR – recall that the shock velocity used in our analysis is based on detected ionic infrared emission – is similar to the ages estimated for Kes 17, G311.5–0.3, CTB 37A and the archetypal MM SNRs mentioned above. We do not have a clear idea why G346.6–0.2 shows harder X-ray emission, but perhaps it is somehow related to a particular property of this SNR: the detected  $H_2$  emission from G346.6–0.2 differs from the  $H_2$  emission detected from the other MM SNRs in that the detected emission from G346.6–0.2 requires a high velocity J-shock component or a high-velocity C-shock component coupled with a slow-velocity C-shock component to be fit properly. In contrast, the emission detected from the other SNRs requires two slow C-shock components. It is possible that the X-ray emission from G346.6–0.2 is associated with the forward shock of this SNR, which is necessarily a J-shock because C-shocks do not shock-heat the plasmas of SNRs. In addition, or perhaps as an alternate explanation, C-shocks are associated with lower shock velocities: this might indicate that G346.6–0.2 is dynamically a younger SNR. Therefore, this would be an indirect connection between the shock and the X-ray emission



seen from the interior of this SNR. More X-ray observations of this intriguing SNR are clearly warranted.

Observations made with the *Fermi* telescope have detected many MM SNRs at  $\gamma$ -ray energies, including W28, W44, W49B, W51C and IC 443 (Abdo et al. 2009, 2010a,b,c,d; Uchiyama et al. 2010), among others (also see Brandt et al. 2012; Hewitt et al. 2012). The  $\gamma$ -ray emission detected from these sources may be explained as hadronic particle acceleration by the MM SNRs expanding into a dense environment. Of the five SNRs considered in this paper, two – Kes 17 and CTB 37A – have been detected at  $\gamma$ -ray energies: Kes 17 was detected by *Fermi* (Wu et al. 2011), while CTB 37A was detected with very high energy (VHE)  $\gamma$ -ray telescopes (Aharonian et al. 2008) and *Fermi* (Castro & Slane 2010). Our present research has helped to confirm that Kes 17 and CTB 37A are MM SNRs that feature center-filled X-ray emission. We argue that additional  $\gamma$ -ray observations of MM SNRs are needed to investigate the inter-relationship between X-ray and  $\gamma$ -ray emission from these particular sources and mechanisms of particle acceleration.

We note that infrared observations of the five SNRs considered in this paper have revealed that the infrared emission detected from these SNRs is radiative and produced by shocks with velocities  $V_s \sim 70$  to  $150 \text{ km s}^{-1}$ . It appears that each of these SNRs is currently in the snowplow stage of evolution and the X-ray emission detected from Kes 17, G311.5–0.3, G346.6–0.2 and CTB 37A is fossil radiation that was produced during an earlier evolutionary stage of the SNRs. The X-ray emission from several MM SNRs – as observed by *Suzaku* – often exhibits multiple ionization states which come from elemental differences in ionization and recombination timescales (e.g. Sawada & Koyama 2012). The rarefaction of the recombining plasma is likely due to continuous fast cooling of the plasma due to radiative shocks encountering dense clouds (as inferred by the characteristics of the detected infrared emission from these SNRs). Our sample of four X-ray-detected MM SNRs in this paper help confirm that a strong correlation exists between infrared shocked  $\text{H}_2$  emitting SNRs and MM SNRs.

We also note that *Chandra* observations of other MM SNRs – such as W44 and 3C 391 – have confirmed the presence of uniform temperature profiles in X-ray emission from these sources (Chen et al. 2004; Shelton et al. 2004). In addition, wide ranges of plasma conditions and metal enrichment have also been revealed by *ASCA* and *Chandra* X-ray observations of MM SNRs, such as an over-ionized plasma in IC 443 (Kawasaki et al. 2002), a suggested abundance gradient at the bright projected center of W44 (Shelton et al. 2004) and iron-rich ejecta in the MM SNRs 3C 397 and Sgr A East (Safi-Harb et al. 2005; Maeda et al. 2002). Finally, evidence for X-ray emission from an ejecta-dominated plasma associated with IC 443 as detected by *XMM-Newton* was presented by (Troja et al. 2008). Simulations have

shown that the center-filled thermal X-ray emission as observed in MM SNRs can be produced through anisotropic thermal conduction. Specifically, SNRs expanding into denser environments tend to be smaller, making it easier for thermal conduction to dictate large changes in the temperatures of their expanding hot gas bubbles. Therefore, thermal conduction plays a prominent role in determining the observed X-ray morphology of MM SNRs (Tilley et al. 2006). Magnetohydrodynamic (MHD) modeling of SNRs expanding through an inhomogeneous ISM also confirms that X-ray emission detected from MM SNRs can be reproduced when both thermal conduction and the reverse shock of the SNR are included in the modeling (Orlando et al. 2009). After the reverse shock has reached the center of the SNR, a maximum in the X-ray emission is seen toward the center of the SNR and the morphology is centrally brightened: such a morphology is a defining characteristic of MM SNRs. Therefore, it is evident that thermal conduction plays a crucial role in producing SNRs of this class.

Follow-up X-ray observations of the MM SNRs in our sample are vital to investigate further their properties. While these SNRs have already been observed with such current X-ray observatories as *XMM-Newton*, *Chandra* and *Suzaku*, we argue that a deeper observing campaign of these SNRs (as well as other known MM SNRs) is crucial and will permit detailed comparisons between these SNRs to be made. Analysis of the X-ray spectra obtained from these observations will allow us to investigate the line emission of elements present in the X-ray emitting plasma of these sources, specifically their ionization states and temperatures. Such analysis may also reveal the presence of enhanced elemental abundances in the ejecta emission: this phenomenon has been seen in other MM SNRs. Finally,  $\gamma$ -ray observations of the MM SNRs in our sample which have not yet been detected at such high energies – such as G311.5–0.3 and G346.6–0.2 – as well as other MM SNRs are clearly warranted. The detection of  $\gamma$ -ray emission from such sources will provide exciting opportunities to advance our understanding of particle acceleration by these sources.

## 7. Conclusions

The conclusions of this paper may be summarized as follows:

- 1) Using archival X-ray observations made with *ASCA*, *XMM-Newton* and *Chandra*, we have conducted a spectroscopic analysis of the X-ray properties of five SNRs (Kes 17, G311.5–0.3, G346.6–0.2, CTB 37A and G348.5–0.0) detected in the infrared by the *Spitzer* GLIMPSE survey. Four of the five SNRs (namely Kes 17, G311.5–0.3, G346.6–0.2 and CTB 37A) are clearly detected by these observations and we have placed an upper limit on the X-ray luminosity of G348.5–0.0). Our work represents the first published detection of

X-ray emission from G311.5–0.3.

2) The four X-ray detected SNRs all feature a center-filled X-ray morphology with a contrasting shell-like radio morphology: therefore, these sources may be classified as MM SNRs. The X-ray emission from each SNR appears to be thermal in origin: however, when the spectral properties of the X-ray-emitting plasmas of the SNRs are compared, significant variations are seen from one SNR to the other. For example, the plasma associated with Kes 17 may be overabundant in magnesium, suggesting that the plasma may be ejecta-dominated. In addition, evidence exists for the presence of hard components in the X-ray emission from G346.6–0.2. We also note that we have identified a hard discrete X-ray source seen in projection toward CTB 37A (and distinct from the extended emission with a hard spectrum seen toward the northwest rim of the SNR) and suggest that it may be a neutron star associated with this SNR.

3) We have discussed the plasma conditions of the four X-ray detected SNRs and estimated such properties of the plasma as  $n_e$ ,  $t_{rad}$  and  $M_X$ : these values range from  $\sim 0.4\text{--}0.8\text{ cm}^{-3}$ ,  $\sim 2.3\text{--}4.2 \times 10^4\text{ yr}$  and  $\sim 13\text{--}88\text{ }M_\odot$ , respectively. These values are similar to those observed for other MM SNRs.

4) We discuss the implications of our results for studies of SNR evolution. Because all four of the X-ray detected SNRs feature lines produced by shocked  $H_2$  in their infrared spectra, we argue that each of them is interacting with a nearby molecular cloud. We believe that our results help strengthen the link between MM SNRs and interactions between SNRs and molecular clouds: this may help to explain the origin of the center-filled thermal X-ray morphologies of these sources.

We thank the anonymous referee for many useful comments that helped to improve greatly the quality of this paper. T.G.P. also thanks Koji Mukai for assistance with analyzing the *ASCA* datasets considered in this paper and Nicholas Lee for assistance with analyzing the *Chandra* observation of CTB 37A. Finally, T.G.P. also thanks Jelle de Plaa for assistance with using the SPEX software package. This research has made use NASA’s Astrophysics Data System as well as data obtained from the High Energy Astrophysics Science Archive Research Center (HEASARC), provided by NASA’s Goddard Space Flight Center.

## REFERENCES

- Abdo, A. A., Ackermann, M., Ajello, M., Baldini, L., Ballet, J., Barbiellini, G., Baring, M. G., Bastieri, D. et al. 2009, ApJ, 706, L1
- Abdo, A. A., Ackermann, M., Ajello, M., Baldini, L., Ballet, J., Barbiellini, G., Bastieri, D., Baughmann, B. et al. 2010a, ApJ, 712, 459
- Abdo, A. A., Ackermann, M., Ajello, M., Allafort, A., Baldini, L., Ballet, J., Barbiellini, G., Bastieri, D. et al. 2010b, ApJ, 718, 348
- Abdo, A. A., Ackermann, M., Ajello, M., Baldini, L., Ballet, J., Barbiellini, G., Baring, M. G., Bastieri, D. et al. 2010c, Science, 327, 1103
- Abdo, A. A., Ackermann, M., Ajello, M., Baldini, L., Ballet, J., Barbiellini, G., Bastieri, D., Behtol, K. et al. 2010d, ApJ, 722, 1303
- Aharonian, F., Akhperjanian, A. G., Barres de Almeida, U., Bazer-Bachi, A. R., Behera, B., Beilicke, M., Benbow, W., Bernlöhr, K. et al. 2008, A&A, 490, 685
- Andersen, M., Rho, J., Reach, W. T., Hewitt, J. W. & Bernard, J. P., 2011, ApJ, 742, 7
- Arnaud, K. A. 1996, Astronomical Data Analysis Software and Systems V, eds. Jacoby, G. and Barnes, J., p. 17, ASP Conference Series Vol. 101
- Atwood, W. B. et al. 2009, ApJ, 697, 1071
- Benjamin, R. A., Churchwell, E., Babler, B. L., Bania, R. M., Clemens, D. P., Cohen, M., Dickey, J. M., Indebetouw, R. et al. 2003, PASP, 115, 953
- Bernlöhr, K. et al. 2003, APh, 20, 111
- Borkowski, K. J., Lyerly, W. J. & Reynolds, S. P. 2001, ApJ, 548, 820
- Brandt, T. & *Fermi* LAT Collaboration, 2012, American Astronomical Society Meeting Abstracts, 219, #213.03
- Brogan, C. L., Frail, D. A., Goss, W. M. & Troland, T. H. 2000, ApJ, 537, 875
- Burke, B. E., Mountain, R. W., Harrison, D. C., Bautz, M. W., Doty, J. P., Ricker, G. R. & Daniels, P. J. 1991, IEEE Trans., Electron Devices, 38, 1069
- Castro, D. & Slane, P., 2010 ApJ, 717, 372
- Caswell, J. L., Murray, J. D., Roger, R. S., Cole, D. J. & Cooke, D. J. 1975, A&A, 45, 239

- Caswell, J. L. & Barnes, P. J. 1985, MNRAS, 216, 753
- Chen, Y. et al. 2004, ApJ, 616, 885
- Clark, D. H., Caswell, J. L. & Green, A. J. 1973, Nature, 246, 28
- Clark, D. H., Caswell, J. L. & Green, A. J. 1975, AuJPA, 37, 1
- Clegg, P. E. et al. 1996, A&A, 315, L38
- Cohen, M. & Green, A. J. 2001, MNRAS, 325, 531
- Combi, J. A., Albacete Colombo, J. F., Sánchez-Ayaso, E., Romero, G. E., Martí, J., Luque-Escamilla, P. L., Muñoz-Arjonilla, A. J., Sánchez-Sutil, J. R. & López-Santiago, J. 2010, A&A, 523, 76
- Downes, A. 1984, MNRAS, 210, 845
- Dubner, G. M., Moffett, D. A., Goss, W. M. & Winkler, P. F. 1993, AJ, 105, 2251
- Fazio, G. G. et al. 2004, ApJS, 154, 10
- Foster, A. R., Ji, L., Smith, R. K., & Brickhouse, N. S., 2012, ApJ, 756, 128
- Frail, D. A., Goss, W. M., Reynoso, E. M., Giacani, E. B., Green, A. J. & Otrupcek, R. 1996, AJ, 111, 1651
- Freeman, P. E., Kashyap, V., Rosner, R. & Lamb, D. Q. 2002, ApJS, 138, 185
- Fruscione, A. et al. 2006, Proc. SPIE, 6270, 60
- Gabriel, C., et al. 2004, Astronomical Data Analysis Software and Systems (ADASS), XIII, 314, 759
- Garmire, G. P., Bautz, M. W., Ford, P. G., Nousek, J. A. & Ricker, G. R. Jr., 2003, Proc. SPIE, 4851, 28
- Gök, F. & Sezer, A., 2012, MNRAS, 423, 1215
- Green, A. J., Frail, D. A., Goss, W. M. & Otrupcek, R. 1997, AJ, 114, 2058
- Green, D. A. 2009a, ‘A Catalogue of Galactic Supernova Remnants (2009 March version)’, Astrophysics Group, Cavendish Laboratory, Cambridge, United Kingdom (available at ”<http://www.mrao.cam.ac.uk/surveys/snrs/>”).

- Green, D. A. 2009b, *BASI*, 37,45
- Hewitt, J. W., Yusef-Zadeh, F. & Wardle, M. 2008, *ApJ*, 683, 189
- Hewitt, J. W., Rho, J., Andersen, M. & Reach, W. T., 2009, *ApJ*, 694, 1266
- Hewitt, J. W. & *Fermi* LAT Collaboration, 2012, American Astronomical Society Meeting Abstracts, 219, #239.23
- Houck, J. R. et al. 2004, *ApJS*, 154, 18
- Huang, Y.-L. & Thaddeus, P. 1985, *ApJ*, 295, L13
- Jansen, F. et al. 2001, *A&A*, 365, L1
- Kaastra, J. S., Mewe, R. & Nieuwenhuijzen, H, 1996, *UV and X-ray Spectroscopy of Astrophysical and Laboratory Plasmas*, ed. K. Yamashita and T. Watanabe (Universal Academy Press, Tokyo), p. 411
- Kawasaki, M. T., Ozaki, M., Nagase, F., Masai, K., Ishida, M. & Petre, R. et al. 2002, *ApJ*, 572, 897
- Kassim, N. E., Baum, S. A. & Weiler, K. W. 1991, *ApJ*, 374, 212
- Kessler, M. F. et al. 1996, *A&A*, 315, L27
- Kesteven, M. J. L. 1968a, *AuJPh*, 21, 369
- Kesteven, M. J. L. 1968b, *AuJPh*, 21, 739
- Koralesky, B., Frail, D. A., Goss, W. M., Claussen, M. J. & Green, A. J. 1998, *AJ*, 116, 1323
- Liedahl, D. A., Osterheld, A. L. & Goldstein, W. H. 1995, *ApJ*, 438, L115
- Maeda, Y., Baganoff, F. K., Fiegelson, E. D., Morris, M., Bautz, M. W., Brandt, W. N., Burrows, D. N., Doty, J. P. et al. 2002, *ApJ*, 570, 671
- Makishima, K. et al. 1996, *PASJ*, 48, 171
- Mazzotta, P., Mazzitelli, G., Colafrancesco, S. & Vittorio, N. 1998, *A&AS*, 133, 403
- Mewe, R., Gronenschild, E. H. B. M. & van den Oord, G. H. J. 1985, *A&AS*, 62, 197
- Mewe, R., Lemen, J. R., van den Oord, G. H. J. 1986, *A&AS*, 65, 511



- Mill, J., O’Neil, R. R., Price, S. D., Romick, G. J., Uy, O. M. & Gaposchkin, E. M. 1994, *J. Spacecraft Rockets*, 31, 900
- Mills, B. Y. 1981, *PASA*, 4, 156
- Milne, D. K. & Hill, E. R. 1969, *AuJPh*, 22, 211
- Milne, D. K. & Dickel, J. R. 1975, *AuJPh*, 28, 209
- Milne, D. K., Goss, W. M., Haynes, R. F., Wellington, K. J., Caswell, J. L. & Skellern, D. J. 1979, 188, 437
- Morrison, R. & McCammon, D. 1983, *ApJ*, 270, 119
- Ohashi, T. et al. 1996, *PASJ*, 48, 157
- Ohnishi, T., Koyama, K., Tsuru, T. G., Masai, K., Yamaguchi, H. & Ozawa, M. 2011, *PASJ*, 63, 527
- Orlando, S., Bocchino, F., Miceli, M., Reale, F. & Peres, G. 2009, *Memorie della Societa Astronomica Italiana Suppl.*, 13, 97
- Ozawa, M., Koyama, K., Yamaguchi, H., Masai, K. & Tamagawa, T., 2009, *ApJ*, 706, L71
- Pannuti, T. G., Rho, J., Borkowski, K. J. and Cameron, P. B. 2010, *AJ*, 140, 1787
- Raymond, J. C. & Smith, B. W. 1977, *ApJS*, 35, 419
- Reach, W. T., & Rho, J., 2000, *ApJ*, 544, 843
- Reach, W. T., Rho, J., Tappe, A., Pannuti, T. G., Brogan, C. L., Churchwell, E. B., Meade, M. R., Babler, B. et al. 2006, *AJ*, 131, 1479
- Retallack, D. S. 1980, Ph. D Thesis, University of Sydney
- Reynoso, E. M. & Mangum, J. G. 2000, *ApJ*, 545, 874
- Rho, J., Petre, R., Schlegel, E. M., & J. Hester, 1994, *ApJ*, 430, 757
- Rho J. & Petre, R., 1996, *ApJ*, 467, 698
- Rho, J. & Petre, R. 1998, *ApJ*, 503, L167
- Rho, J., Jarrett, T.J., Cutri, R. M. & Reach, W. T. 2001, *ApJ*, 547, 885
- Rho, J. & Borkowski, K. J. 2002, *ApJ*, 575, 201

- Robertson, J. G. 1991, *AuJPh*, 44, 729
- Safi-Harb, S., Dubner, G., Petre, R., Holt, S. S. & Durouchoux, P. 2005, *ApJ*, 618, 321
- Sawada, M. & Koyama, K., 2012, *PASJ*, 64, 81
- Serlemitsos, P. J. et al. 1995, *PASJ*, 47, 105
- Sezer, A., Gök, F., Hudaverdi, M. & Ercan, E. N. 2011a, *MNRAS*, 417, 1387
- Sezer, A., Gök, F., Hudaverdi, M., Kimura, M. & Ercan, E. N. 2011b, *MNRAS*, 415, 301
- Shaver, P. A. & Goss, W. M. 1970a, *AuJPhA*, 14, 1
- Shaver, P. A. & Goss, W. M. 1970b, *AuJPhA*, 14, 77
- Shaver, P. A. & Goss, W. M. 1970c, *AuJPhA*, 14, 133
- Shelton, R. L., Kuntz, K. D., & Petre, R. 2004, *ApJ*, 615, 275
- Strüder, L. et al. 2001, *A&A*, 365, L18
- Tanaka, Y., Inoue, H. & Holt, S. S. 1994, *PASJ*, 46, L37
- Tian, W. W. & Leahy, D. A. 2012, *MNRAS*, 421, 2593
- Tilley, D.A., Balsara, D.S. & Howk, J.C. 2006, *MNRAS*, 371, 1106
- Troja, E., Bocchino, F., Miceli, M., & Reale, F. 2008, *A&A*, 485, 777
- Turner, M. J. L. et al. 2001, *A&A*, 365, L27
- Uchida, H., Tsunemi, H., Katsuda, S., Mori, K. Petre, R. & Yamaguchi, H. 2012, *PASJ*, 64, 61
- Uchiyama, Y., Blandford, R. D., Funk, S., Tajima, H. & Tanaka, T. 2010, *ApJ*, 723, L122
- Vink, J. 2012, *A&AR*, 20, 49
- Weisskopf, M. C., Brinkman, B., Canizares, C., Garmire, G., Murray, S. & van Speybroeck, L. P. 2002, *PASP*, 114, 1
- Weisskopf, M. C., Karovska, M., Pavlov, G. G., Zavlin, V. E. & Clarke, T. 2007, *Ap&SS*, 308, 151
- Werner, M. W. et al. 2004, *ApJS*, 154, 1

- Whiteoak, J. B. Z. & Green, A. J. 1996, A&AS, 118, 329
- Wilson, R. W. 1963, AJ, 68, 181
- Wilson, R. W. & Bolton, J. G. 1960, PASP, 72, 331
- Wu, E. M. H., Hui, C. Y., Tam, P. H. T., Huang, R. H. H., Kong, A. K. H. & Cheng, K. S. 2011, ApJ, 740, L12
- Yamauchi, S., Ueno, M., Koyama, K. & Bamba, A. 2008, PASJ, 60, 1143
- Yamauchi, S., Nobukawa, M., Koyama, K. & Yonemori, M. 2013, PASJ, 65, 6
- Yamaguchi, H., Ozawa, M., Koyama, K., Masai, K., Hiraga, J. S., Ozaki, M., Yonetoku, D, 2009, ApJ, 705, 6

Table 1. Properties of Supernova Remnants

	Kes 17 (G304.6+0.1)	G311.5-0.3	G346.6-0.2	CTB 37A (G348.5+0.1)	G348.5-0.0	References
RA (J2000.0)	13 05 59	14 05 38	17 10 19	17 14 06	17 15 26	(1)
Dec (J2000.0)	−62 42	−61 58	−40 11	−38 32	−38 28	(1)
Angular Diameter (arcmin)	8	5	8	15 <sup>a</sup>	5 <sup>b</sup>	(1)
distance (kpc)	≥9.7	12.5	11	6.3-9.5 <sup>c</sup>	≤6.3	(2), (3), (4), (5)
physical size (pc)	≥23	18	26	21	≤10	(6)
$N_H$ ( $10^{22}$ cm <sup>−2</sup> )	~3.9	~3.0	~1.7	~3.4	...	(6)
$A_V$ (mag)	19.3	11.4	14.3	15	15	(6)

Note. — References: (1) Green (2009a,b), (2) Caswell et al. (1975), (3) Shaver & Goss (1970c), (4) Koralesky et al. (1998), (5) Tian & Leahy (2012), (6) This paper.

<sup>a</sup>This size estimate includes an apparent extension of radio emission seen toward the southwest which resembles a "blow-out" region and may not necessarily be associated with this SNR. In the present paper, we concentrate on the X-ray emission detected from the bright radio shell seen toward the north which is approximately 8 arcminutes in diameter. X-ray emission is clearly detected from this northern portion of the SNR but it is not clearly detected from the southwestern portion. See Section 3.4.2.

<sup>b</sup>This is the approximate size of the bright concave radio rim that defines this SNR.

<sup>c</sup>These are the lower and upper bounds on the distance to CTB 37A based on analysis of the HI absorption profile toward these source (Tian & Leahy 2012). For this paper, we adopt a mean distance of 8 kpc to this SNR.

Table 2. Summary of *ASCA* GIS and SIS Observations of the SNRs<sup>a</sup>

Sequence Number	SNR	Observation Date	Right Ascension (J2000.0)	Declination (J2000.0)	GIS2 Effective Exposure Time (s)	GIS2 Count Rate (counts s <sup>-1</sup> )	GIS3 Effective Exposure Time (s)	GIS2 Count Rate (counts s <sup>-1</sup> )	SIS0 Effective Exposure Time (s)	SIS0 Count Rate (counts s <sup>-1</sup> )
57013000	Kes 17	1999 February 12	13 06 44.2	-62 40 47	24656	$6.5 \times 10^{-2}$	24656	$7.8 \times 10^{-2}$	23328	$5.4 \times 10^{-2}$
56047000	G311.5-0.3	1998 March 2	14 06 18.7	-61 53 02	17858	$4.2 \times 10^{-3}$	17870	$6.2 \times 10^{-3}$	...	...
54004090	G346.6-0.2	1996 September 3	17 09 34.3	-39 59 38	8986	$7.4 \times 10^{-2}$	8986	$6.3 \times 10^{-2}$	...	...

Note. — The units of Right Ascension are hours, minutes and seconds while the units of Declination are degrees, arc minutes and arcseconds. Count rates are for the energy range 0.7-10.0 keV.

<sup>a</sup>No SIS1 data with sufficient signal-to-noise for detailed spectral analysis was available for any of these observations.

Table 3. Summary of *XMM-Newton* MOS1, MOS2 and PN Observations of the SNRs

Sequence Number	SNR	Observation Date	Right Ascension (J2000.0)	Declination (J2000.0)	MOS1 Effective Exposure Time (s)	MOS1 Count Rate (counts s <sup>-1</sup> )	MOS2 Effective Exposure Time (s)	MOS2 Count Rate (counts s <sup>-1</sup> )	PN Exposure Time (s)	PN Effective Count Rate (counts s <sup>-1</sup> )
0303100201	Kes 17	2005 August 25	13 05 40.7	-62 41 36	20176	$1.3 \times 10^{-2}$	19895	$1.1 \times 10^{-2}$	16151	$9.7 \times 10^{-3}$
0306510101	CTB 37A	2006 March 1	17 14 41.0	-38 30 53	3090	$7.7 \times 10^{-2}$	2857	$6.5 \times 10^{-2}$	939	$1.1 \times 10^{-3}$
0306510101	G348.5-0.0	2006 March 1	17 14 41.0	-38 30 53	3090	$< 2.2 \times 10^{-2}$	2857	$< 9.1 \times 10^{-3}$	939	$< 3.3 \times 10^{-2}$

Note. — The units of Right Ascension are hours, minutes and seconds while the units of Declination are degrees, arcminutes and arcseconds. Count rates are for the energy range 0.6-10.0 keV.

Table 4. Summary of *Chandra* ACIS-I Observation of CTB 37A

Sequence Number	ObsID	Observation Date	R.A. (J2000.0)	Decl. (J2000.0)	ACIS-I Effective Exposure Time (s)	ACIS-I Count Rate (s)
500668	6721	2006 October 7	17 14 35.80	−38 31 25	19656	$3.0 \times 10^{-2}$

Note. — The units of Right Ascension are hours, minutes and seconds while the units of Declination are degrees, arcminutes and arcseconds. Count rates are for the energy range 0.3-10.0 keV.

Table 5. Summary of Fits to *ASCA* GIS and SIS Spectra of Kes 17

Model	$N_H$ ( $10^{22} \text{ cm}^{-2}$ )	$kT$ (keV)	$\tau$ ( $10^{12} \text{ cm}^{-3} \text{ s}$ )	Normalization <sup>a</sup>	Abundance	$\chi^2_\nu$ ( $\chi^2/\text{DOF}$ )	Absorbed Flux <sup>b</sup> ( $\text{ergs cm}^{-2} \text{ s}^{-1}$ )	Unabsorbed Flux <sup>b</sup> ( $\text{ergs cm}^{-2} \text{ s}^{-1}$ )	Unabsorbed Luminosity <sup>b</sup> ( $\text{ergs s}^{-1}$ )
PHABS×APEC	$3.48^{+0.46}_{-0.30}$	$0.70^{+0.08}_{-0.11}$	...	$3.58 \times 10^{-2}$	1.0 (frozen)	1.18 (355.08/302)	$2.00 \times 10^{-12}$	$7.96 \times 10^{-11}$	$8.96 \times 10^{35}$
PHABS×APEC	$3.56^{+0.48}_{-0.38}$	$0.63^{+0.09}_{-0.12}$	...	$1.30 \times 10^{-1}$	$0.20^{+0.24}_{-0.12}$	1.12 (338.07/301)	$2.01 \times 10^{-12}$	$7.09 \times 10^{-11}$	$7.98 \times 10^{35}$
PHABS×NEI	$3.72^{+0.38}_{-0.37}$	$0.64^{+0.10}_{-0.08}$	9.60 (>0.5)	$5.34 \times 10^{-2}$	1.0 (frozen)	1.20 (359.74/301)	$1.96 \times 10^{-12}$	$1.15 \times 10^{-10}$	$1.29 \times 10^{36}$
PHABS×NEI	$3.58^{+0.42}_{-0.38}$	$0.63 \pm 0.08$	9.63 (>0.02)	$1.26 \times 10^{-1}$	$0.22^{+0.22}_{-0.13}$	1.13 (340.38/300)	$2.00 \times 10^{-12}$	$7.53 \times 10^{-11}$	$8.48 \times 10^{35}$
PHABS×VAPEC <sup>c</sup>	$4.22^{+1.28}_{-1.02}$	$0.60^{+0.15}_{-0.14}$	...	$6.41 \times 10^{-2}$	Mg= $2.38^{+4.32}_{-1.58}$	1.17 (352.69/301)	$1.89 \times 10^{-12}$	$1.43 \times 10^{-10}$	$1.61 \times 10^{36}$
PHABS×VAPEC <sup>c</sup>	$4.27^{+0.53}_{-0.52}$	$0.56^{+0.10}_{-0.11}$	...	$1.13 \times 10^{-1}$	Si= $0.47^{+0.27}_{-0.19}$ , S= $0.21(<0.56)$	1.11 (334.12/300)	$1.99 \times 10^{-12}$	$2.32 \times 10^{-10}$	$2.61 \times 10^{36}$

Note. — All quoted error bounds correspond to the 90% confidence level.

<sup>a</sup>In the cases of the PHABS×APEC, PHABS×NEI and PHABS×VAPEC models, the normalization is defined in units of  $(10^{-14}/4\pi d^2) \times \int n_e n_p dV$ , where  $d$  is the distance to the source (in units of cm),  $n_e$  and  $n_p$  are the number densities of electrons and hydrogen nuclei, respectively (in units of  $\text{cm}^{-3}$ ) and finally  $\int dV$  is the integral over the entire volume of the X-ray-emitting plasma (in units of  $\text{cm}^{-3}$ ).

<sup>b</sup>For all the considered energy range is 0.7 to 10.0 keV. All luminosities have been calculated assuming a distance of 9.7 kpc to Kes 17.

<sup>c</sup>In the first VAPEC fit listed here, the abundance of magnesium was allowed to vary while the abundances of the other elements were frozen to solar values. In the second VAPEC fit listed here, the abundances of silicon and sulfur were allowed to vary while the abundances of the other elements were frozen to solar values.



Table 6. Summary of Fits to *XMM-Newton* MOS1, MOS2 and PN Spectra of Diffuse X-ray Emission from Kes 17<sup>a</sup>

Model	$N_H$ ( $10^{22}$ cm $^{-2}$ )	$kT$ (keV)	$\tau$ ( $10^{11}$ cm $^{-3}$ s)	Normalization <sup>a</sup>	Abundance	$\chi^2_\nu$ ( $\chi^2/\text{DOF}$ )	Absorbed Flux <sup>b</sup> (ergs cm $^{-2}$ s $^{-1}$ )	Unabsorbed Flux <sup>b</sup> (ergs cm $^{-2}$ s $^{-1}$ )	Unabsorbed Luminosity <sup>b</sup> (ergs s $^{-1}$ )
PHABS×APEC	$3.15^{+0.39}_{-0.18}$	$0.92^{+0.09}_{-0.15}$	...	$1.67 \times 10^{-2}$	1.0 (frozen)	1.10 (308.77/281)	$1.81 \times 10^{-12}$	$3.35 \times 10^{-11}$	$3.77 \times 10^{35}$
PHABS×APEC	$3.29^{+0.33}_{-0.51}$	$0.82^{+0.17}_{-0.10}$	...	$3.17 \times 10^{-2}$	$0.53^{+0.77}_{-0.23}$	1.09 (306.48/280)	$1.76 \times 10^{-12}$	$3.95 \times 10^{-11}$	$4.45 \times 10^{35}$
PHABS×NEI	$3.14^{+0.34}_{-0.38}$	$1.10^{+0.26}_{-0.20}$	$3.70^{+6.30}_{-1.70}$	$1.32 \times 10^{-2}$	1.0 (frozen)	1.08 (303.10/286)	$1.95 \times 10^{-12}$	$2.56 \times 10^{-11}$	$2.88 \times 10^{35}$
PHABS×VAPEC <sup>c</sup>	$3.69^{+0.61}_{-0.65}$	$0.79^{+0.17}_{-0.09}$	...	$2.31 \times 10^{-2}$	Mg= $2.75^{+2.20}_{-1.70}$	1.08 (303.11/280)	$1.77 \times 10^{-12}$	$5.28 \times 10^{-11}$	$5.95 \times 10^{35}$
PHABS×VAPEC <sup>c</sup>	$3.47^{+0.37}_{-0.55}$	$0.80^{+0.25}_{-0.10}$	...	$2.56 \times 10^{-2}$	Si= $0.79^{+0.51}_{-0.27}$ , S= $0.71^{+0.49}_{-0.29}$	1.08 (314.50/291)	$1.77 \times 10^{-12}$	$5.43 \times 10^{-11}$	$6.11 \times 10^{35}$
PHABS×VAPEC <sup>c</sup>	$3.46^{+0.33}_{-0.62}$	$0.90^{+0.08}_{-0.10}$	...	$1.82 \times 10^{-2}$	Mg= $2.76^{+1.22}_{-1.04}$ , Si= $1.08^{+0.21}_{-0.18}$ , S= $0.88^{+0.12}_{-0.24}$	1.09 (302.70/278)	$1.81 \times 10^{-12}$	$5.34 \times 10^{-11}$	$6.02 \times 10^{35}$
PHABS×(VAPEC + POWER LAW) <sup>c</sup>	$3.23^{+0.46}_{-0.58}$	$0.84^{+0.10}_{-0.12}$ $\Gamma=3.98^{+0.24}_{-1.63}$	...	$3.01 \times 10^{-3}$ , $8.01 \times 10^{-3}$	Mg= $9.49(>1.65)$ , Si= $5.17(>0.85)$ , S= $4.88(>0.44)$	1.07 (292.50/274)	$2.05 \times 10^{-12}$	$5.40 \times 10^{-11}$	$6.09 \times 10^{35}$
Reference Fits <sup>d,e</sup>									
WABS×(PSHOCK + POWER LAW) <sup>d</sup>	3.09 (frozen)	0.75 (frozen) $\Gamma=2.4$ (frozen)	21 (frozen)	$1.92 \times 10^{-2}$ , $9.12 \times 10^{-4}$	0.8 (frozen)	1.21 (338.16/280)	$2.23 \times 10^{-12}$	$3.83 \times 10^{-11}$	$4.31 \times 10^{35}$
WABS×(VMEKAL + POWER LAW) <sup>e</sup>	3.77 (frozen)	0.78 (frozen) $\Gamma=1.5$ (frozen)	...	$2.66 \times 10^{-2}$ , $5.32 \times 10^{-5}$	Mg = 1.1 (frozen), Si = 0.97 (frozen), S = 0.50 (frozen)	1.11 (312.68/252)	$1.93 \times 10^{-12}$	$5.77 \times 10^{-11}$	$6.50 \times 10^{35}$
WABS×(PSHOCK + POWER LAW) <sup>d</sup>	$3.67^{+0.52}_{-0.55}$	$0.75^{+0.20}_{-0.12}$ $\Gamma=1.58^{+2.24}_{-0.25}$	1667 (>10)	$3.05 \times 10^{-2}$ , $1.17 \times 10^{-4}$	$0.61^{+0.75}_{-0.44}$	1.11 (305.83/275)	$1.88 \times 10^{-12}$	$4.62 \times 10^{-11}$	$5.76 \times 10^{35}$
WABS×(VMEKAL + POWER LAW) <sup>e</sup>	$3.73^{+0.63}_{-0.54}$	$0.79^{+0.22}_{-0.16}$ $\Gamma=4.16^{+1.22}_{-2.12}$	...	$1.33 \times 10^{-2}$ , $8.08 \times 10^{-3}$	Mg= $4.96(>1.34)$ , Si= $2.18(>0.64)$ , S= $1.95(>0.32)$	1.08 (298.93/276)	$1.92 \times 10^{-12}$	$5.61 \times 10^{-11}$	$6.12 \times 10^{35}$

Note. — All quoted error bounds correspond to the 90% confidence level.

<sup>a</sup>In the cases of the PHABS×APEC, PHABS×NEI, PHABS×VAPEC, PHABS×(VPSHOCK+Power Law) and PHABS×(VMEKAL+Power Law) models, the normalization of the thermal component is defined in units of  $(10^{-14}/4\pi d^2) \times \int n_e n_p dV$ , where  $d$  is the distance to the source (in units of cm),  $n_e$  and  $n_p$  are the number densities of electrons and hydrogen nuclei, respectively (in units of cm $^{-3}$ ) and finally  $\int dV$  is the integral over the entire volume of the X-ray-emitting plasma (in units of cm $^{-3}$ ). Where a power law is present, the normalization is defined in the units of photons keV $^{-1}$  cm $^{-2}$  s $^{-1}$  at 1 keV.

<sup>b</sup>For all the considered energy range is 0.7 to 10.0 keV. All luminosities have been calculated assuming a distance of 9.7 kpc to Kes 17.

<sup>c</sup>In the first VAPEC fit listed here, the abundance of magnesium was allowed to vary while the abundances of the other elements were frozen to solar values. In the second VAPEC fit listed here, the abundances of silicon and sulfur were allowed to vary while the abundances of the other elements were frozen to solar values. In the third VAPEC fit listed here, magnesium, silicon and sulfur were allowed to vary while the abundances of the other elements were frozen to solar values. In the VAPEC×POWER fit listed here, magnesium, silicon and sulfur were allowed to vary while the abundances of the other elements were frozen to solar values.

<sup>d</sup>Fit presented by Combi et al. (2010) in the analysis of MOS1+MOS2+PN spectra of the SNR. Specific fit values for each parameter given here correspond to the values obtained for fits to three different regions of the SNR. The value of the photon index  $\Gamma$  of the power law component is given: the second listed normalization corresponds to this component.

<sup>e</sup>Fit presented by Gök & Sezer (2012) in the analysis of *Suzaku* XIS spectra of the SNR. Specific fit values for each parameter given here correspond to the values obtained for fits to three different regions of the SNR. The value of the photon index  $\Gamma$  of the power law component is given: the second listed normalization corresponds to this component.

Table 7. Summary of Fits to *ASCA* GIS Spectra of G311.5–0.3

Model	$N_H$ ( $10^{22} \text{ cm}^{-2}$ )	$kT$ (keV)	$\Gamma$	Normalization <sup>a</sup>	$\chi^2_\nu$ ( $\chi^2/\text{DOF}$ )	Absorbed Flux <sup>b</sup> (ergs $\text{cm}^{-2} \text{ s}^{-1}$ )	Unabsorbed Flux <sup>b</sup> (ergs $\text{cm}^{-2} \text{ s}^{-1}$ )	Unabsorbed Luminosity <sup>b</sup> (ergs $\text{s}^{-1}$ )
PHABS×Power Law	$3.31^{+6.09}_{-1.91}$	...	$4.82^{+3.78}_{-2.32}$	$4.49 \times 10^{-3}$	0.79 (5.56/7)	$2.25 \times 10^{-13}$	$6.95 \times 10^{-12}$	$1.30 \times 10^{35}$
PHABS×APEC <sup>c</sup>	$2.69^{+1.51}_{-1.59}$	$0.98^{+1.02}_{-0.22}$	...	$1.58 \times 10^{-3}$	0.57 (3.97/7)	$2.23 \times 10^{-13}$	$3.00 \times 10^{-12}$	$5.61 \times 10^{34}$

Note. — All quoted error bounds correspond to the 90% confidence level.

<sup>a</sup>In the case of the PHABS×Power Law model, the normalization is defined in the units of photons  $\text{keV}^{-1} \text{ cm}^{-2} \text{ s}^{-1}$  at 1 keV. In the case of the PHABS×APEC model, the normalization is defined in units of  $(10^{-14}/4\pi d^2) \times \int n_e n_p dV$ , where  $d$  is the distance to the source (in units of cm),  $n_e$  and  $n_p$  are the number densities of electrons and hydrogen nuclei, respectively (in units of  $\text{cm}^{-3}$ ) and finally  $\int dV$  is the integral over the entire volume of the X-ray-emitting plasma (in units of  $\text{cm}^{-3}$ ).

<sup>b</sup>Measured over the energy range of 0.7 to 5.0 keV.

<sup>c</sup>Abundance parameter frozen to solar values.

Table 8. Summary of Fits to *ASCA* GIS Spectra of G346.6–0.2

Model	$N_H$ ( $10^{22} \text{ cm}^{-2}$ )	$kT$ (keV)	$\Gamma$	$\tau$ ( $10^9 \text{ cm}^{-3} \text{ s}$ )	Normalization <sup>a</sup>	Abundance	$\chi^2_\nu$ ( $\chi^2/\text{DOF}$ )	Absorbed Flux <sup>b</sup> ( $\text{ergs cm}^{-2} \text{ s}^{-1}$ )	Unabsorbed Flux <sup>b</sup> ( $\text{ergs cm}^{-2} \text{ s}^{-1}$ )	U L
PHABS×Power Law	$1.54^{+0.50}_{-0.40}$	...	$2.54^{+0.40}_{-0.34}$	...	$7.68 \times 10^{-3}$	...	1.34 (66.78/50)	$9.07 \times 10^{-12}$	$2.35 \times 10^{-10}$	3
PHABS×APEC	$1.39^{+0.33}_{-0.31}$	$2.49^{+0.51}_{-0.39}$	...	...	$1.34 \times 10^{-2}$	1.0 (frozen)	1.45 (72.25/50)	$8.43 \times 10^{-12}$	$1.80 \times 10^{-10}$	2
PHABS×APEC	$1.08^{+0.34}_{-0.30}$	$3.44^{+1.30}_{-0.84}$	...	...	$1.46 \times 10^{-2}$	<0.4	1.22 (59.88/49)	$8.68 \times 10^{-12}$	$1.52 \times 10^{-10}$	2
PHABS×NEI	$2.13^{+0.40}_{-0.68}$	$2.80^{+0.80}_{-0.50}$	...	$7.27^{+6.23}_{-3.77}$	$1.77 \times 10^{-2}$	1.0 (frozen)	1.07 (52.52/49)	$8.66 \times 10^{-12}$	$1.77 \times 10^{-10}$	2
PHABS×NEI	$1.97^{+0.55}_{-0.77}$	$2.82^{+1.14}_{-0.54}$	...	$9.84^{+46}_{-6.44}$	$1.82 \times 10^{-2}$	$0.49^{+1.11}_{-0.45}$	1.07 (51.38/48)	$8.62 \times 10^{-12}$	$1.06 \times 10^{-10}$	1
PHABS×(NEI+Power Law)	$1.77^{+0.40}_{-0.66}$	$1.57^{+0.92}_{-0.40}$	0.5 (frozen)	80 (frozen)	$1.81 \times 10^{-2}$ , $3.43 \times 10^{-4}$	$0.25^{+1.10}_{-0.10}$	1.17 (63.06/54)	$1.43 \times 10^{-11}$	$3.59 \times 10^{-11}$	5
PHABS×(NEI+Power Law)	$1.76^{+0.52}_{-0.70}$	$0.97^{+1.05}_{-0.37}$	2.0 (frozen)	80 (frozen)	$2.42 \times 10^{-3}$ , $4.13 \times 10^{-3}$	2.67 (>0.56)	1.16 (62.37/54)	$1.10 \times 10^{-11}$	$4.46 \times 10^{-11}$	6
PHABS×(NEI+Power Law)	$1.74^{+0.48}_{-0.68}$	$1.50^{+1.00}_{-0.58}$	0.5 (frozen)	100 (frozen)	$1.88 \times 10^{-2}$ , $3.57 \times 10^{-4}$	$0.23^{+1.20}_{-0.05}$	1.19 (64.21/54)	$1.45 \times 10^{-11}$	$3.37 \times 10^{-11}$	4
PHABS×(NEI+Power Law)	$1.79^{+0.56}_{-0.72}$	$0.87^{+0.98}_{-0.33}$	2.0 (frozen)	100 (frozen)	$5.46 \times 10^{-3}$ , $4.09 \times 10^{-3}$	1.32 (>0.42)	1.16 (62.82/54)	$1.09 \times 10^{-11}$	$4.50 \times 10^{-11}$	6
Reference Fits <sup>c,d,e</sup>										
WABS×(VMEKAL +Power Law) <sup>c</sup>	2.0 (frozen)	0.97 (frozen)	0.5 (frozen)	...	$2.29 \times 10^{-2}$ , $4.5 \times 10^{-4}$	Varied <sup>c</sup>	1.16 (65.02/56)	$1.63 \times 10^{-11}$	$4.91 \times 10^{-11}$	7
WABS×(VNEI +Power Law) <sup>d</sup>	2.1 (frozen)	1.22 (frozen)	0.5 (frozen)	292 (frozen)	$2.29 \times 10^{-2}$ , $4.5 \times 10^{-4}$	Varied <sup>d</sup>	1.16 (65.05/56)	$1.63 \times 10^{-11}$	$4.91 \times 10^{-11}$	7
WABS×(VPSHOCK +Power Law) <sup>e</sup>	2.1 (frozen)	1.3 (frozen)	0.6 (frozen)	692 (frozen)	$2.29 \times 10^{-2}$ , $4.5 \times 10^{-4}$	Varied <sup>e</sup>	1.15 (64.50/56)	$1.63 \times 10^{-11}$	$4.91 \times 10^{-11}$	7

Note. — All quoted error bounds correspond to the 90% confidence level.

<sup>a</sup>In the case of the PHABS×Power Law model, the normalization is defined in the units of photons  $\text{keV}^{-1} \text{ cm}^{-2} \text{ s}^{-1}$  at 1 keV. In the cases of the PHABS×APEC and PHABS×NEI normalization is defined in units of  $(10^{-14}/4\pi d^2) \times \int n_e n_p dV$ , where  $d$  is the distance to the source (in units of cm),  $n_e$  and  $n_p$  are the number densities of electrons and hydrogen nuclei, respectively (in units of  $\text{cm}^{-3}$ ) and finally  $\int dV$  is the integral over the entire volume of the X-ray-emitting plasma (in units of  $\text{cm}^{-3}$ ). In the cases of the PHABS×(NEI+Power Law) model and the reference listed normalization is for the NEI component and the second listed normalization is for the Power Law component: these normalizations are defined as above.

<sup>b</sup>For all the considered energy range is 0.6 to 10.0 keV. All luminosities have been calculated assuming a distance of 11 kpc to G346.6–0.2.

<sup>c</sup>These fit parameters are from the fit obtained by Sezer et al. (2011b) to extracted *Suzaku* spectra of this SNR. The fitted variable elemental abundances in that fit are as follows: Mg = 0.65, Si = 0.70, Ca = 3.4 and Fe = 0.4. All of these elemental abundances (as well as the other fit parameters except for the normalizations) were frozen as we applied these spectral fit parameters to the *ASCA* GIS data.

<sup>d</sup>These fit parameters are from the fit obtained by Sezer et al. (2011b) to extracted *Suzaku* spectra of this SNR. The fitted variable elemental abundances  $S = 0.70$ ,  $Ca = 2.3$  and  $Fe = 0.6$ . All of these elemental abundances (as well as the other fit parameters except for the normalizations) were frozen as we applied these parameters to the extracted GIS data.

<sup>e</sup>These fit parameters are from the fit obtained by Sezer et al. (2011b) to extracted *Suzaku* spectra of this SNR. The fitted variable elemental abundances  $S = 0.8$ ,  $Ca = 2.3$  and  $Fe = 0.6$ . Here, the given value for  $\tau$  corresponds to the upper limit on the ionization timescale as derived by those authors. All of these parameters (as well as the other fit parameters except for the normalizations) were frozen as we applied these spectral fit parameters to the extracted GIS data.

Table 9. Summary of Fits to *XMM-Newton* MOS1, MOS2 and PN Spectra of Diffuse X-ray Emission from CTB 37A<sup>a</sup>

Model	$N_H$ ( $10^{22} \text{ cm}^{-2}$ )	$kT$ (keV)	$\tau$ ( $10^{11} \text{ cm}^{-3} \text{ s}$ )	Normalization <sup>b</sup>	Abundance	$\chi^2_\nu$ ( $\chi^2/\text{DOF}$ )	Absorbed Flux <sup>c</sup> ( $\text{ergs cm}^{-2} \text{ s}^{-1}$ )	Unabsorbed Flux <sup>c</sup> ( $\text{ergs cm}^{-2} \text{ s}^{-1}$ )	Unabsorbed Luminosity <sup>c</sup> ( $\text{ergs s}^{-1}$ )
PHABS×APEC	$3.15^{+0.75}_{-0.40}$	$0.73^{+0.15}_{-0.16}$	...	$3.37 \times 10^{-2}$	1.0 (frozen)	1.11 (207.36/192)	$2.32 \times 10^{-12}$	$7.43 \times 10^{-11}$	$5.69 \times 10^{35}$
PHABS×APEC	$3.26^{+0.66}_{-0.56}$	$0.64^{+0.18}_{-0.14}$	...	$1.03 \times 10^{-1}$	$0.29^{+0.43}_{-0.15}$	1.08 (200.04/186)	$2.28 \times 10^{-12}$	$7.73 \times 10^{-11}$	$5.92 \times 10^{35}$
PHABS×NEI	$3.53^{+0.80}_{-0.58}$	$0.62^{+0.21}_{-0.16}$	357 (>3)	$6.29 \times 10^{-2}$	1.0 (frozen)	1.11 (207.13/186)	$2.24 \times 10^{-12}$	$1.35 \times 10^{-10}$	$1.03 \times 10^{36}$
PHABS×NEI	$3.40 \pm 0.60$	$0.64^{+0.16}_{-0.14}$	6.73 (>0.52)	$1.05 \times 10^{-1}$	$0.35^{+0.50}_{-0.20}$	1.09 (201.19/185)	$2.29 \times 10^{-12}$	$9.37 \times 10^{-11}$	$7.18 \times 10^{35}$
PHABS×VAPEC <sup>d</sup>	$3.71^{+0.71}_{-0.56}$	$0.55^{+0.16}_{-0.11}$	...	$9.29 \times 10^{-2}$	Si= $0.48^{+0.26}_{-0.23}$	1.05 (198.98/186)	$2.24 \times 10^{-12}$	$1.91 \times 10^{-10}$	$1.46 \times 10^{36}$
PHABS×VNEI <sup>d</sup>	$3.69^{+0.61}_{-0.49}$	$0.57^{+0.13}_{-0.11}$	43 (>1)	$9.36 \times 10^{-2}$	Si= $0.55^{+0.30}_{-0.27}$	1.07 (198.82/185)	$2.25 \times 10^{-12}$	$1.95 \times 10^{-10}$	$1.49 \times 10^{36}$
Reference Fits <sup>e</sup>									
PHABS×(VMEKAL +Power Law) <sup>e</sup>	2.90 (frozen)	0.63 (frozen) and $\Gamma=1.6$ (frozen)	...	$3.14 \times 10^{-2}$ , $3.40 \times 10^{-4}$	1.0 (frozen)	1.13 (214.80/190)	$3.20 \times 10^{-12}$	$7.41 \times 10^{-11}$	$5.68 \times 10^{35}$

Note. — All quoted error bounds correspond to the 90% confidence level.

<sup>a</sup>X-ray emission from the known hard X-ray source has been excluded when spectra have been extracted.

<sup>b</sup>In the cases of the PHABS×APEC, PHABS×NEI, PHABS×VAPEC, PHABS×VNEI and PHABS×(VMEKAL+Power Law) models, the normalization of the thermal component is defined in units of  $(10^{-14}/4\pi d^2) \times \int n_e n_p dV$ , where  $d$  is the distance to the source (in units of cm),  $n_e$  and  $n_p$  are the number densities of electrons and hydrogen nuclei, respectively (in units of  $\text{cm}^{-3}$ ), and finally  $\int dV$  is the integral over the entire volume of the X-ray-emitting plasma (in units of  $\text{cm}^{-3}$ ). In the case of the PHABS×(VMEKAL+Power Law) model, the normalization of the power law component is defined in units of photons  $\text{keV}^{-1} \text{ cm}^{-2} \text{ s}^{-1}$  at 1 keV.

<sup>c</sup>For the considered energy range 0.7 to 10.0 keV. All luminosities have been calculated assuming a distance of 8 kpc to CTB 37A.

<sup>d</sup>For these fits, the abundances for all elements were frozen to solar except for silicon, which was allowed to vary.

<sup>e</sup>These fit parameters are from the fit obtained by Sezer et al. (2011a) to extracted *Suzaku* spectra of this SNR. All elemental abundances were frozen to solar values and all of the fit parameters (except for the normalizations) were frozen as we applied these spectral fit parameters to the extracted GIS data.



Table 10. Summary of Fits to *Chandra* ACIS-I Spectra of CTB 37A

Model	$N_H$ ( $10^{22}$ cm $^{-2}$ )	$kT$ (keV)	$\Gamma$	$\tau$ ( $10^{11}$ cm $^{-3}$ s)	Normalization <sup>a</sup>	Abundance	$\chi^2_\nu$ ( $\chi^2$ /DOF)	Absorbed Flux <sup>b</sup> (ergs cm $^{-2}$ s $^{-1}$ )	Unabsorbed Flux <sup>b</sup> (ergs cm $^{-2}$ s $^{-1}$ )	Unabsorbed Luminosity <sup>b</sup> (ergs s $^{-1}$ )
CXOU J171419.8–383023										
PHABS×Power Law	$4.08^{+1.32}_{-0.88}$	...	$1.18^{+0.42}_{-0.33}$	...	$3.97 \times 10^{-4}$	...	0.84 (91.97/109)	$2.99 \times 10^{-12}$	$4.49 \times 10^{-12}$	$3.43 \times 10^{34}$
Northeast Region										
PHABS×APEC	$3.07^{+0.23}_{-0.27}$	$0.80^{+0.13}_{-0.08}$	...	...	$1.31 \times 10^{-2}$	1.0 (frozen)	1.09 (144.42/132)	$1.12 \times 10^{-12}$	$1.88 \times 10^{-11}$	$1.44 \times 10^{35}$
PHABS×APEC	$3.03 \pm 0.25$	$0.78^{+0.11}_{-0.08}$	...	...	$2.30 \times 10^{-2}$	$0.45^{+0.45}_{-0.10}$	1.06 (138.81/131)	$1.13 \times 10^{-12}$	$1.64 \times 10^{-11}$	$1.26 \times 10^{35}$
PHABS×NEI	$3.30^{+0.24}_{-0.28}$	$0.83^{+0.20}_{-0.14}$	...	4.15 (>2.55)	$1.53 \times 10^{-2}$	1.0 (frozen)	1.07 (140.38/131)	$1.16 \times 10^{-12}$	$2.42 \times 10^{-11}$	$1.85 \times 10^{35}$
PHABS×NEI	$3.24^{+0.40}_{-0.24}$	$0.80^{+0.13}_{-0.10}$	...	2.44 (>0.25)	$2.63 \times 10^{-2}$	$0.43^{+0.37}_{-0.15}$	1.02 (132.56/130)	$1.16 \times 10^{-12}$	$2.14 \times 10^{-11}$	$1.64 \times 10^{35}$
Southeast Region										
PHABS×APEC	$3.03^{+0.51}_{-0.33}$	$0.57 \pm 0.12$	...	...	$1.79 \times 10^{-2}$	1.0 (frozen)	0.95 (95.32/100)	$7.11 \times 10^{-13}$	$1.55 \times 10^{-11}$	$1.19 \times 10^{35}$
PHABS×APEC	$3.02^{+0.52}_{-0.34}$	$0.57 \pm 0.12$	...	...	$2.30 \times 10^{-2}$	$0.73^{+5.49}_{-0.43}$	0.96 (95.02/99)	$7.12 \times 10^{-13}$	$1.51 \times 10^{-11}$	$1.16 \times 10^{35}$
PHABS×NEI	$3.31^{+0.43}_{-0.36}$	$0.55^{+0.11}_{-0.06}$	...	4.23(>0.86)	$2.76 \times 10^{-2}$	1.0 (frozen)	0.94 (93.08/99)	$7.36 \times 10^{-13}$	$2.51 \times 10^{-11}$	$1.92 \times 10^{35}$
PHABS×NEI	$3.32^{+0.36}_{-0.30}$	$0.55 \pm 0.13$	...	3.34(>0.52)	$2.79 \times 10^{-2}$	0.86 (>0.34)	0.95 (93.04/98)	$7.37 \times 10^{-13}$	$2.55 \times 10^{-11}$	$1.95 \times 10^{35}$

Note. — All quoted error bounds correspond to the 90% confidence level.

<sup>a</sup>In the case of the PHABS×Power Law model, the normalization is defined in the units of photons keV $^{-1}$  cm $^{-2}$  s $^{-1}$  at 1 keV. In the cases of the PHABS×APEC and PHABS×NEI models, the normalization is defined in units of  $(10^{-14}/4\pi d^2) \times \int n_e n_p dV$ , where  $d$  is the distance to the source (in units of cm),  $n_e$  and  $n_p$  are the number densities of electrons and hydrogen nuclei respectively (in units of cm $^{-3}$ ) and finally  $\int dV$  is the integral over the entire volume of the X-ray-emitting plasma (in units of cm $^{-3}$ ).

<sup>b</sup>For CXOU J171319.8–383023, the northeast region and the southeast region, the considered energy ranges are 0.8 to 10.0 keV, 0.9 to 5.0 keV and 0.9 to 4.0 keV, respectively. All luminosities have been calculated assuming a distance of 8 kpc to CTB 37A.

Table 11. Comparison of Derived X-ray Properties with Previously-Published Results

SNR	Properties (This Paper)	Properties (Other Papers)	References	Notes
Kes 17 <sup>a</sup> (G304.6+0.1)	$n_e = 0.42 \text{ cm}^{-3}$ $\tau \sim 10^{12} \text{ s cm}^{-3}$ $t_{rad} = 2.3 \times 10^4 \text{ yr}$ $M_X = 52 M_\odot$	$n_e = 0.9\text{-}2.3 \text{ cm}^{-3}$ $\tau = 1\text{-}3 \times 10^{12} \text{ s cm}^{-3}$ $t = 2.8\text{-}6.4 \times 10^4 \text{ yr}$ $M_X = 8\text{-}15 M_\odot$ $n_e \sim 2.3 f^{-1/2}$ $\tau \sim 10^{12} \text{ s cm}^{-3}$ $t \sim 1.4 \times 10^4 f^{1/2} \text{ yr}$ $M_X \sim 380 f^{1/2} M_\odot$	(1)     (2)	(1) calculated age from $t = \tau/n_e$ .     (2) assumed distance of 10 kpc and adopted $f$ as filling factor.
G346.6–0.2 <sup>b</sup>	$n_e = 0.24 \text{ cm}^{-3}$ $\tau \sim 10^{11} \text{ s cm}^{-3}$ $t_{rad} = 4.7 \times 10^4 \text{ yr}$ $M_X = 84 M_\odot$	$n_e = 0.82 \text{ cm}^{-3}$ $\tau = 2.92 \times 10^{11} \text{ s cm}^{-3}$ $t = 1.1 \times 10^4 \text{ yr}$	(3)	(3) assumed distance of 8.3 kpc and calculated age from $t = \tau/n_e$ .
CTB 37A <sup>c</sup> (G348.5+0.1)	$n_e = 0.77 \text{ cm}^{-3}$ $\tau \geq 10^{12} \text{ s cm}^{-3}$ $t_{rad} = 3.2\text{-}4.2 \times 10^4 \text{ yr}$ $M_X = 76 M_\odot$	$n_e = 1 \text{ cm}^{-3}$ $\tau \geq 10^{12} \text{ s cm}^{-3}$ $t = 3 \times 10^4 \text{ yr}$ $M_X = 530 M_\odot$	(4)	(3) assumed distance of 11.3 kpc and a filling factor $f=1$ . Age calculated from $t = \tau/n_e$ .

Note. — References: (1) – Combi et al. (2010), (2) – Gök & Sezer (2012), (3) – Sezer et al. (2011b), (4) – Sezer et al. (2011a).

<sup>a</sup>Properties calculated based on fits to extracted *XMM-Newton* MOS1+MOS2+PN spectra obtained using PHABS×VAPEC model (with Mg or Si and S thawed). The ionization timescale quoted here for comparison purposes was obtained from a PHABS×NEI fit to the same spectra (see Table 5): this resulting fit suggests that the X-ray emitting plasma associated with Kes 17 is close to ionization equilibrium.

<sup>b</sup>Properties calculated based on fits to extracted *ASCA* GIS2+GIS3 spectra obtained using PHABS×NEI model.

<sup>c</sup>Properties calculated based on fits to extracted *XMM-Newton* MOS1+MOS2+PN spectra obtained using PHABS×VAPEC model (with Mg or Si and S thawed). The estimate of the X-ray-emitting mass associated with CTB 37A that we provide here should be treated as a lower limit: see Section 3.4.2.

Table 12. Properties of the Diffuse Emission from X-ray-Detected SNRs in Present Sample <sup>a</sup>

	Kes 17 (G304.6+0.1)	G311.5-0.3	G346.6-0.2	CTB 37A (G348.5+0.1)
Radius (pc)	$\geq 11$	9	13	10
$V_s$ (km s <sup>-1</sup> , radiative) <sup>b</sup>	150	100, 170	70-100	75-100
$t_{rad}$ (10 <sup>4</sup> yr)	2.3	2.5-4.2	3.3-4.7	3.2-4.2
X-ray Mechanism	Thermal	Likely Thermal	Thermal	Thermal
$kT$ (keV)	0.79-1.10	0.98	2.49-3.44	0.55-0.83
$\tau$ (cm <sup>-3</sup> s)	$3.7 \times 10^{11}$	$\sim > 10^{12}$	$7.3 \times 10^9$	$> 10^{12}$
$n_e$ (cm <sup>-3</sup> )	0.42	$> 0.40$	0.25	0.77
$M_X$ ( $M_\odot$ )	52	13	88	76 <sup>c</sup>
Morphology	Center-Filled	Center-Filled	Center-Filled	Center-Filled
SNR classification	MM SNR	MM SNR	MM SNR	MM SNR
Evidence of Molecular Cloud interaction <sup>b</sup>	Yes (H <sub>2</sub> )	Yes (H <sub>2</sub> )	Yes (H <sub>2</sub> )	Yes (H <sub>2</sub> )
$\gamma$ -ray detection	Yes	No	No	Yes

<sup>a</sup>For the sake of completeness, we note that the fifth SNR considered in this paper (G348.5–0.0) was not detected in the X-ray but – similarly to the four SNRs listed in this table that were detected in the X-ray – evidence exists that G348.5–0.0 is interacting with a molecular cloud.

<sup>b</sup>See Hewitt et al. (2009) and Andersen et al. (2011).

<sup>c</sup>This estimate of the X-ray-emitting mass associated with CTB 37A should be treated as a lower limit: see Section 3.4.2.

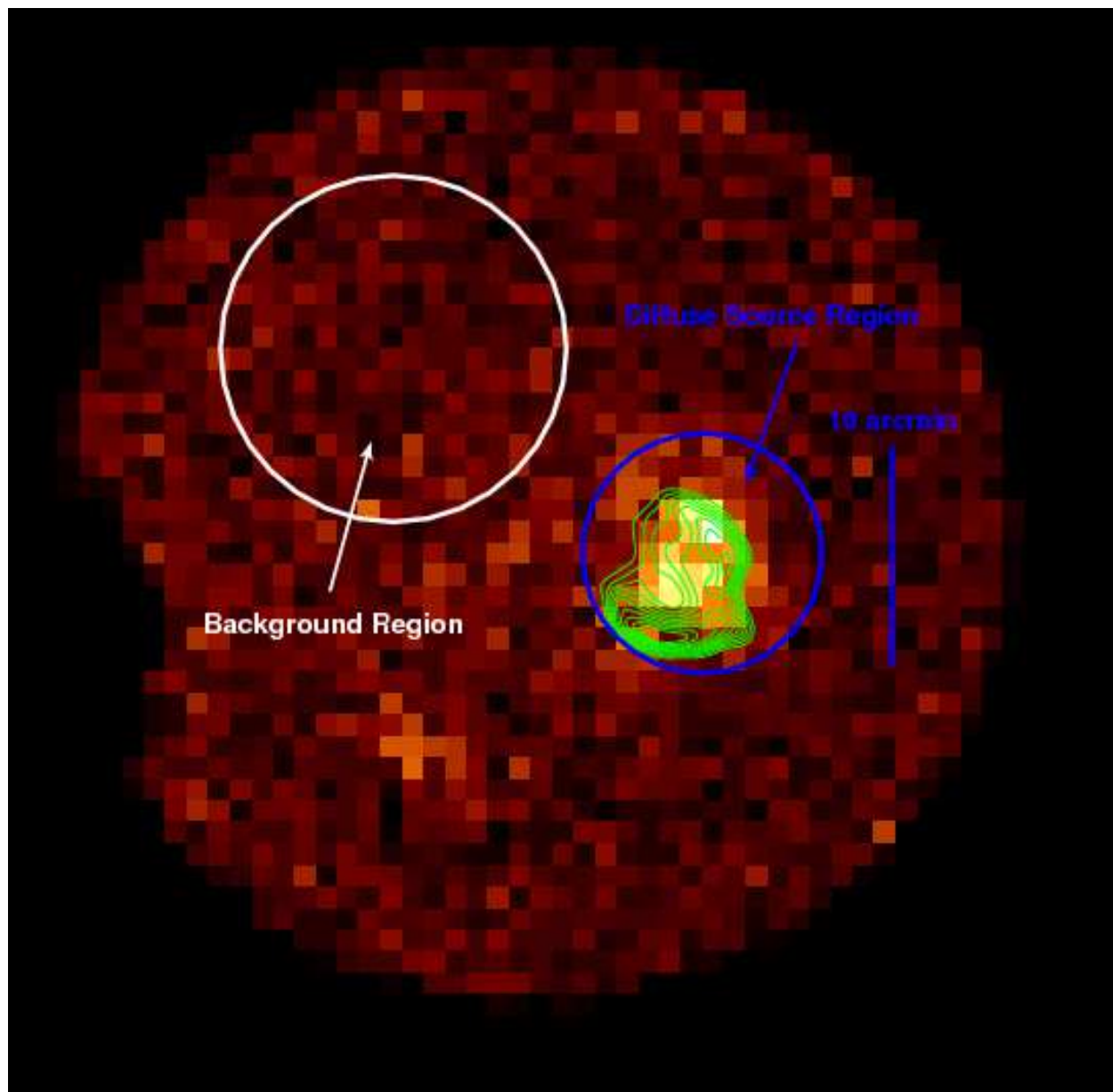


Fig. 1.— *ASCA* GIS2 X-ray image of Kes 17 (in color) for the energy range 0.7 to 10.0 keV. Radio emission (as detected with the MOST at a frequency of 843 MHz) is overlaid on the X-ray emission in green contours. The contour levels correspond to 0.10, 0.15, 0.20, 0.25, 0.30, 0.35, 0.40, 0.45, 0.50 and 0.55 Jy/beam. The region of spectral extraction (namely the entire diffuse region) is indicated. See Section 3.1.1.

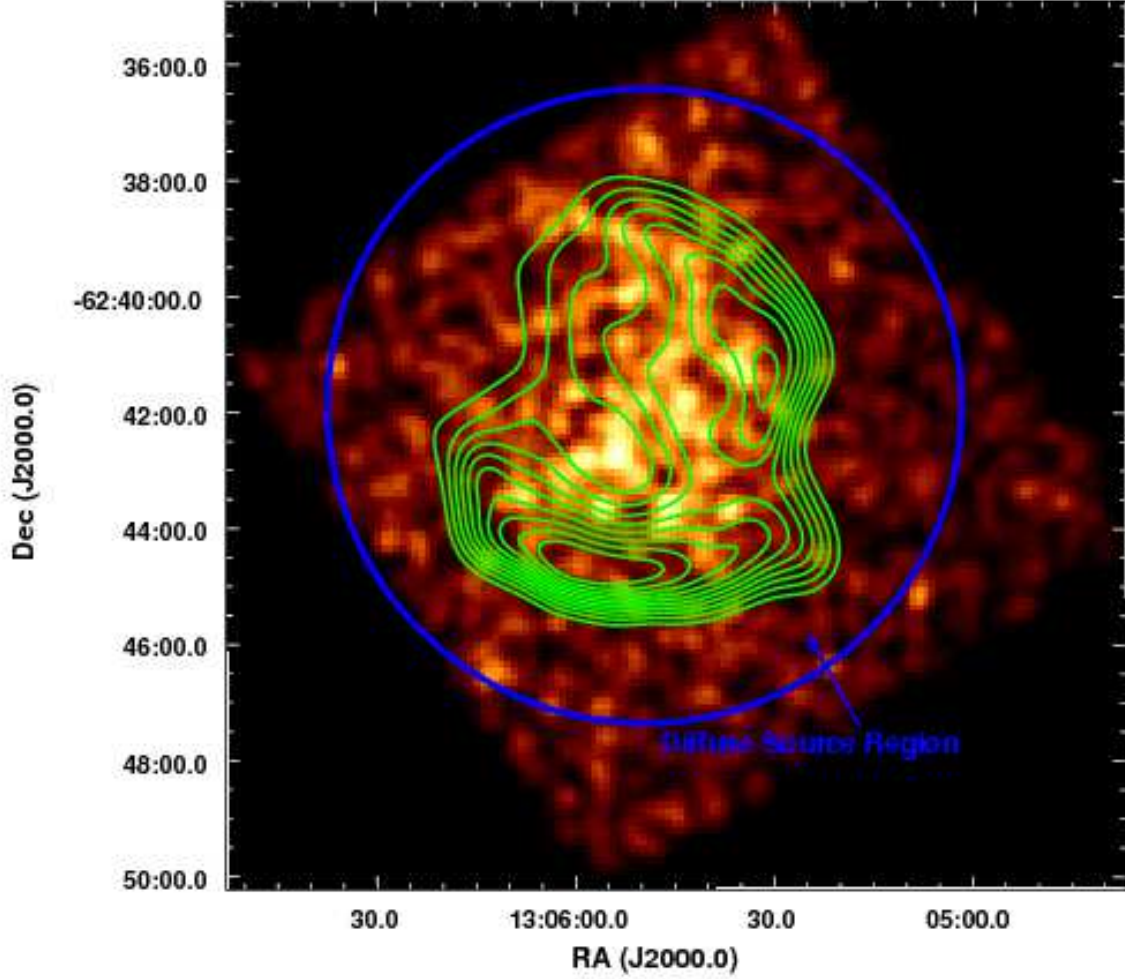


Fig. 2.— *ASCA* SIS0 image of Kes 17 (in color) for the energy range 0.7 to 10.0 keV. Radio emission (as detected with the MOST at a frequency of 843 MHz) is overlaid on the X-ray emission in green contours: the contour levels are the same as those depicted in Figure 1. The region of spectral extraction for the source spectrum (namely the entire diffuse region) is indicated. A background spectrum was extracted from an SIS0 blank sky observation. See Section 3.1.1.

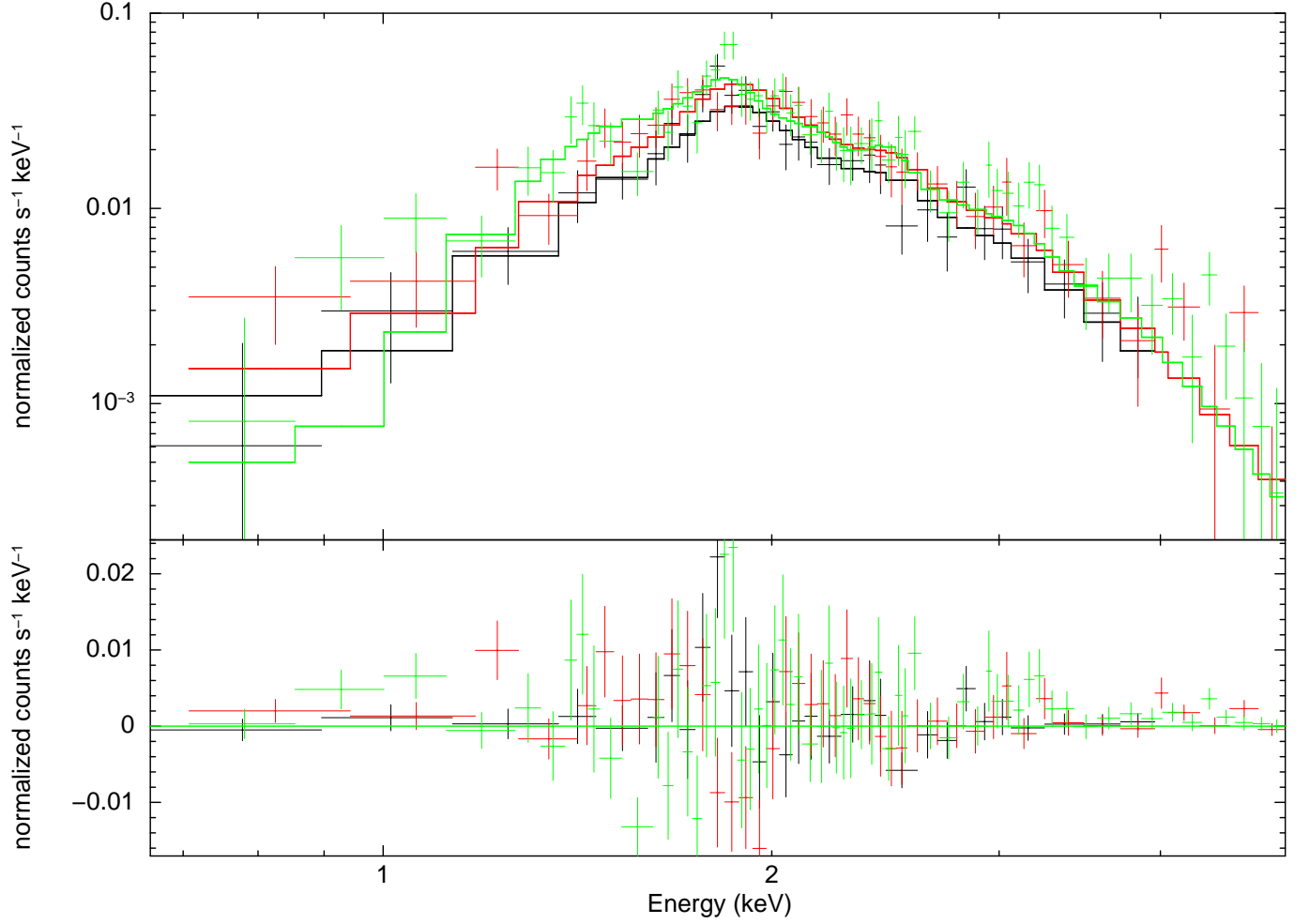


Fig. 3.— *ASCA* GIS2, GIS3 and SIS0 (in black, red and green, respectively) spectra for Kes 17 as fit using a PHABS×APEC model with variable abundance. See Table 5 and Section 3.1.1.



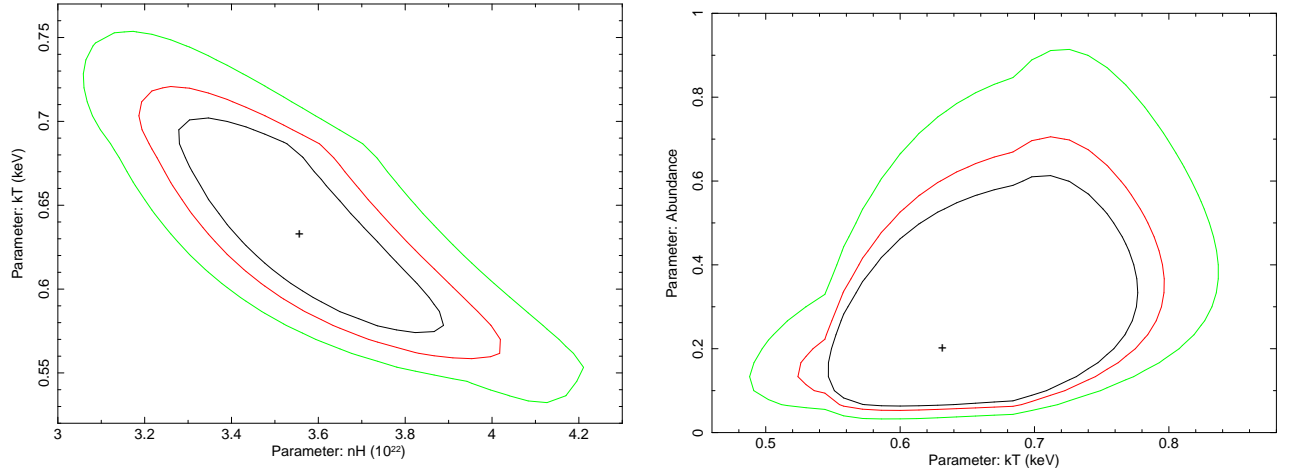


Fig. 4.— Confidence contour plots for column density  $N_H$  versus temperature  $kT$  (left) and abundance versus temperature  $kT$  (right) for the fit generated using the PHABS×APEC model with variable abundances to the *ASCA* GIS2, GIS3 and SIS0 spectra of Kes 17. See Figure 3, Table 5 and Section 3.1.1.

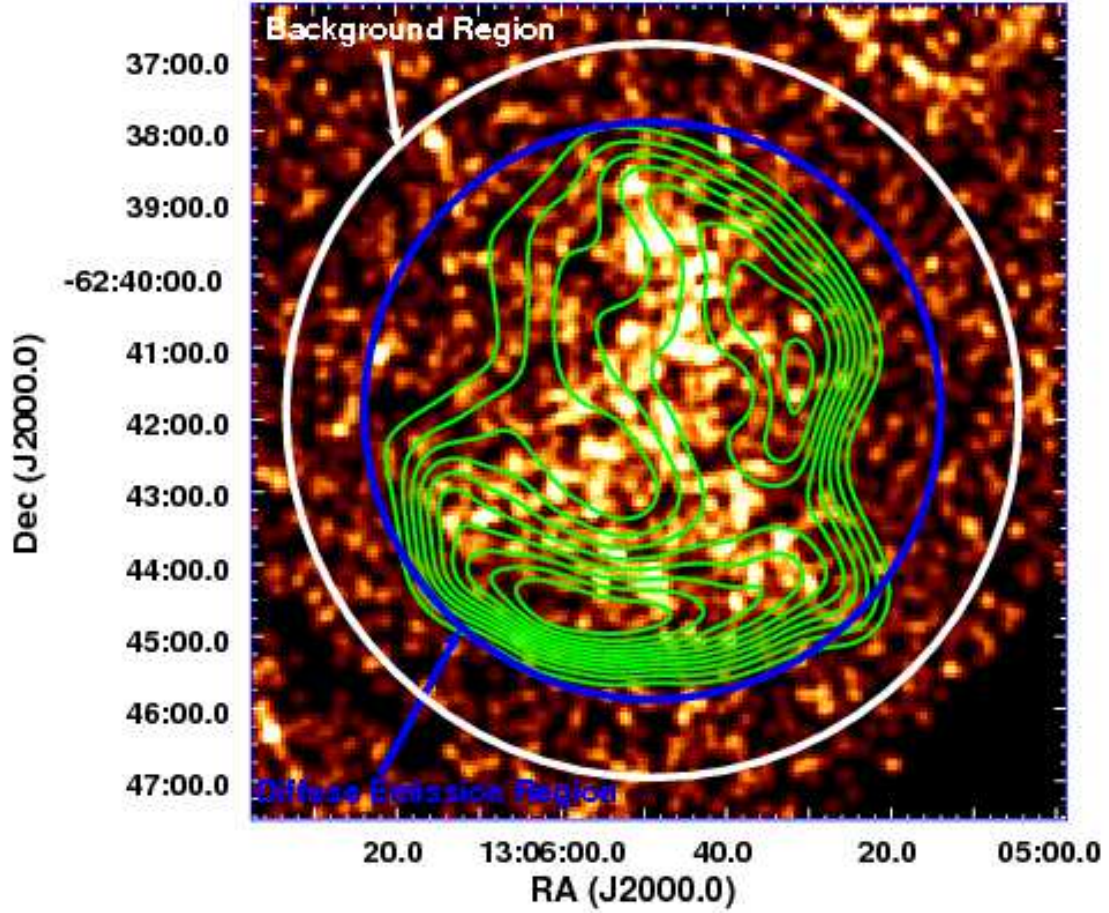


Fig. 5.— *XMM-Newton* MOS1 image of Kes 17 (in color) for the energy range 0.7 to 10.0 keV. Radio emission (as detected with the MOST at a frequency of 843 MHz) is overlaid on the X-ray emission in green contours: the contour levels are the same as those depicted in Figure 1. Regions of spectral extraction (namely the entire diffuse region and the background region) are indicated. See Section 3.1.1.

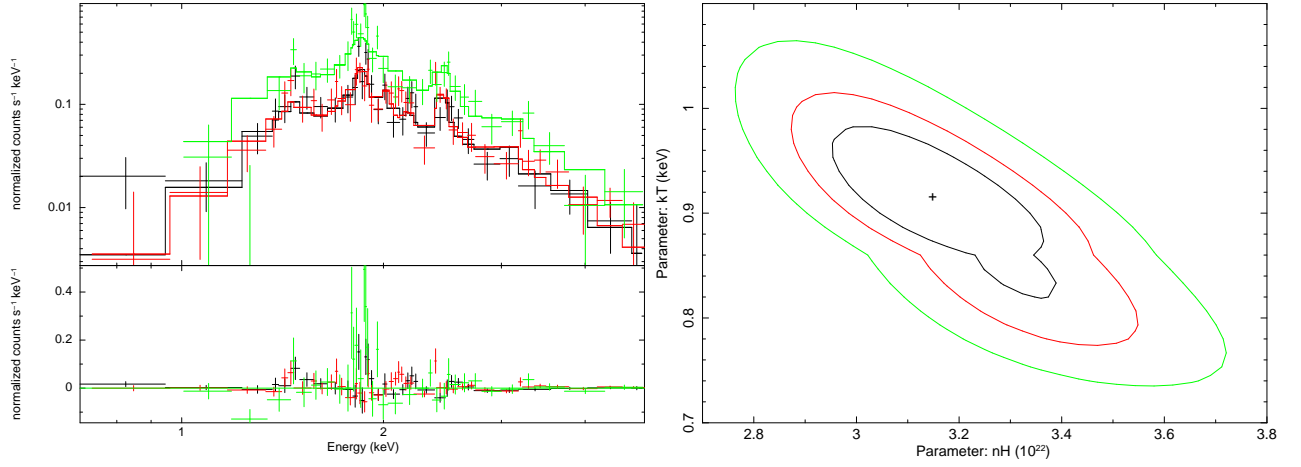


Fig. 6.— (left) *XMM-Newton* MOS1, MOS2 and PN (in black, red and green, respectively) spectra of diffuse emission from Kes 17 as fit with the PHABS×APEC model. (right) Confidence contour plots for column density  $N_H$  versus temperature  $kT$  for the PHABS×APEC fit. The contours are plotted at the  $1\sigma$ ,  $2\sigma$  and  $3\sigma$  levels. See Table 6 and Section 3.1.1.

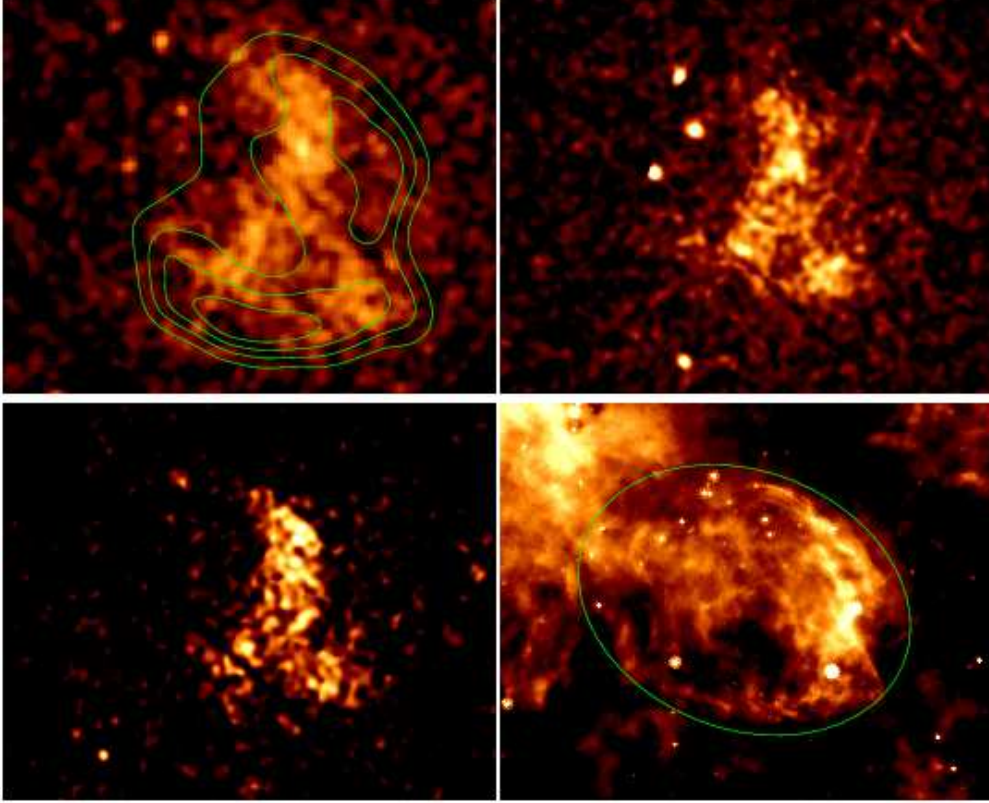


Fig. 7.— (Top panel) Multiwavelength images of Kes 17. (a-upper left), (b-upper right) and (c-lower left): *XMM-Newton* X-ray images of Kes 17 in the (a) total band (with radio contours overlaid), (b) soft band (0.5-2 keV), and (c) hard band (2-6 keV). (d - lower right) *Spitzer* MIPS  $24\mu\text{m}$  image with a green ellipse to demarcate the emission that is plausibly associated with the SNR. The image is centered on RA (J2000.0)  $13^h 05^m 58^s.3$ , Dec (J2000.0)  $-62^\circ 42' 08''.8$  and the field of view is  $12'$ . See Section 3.1.1.



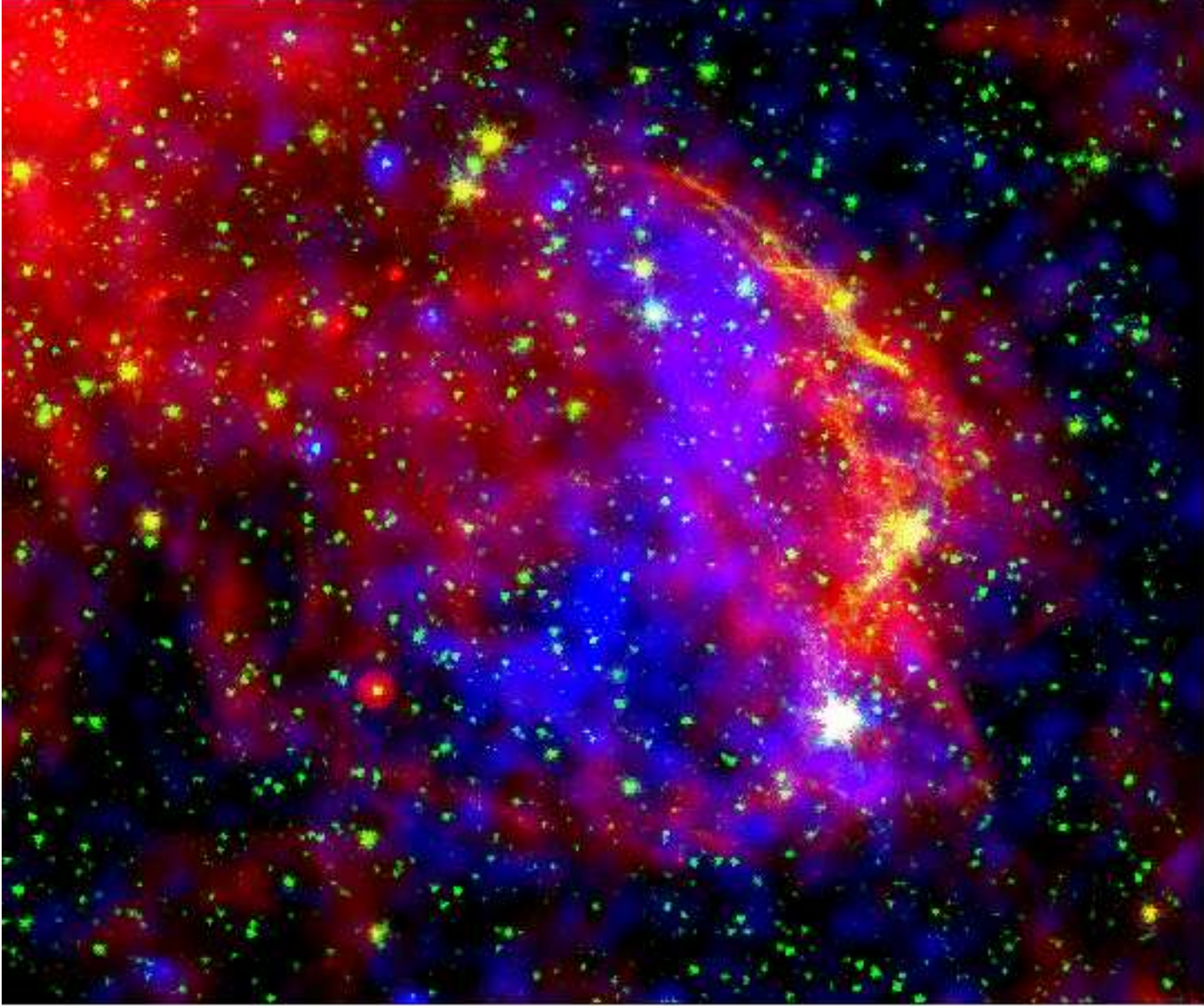


Fig. 8.— Mosaicked three color images of Kes 17. Blue, green and red represent *XMM-Newton* X-ray (total band), *Spitzer* MIPS at  $24\mu\text{m}$  and IRAC  $4.5\mu\text{m}$  images (from Reach et al. (2006) and Andersen et al. (2011), respectively). Note that the observed X-ray emission may be described as center-filled within infrared radiative shells. See Section 3.1.1.

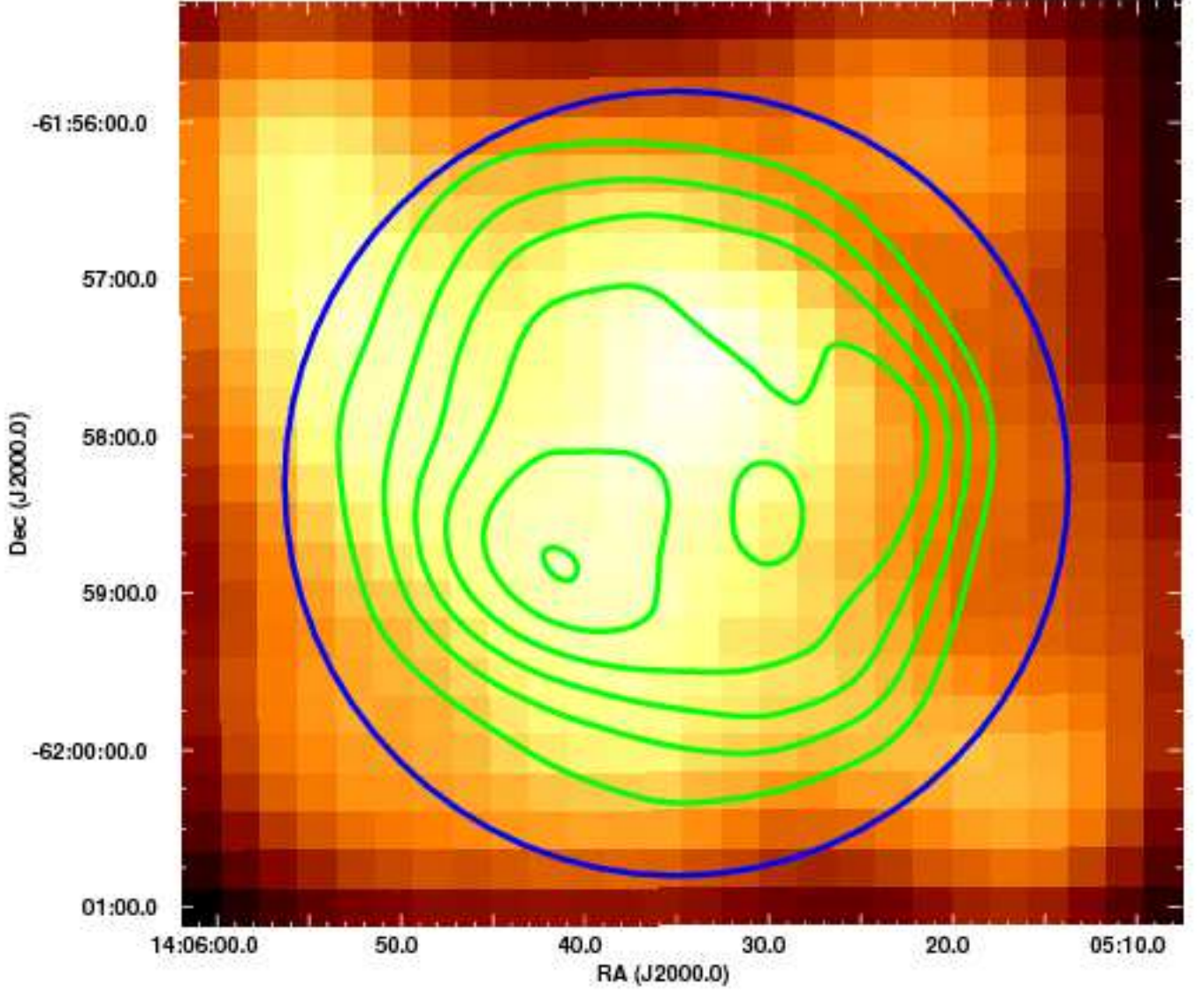


Fig. 9.— *ASCA* GIS2+GIS3 co-added X-ray image of G311.5–0.3 (in color) for the energy range 0.6 to 10.0 keV. Radio emission (as detected with the MOST at a frequency of 843 MHz) is overlaid on the X-ray emission in green contours. The pixel range of the X-ray emission is 0.01 to 0.08 counts arcmin<sup>−2</sup> and the radio contours are at the levels of 0.05, 0.10, 0.15, 0.20, 0.25 and 0.29 Jy/beam. The blue circle (with a radius of 2.5 arcminutes) indicates the region of spectral extraction of the GIS2 and GIS3 spectra. See Section 3.2.1.

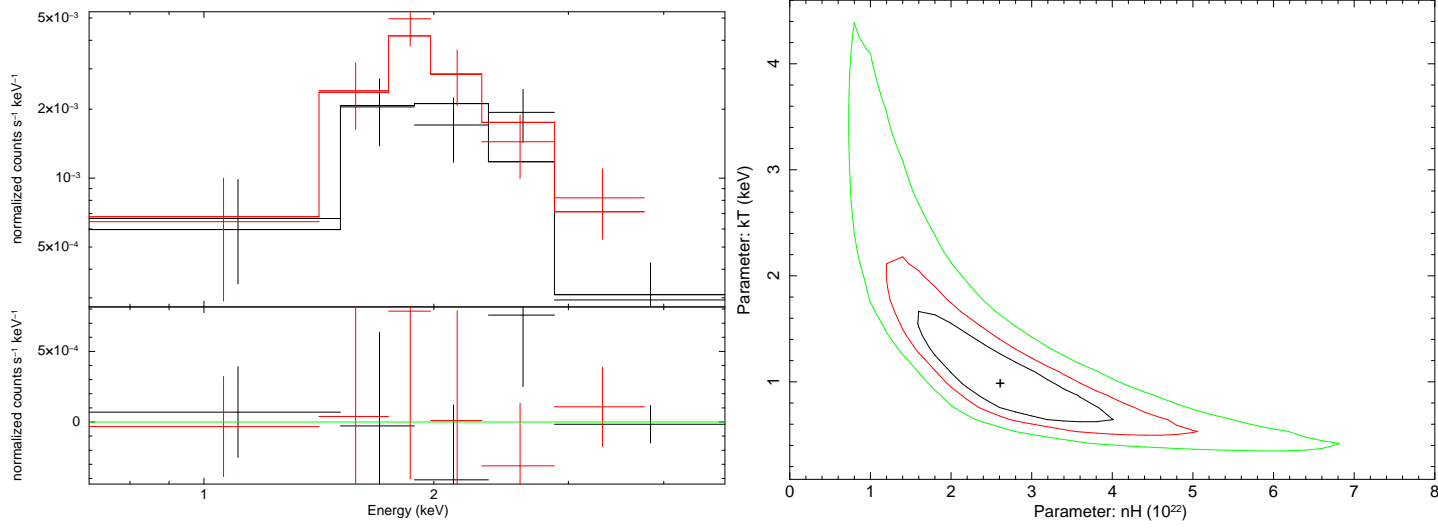


Fig. 10.— (left) *ASCA* GIS2 and GIS3 (in black and red, respectively) spectra for G311.5–0.3 as fit using the PHABS×APEC model. (right) Confidence contour plot for column density  $N_H$  versus temperature  $kT$  for the fit generated using the PHABS×APEC model. See Table 7 and see Section 3.2.1.

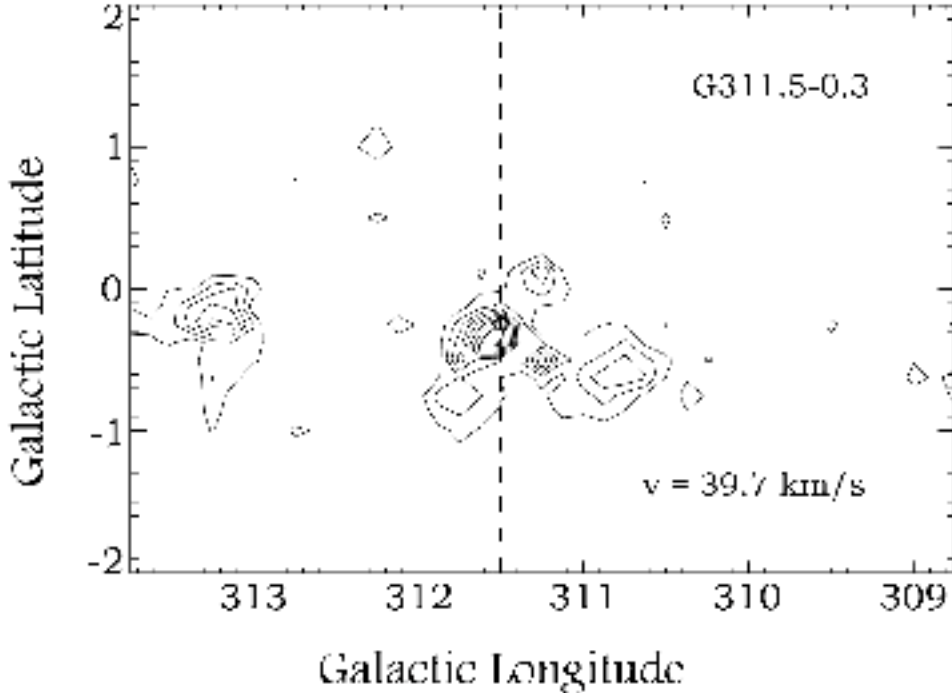


Fig. 11.— CO map of G311.5-0.3 for the velocity  $v = 39.7 \text{ km s}^{-1}$ . The position of G311.5–0.3 is indicated by the intersection of the dashed line. Notice the giant molecular cloud (GMC) located in proximity to G311.5–0.3. See Section 3.2.1.



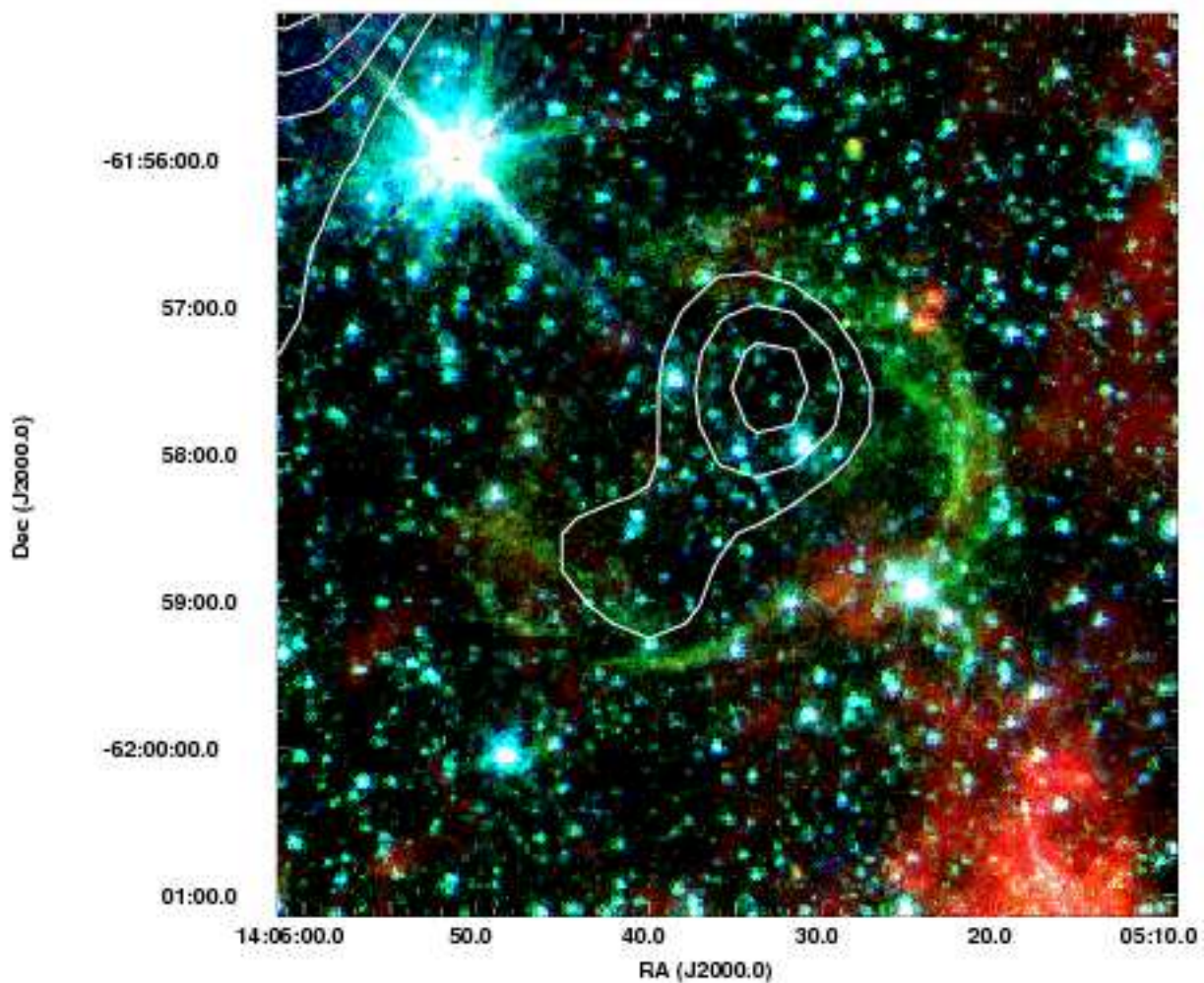


Fig. 12.— *Spitzer* IRAC three color image of G311.5-0.3 (from Reach et al. (2006)) with *ASCA* GIS X-ray contours overlaid. In this image, the red, green and blue correspond to emission detected at  $8\mu\text{m}$ ,  $4.5\mu\text{m}$  and  $3.5\mu\text{m}$ , respectively. Notice the center-filled X-ray morphology which is characteristic of mixed-morphology SNRs. See Section 3.2.1.

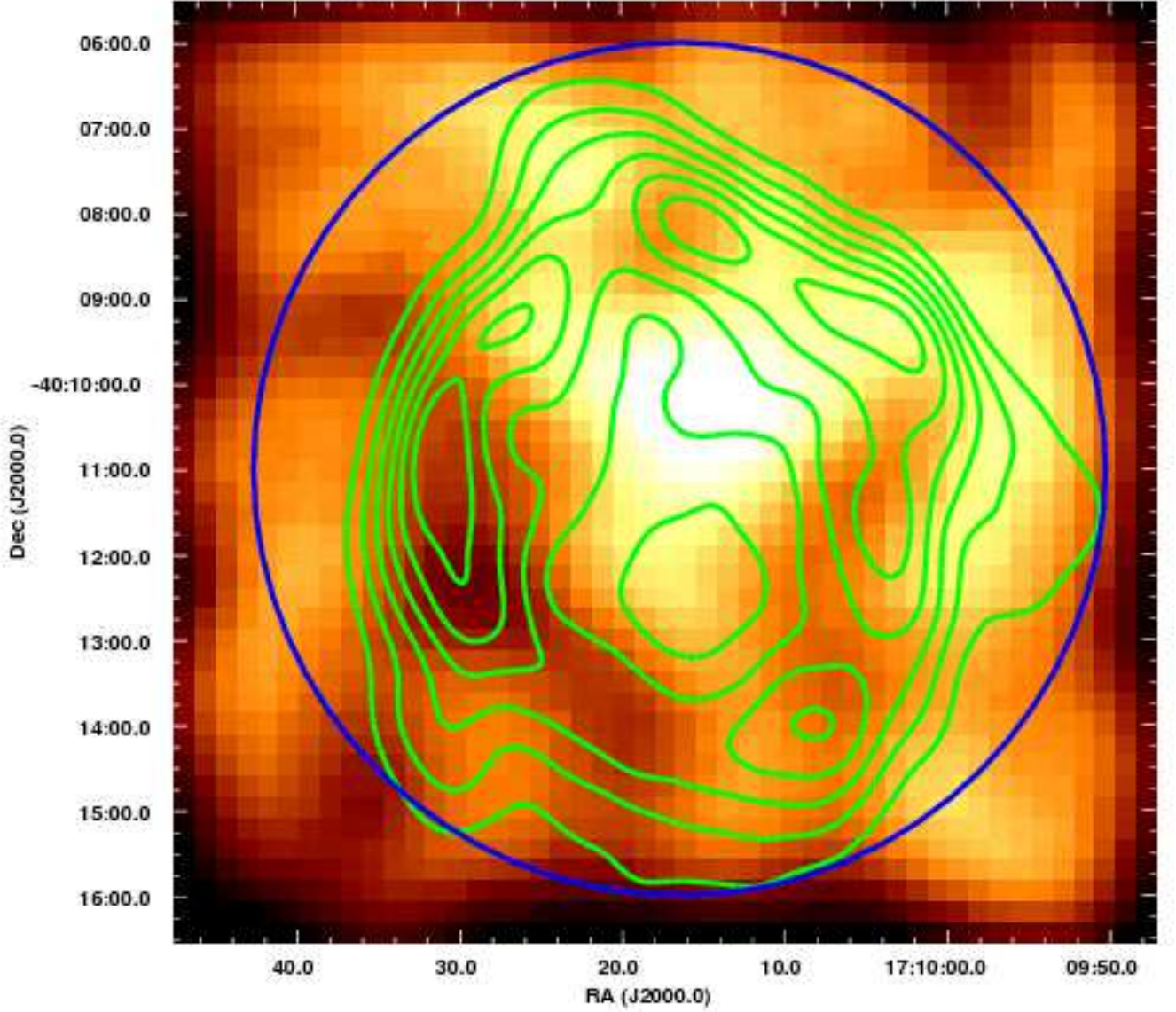


Fig. 13.— *ASCA* GIS2+GIS3 co-added X-ray image of G346.6–0.2 (in color) for the energy range 0.6 to 10.0 keV. Radio emission (as detected with the MOST at a frequency of 843 MHz) is overlaid on the X-ray emission in green contours. The pixel range of the X-ray emission is 0.02 to 0.10 counts arcmin<sup>−2</sup> and the radio contours are at the levels of 0.04, 0.08, 0.12, 0.16, 0.20 and 0.24 Jy/beam. The blue circle (with a radius of 5 arcminutes) indicates the region of spectral extraction of the GIS2 and GIS3 spectra. See Section 3.3.1.

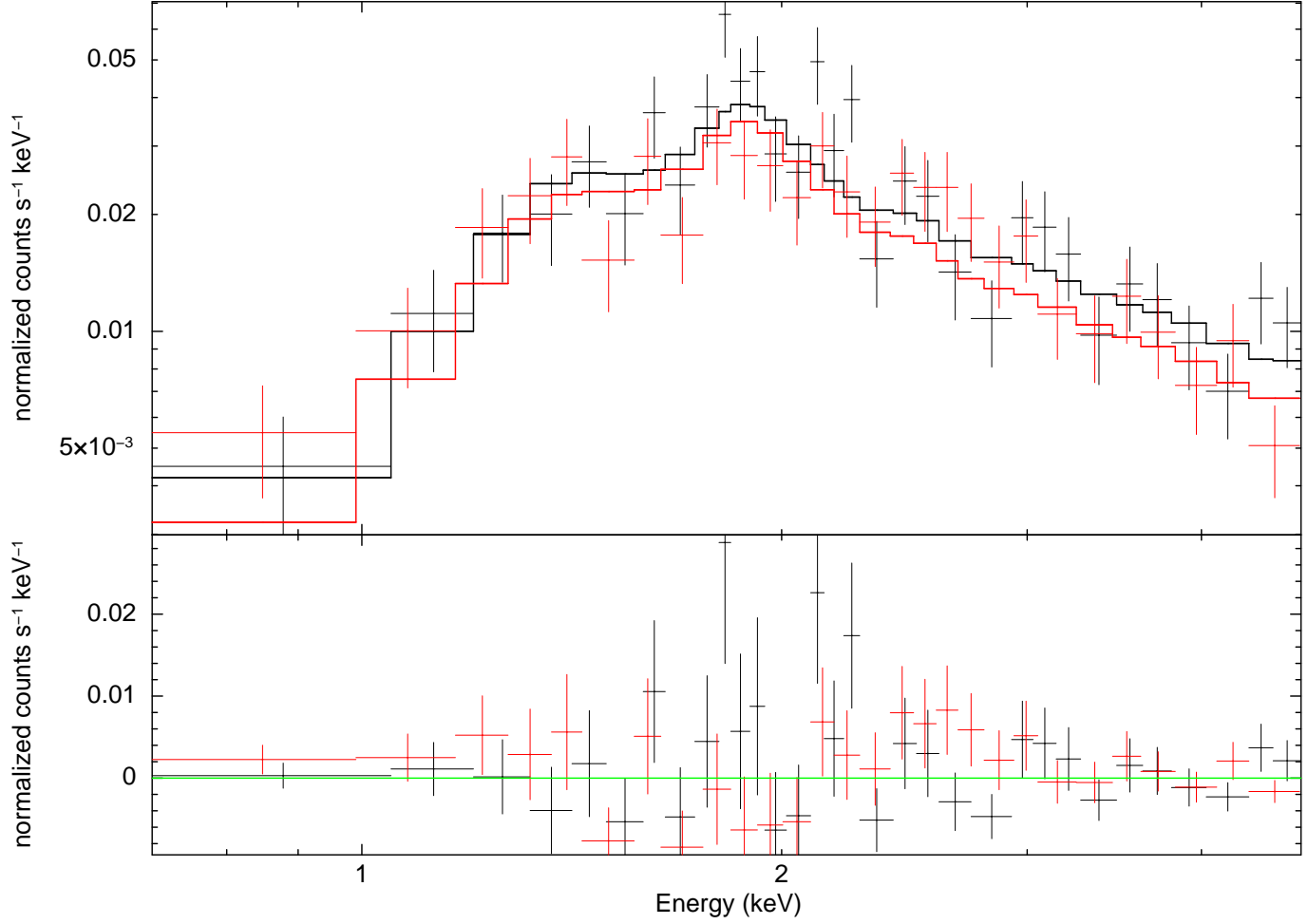


Fig. 14.— *ASCA* GIS2 and GIS3 (in black and red, respectively) spectra for G346.6–0.2 as fit using a PHABS×(NEI+Power Law) model. In this fit, the ionization timescale has been frozen to  $\tau = 8 \times 10^{10} \text{ cm}^{-3} \text{ s}$  and the photon index has been frozen to  $\Gamma=0.5$ . See Table 8 and Section 3.3.2.



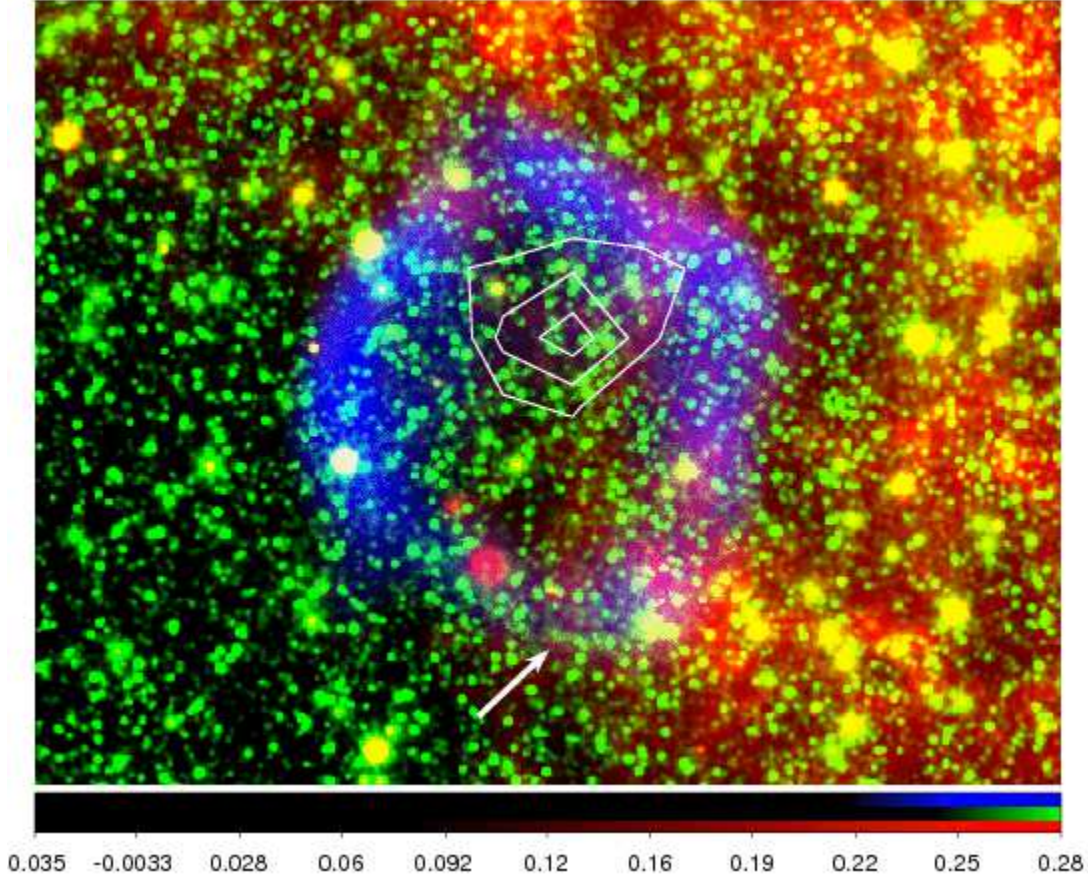


Fig. 15.— Mosaicked three color images of G346.6-0.2 superposed on *ASCA* GIS2+GIS3 X-ray contours. Red, green and blue represent images of *Spitzer* MIPS at 24  $\mu\text{m}$ , IRAC at 4.6  $\mu\text{m}$  (Reach et al. 2006) and radio (Green et al. 1997), respectively. The arrow indicates the location where emission from molecular hydrogen is detected (Andersen et al. 2011). See Section 3.3.1.

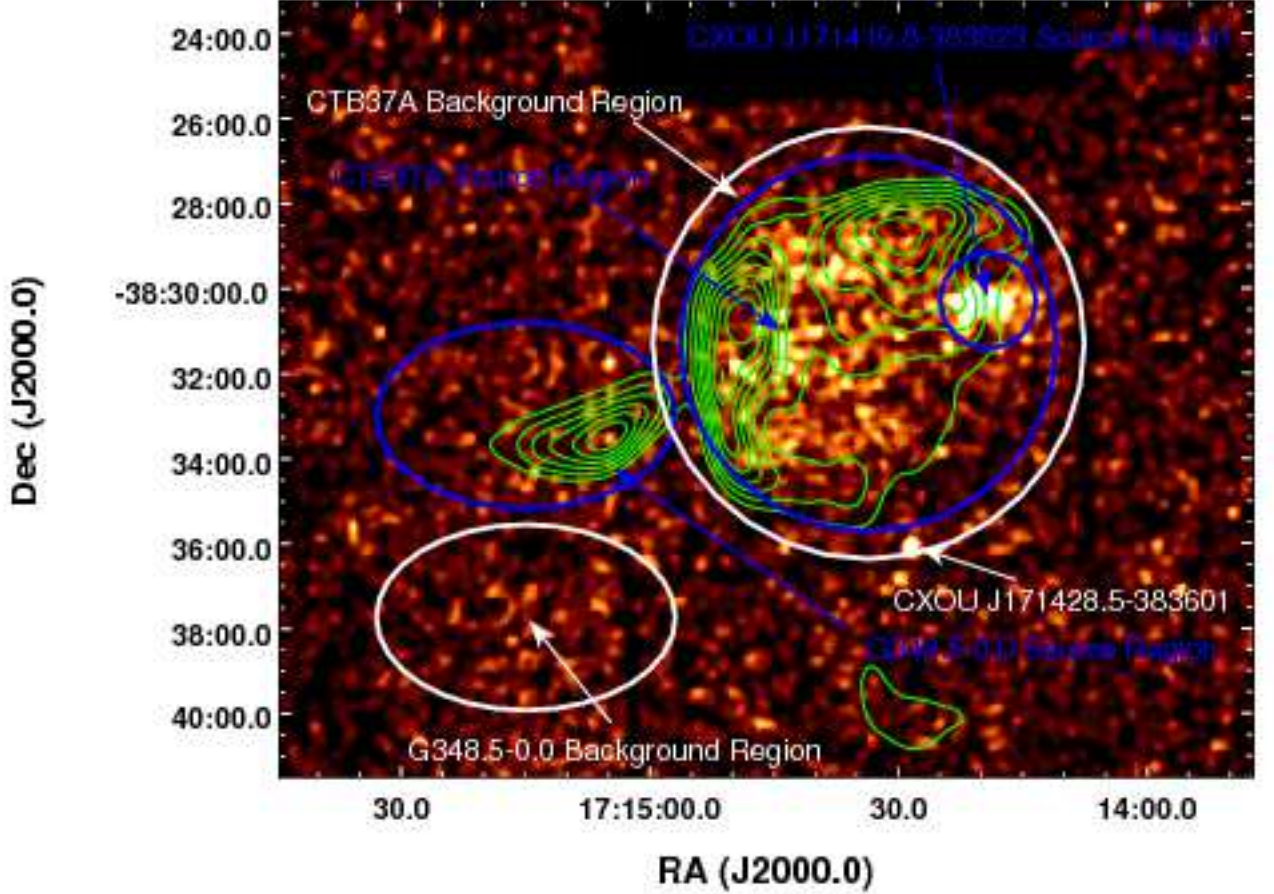


Fig. 16.— *XMM-Newton* MOS1 image (in color) of CTB 37A and G348.5–0.0 for the energy range 0.7 to 10.0 keV. Radio emission (as detected with the MOST at a frequency of 843 MHz) is overlaid on the X-ray emission in white contours. The radio contours are at the level of 0.4, 0.6, 0.8, 1.0, 1.2, 1.4, 1.6, 1.8 and 2.0 Jy/beam. Notice the crescent-shape filament of radio emission located due east of CTB 37A: this filament corresponds to the separate SNR G348.5–0.0. Regions of spectral extraction – namely the entire source region for CTB 37A, the extended source CXOU J171419.8–383023 (associated with the northwestern rim of the SNR), the extended source region for G348.5–0.0 and the corresponding background regions – are indicated. See Sections 3.4.1 and 3.5.



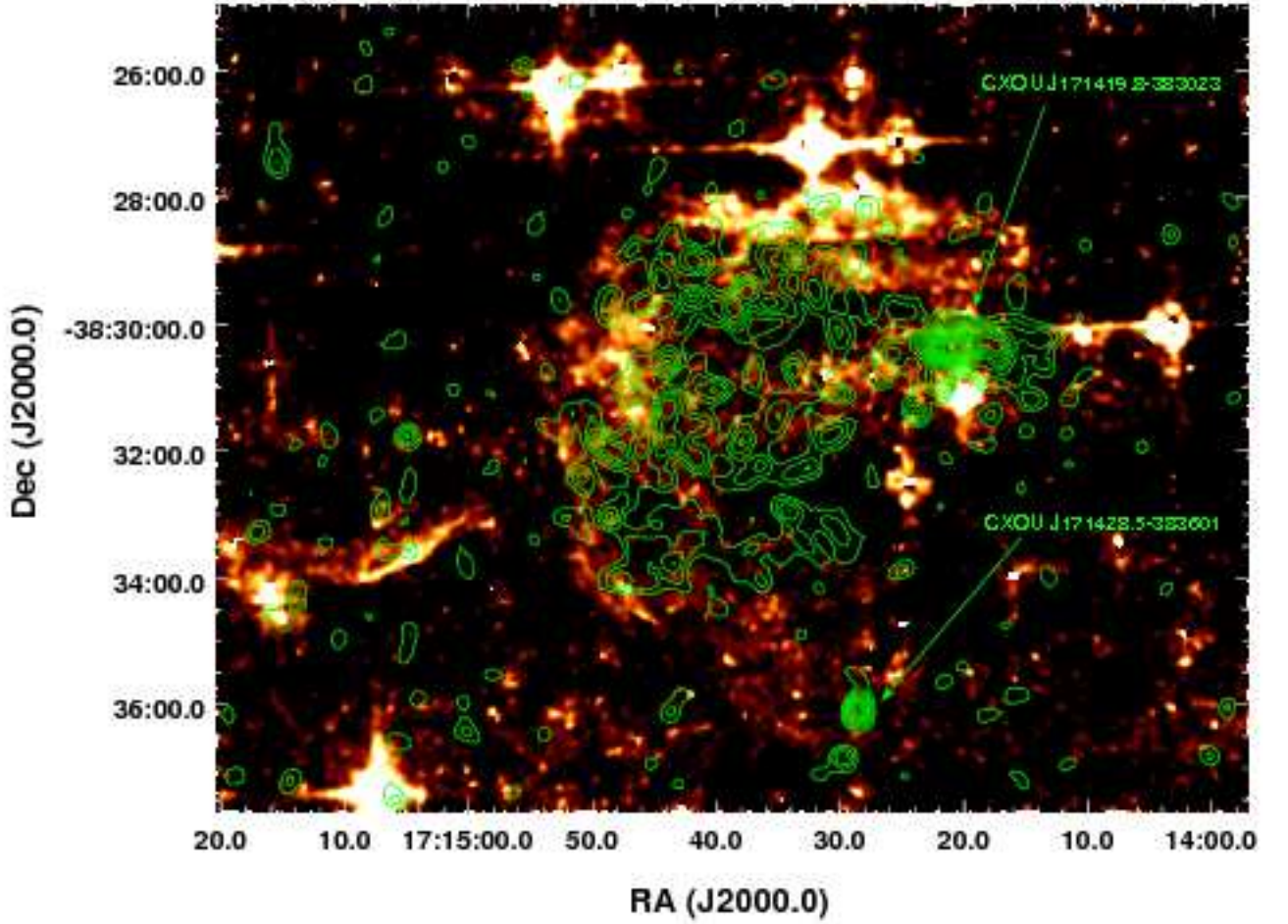


Fig. 17.— Infrared *Spitzer* IRAC Channel 3 ( $5.8\mu\text{m}$ ) color image of CTB 37A with *XMM-Newton* MOS1 X-ray emission overlaid in contours. The contour levels are set at 0.12 to 0.80 counts per pixel (in steps of 0.04). The locations of the X-ray source CXOU J171419.8–383023 (associated with the northwestern rim of the SNR) and CXOU J171428.5–383601 (the southern discrete hard X-ray source) are both indicated. The crescent shape of infrared emission seen toward the east in the image is physically associated with the SNR G348.5–0.0. See Sections 3.4.1 and 3.5.

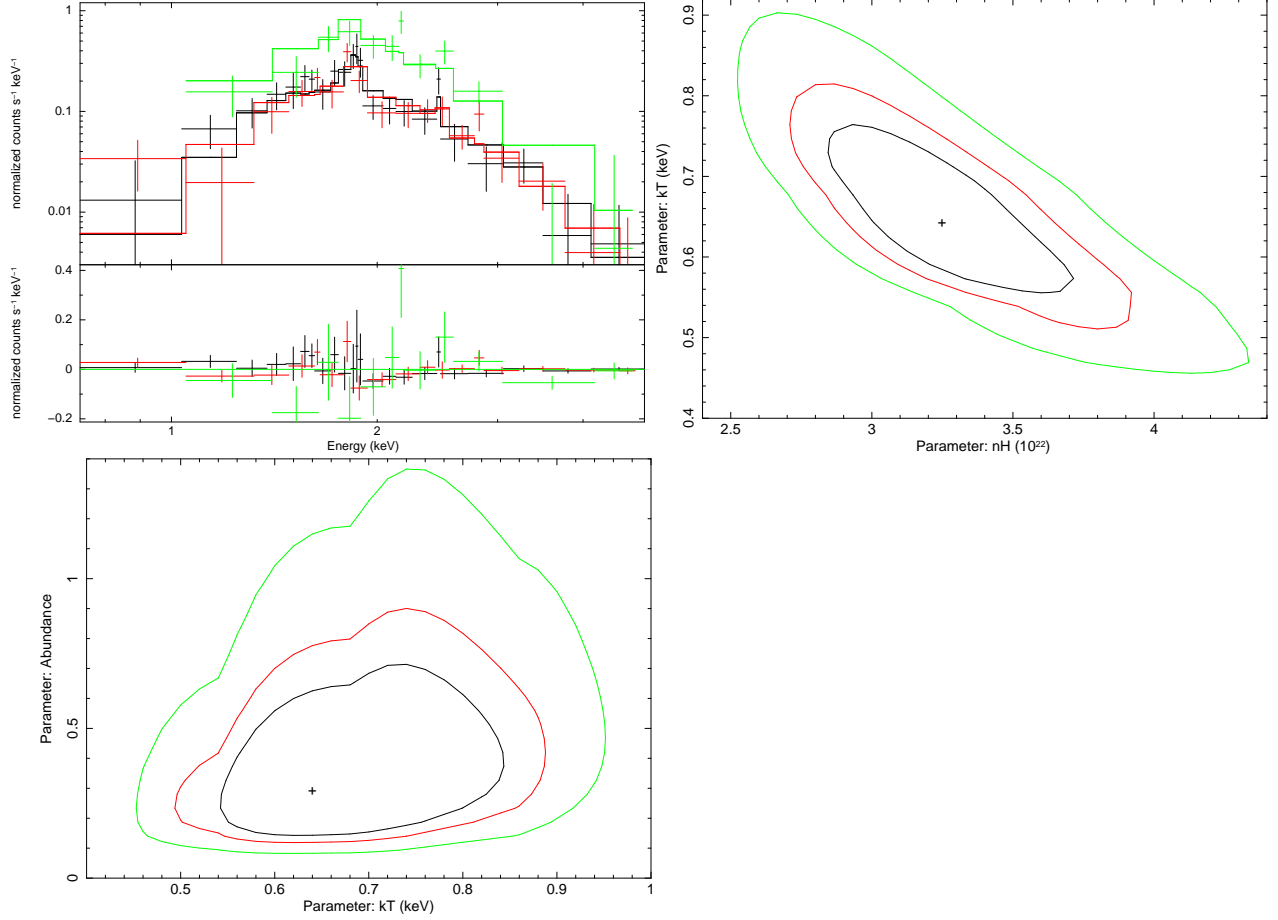


Fig. 18.— (top left) *XMM-Newton* MOS1, MOS2 and PN spectra of CTB 37A as fit with a PHABS×APEC model with variable abundance. (top right) Confidence contour plot for column density  $N_H$  versus temperature  $kT$ . (bottom left) Confidence contour plot for column density  $N_H$  versus abundance. See Table 9 and Section 3.4.1.



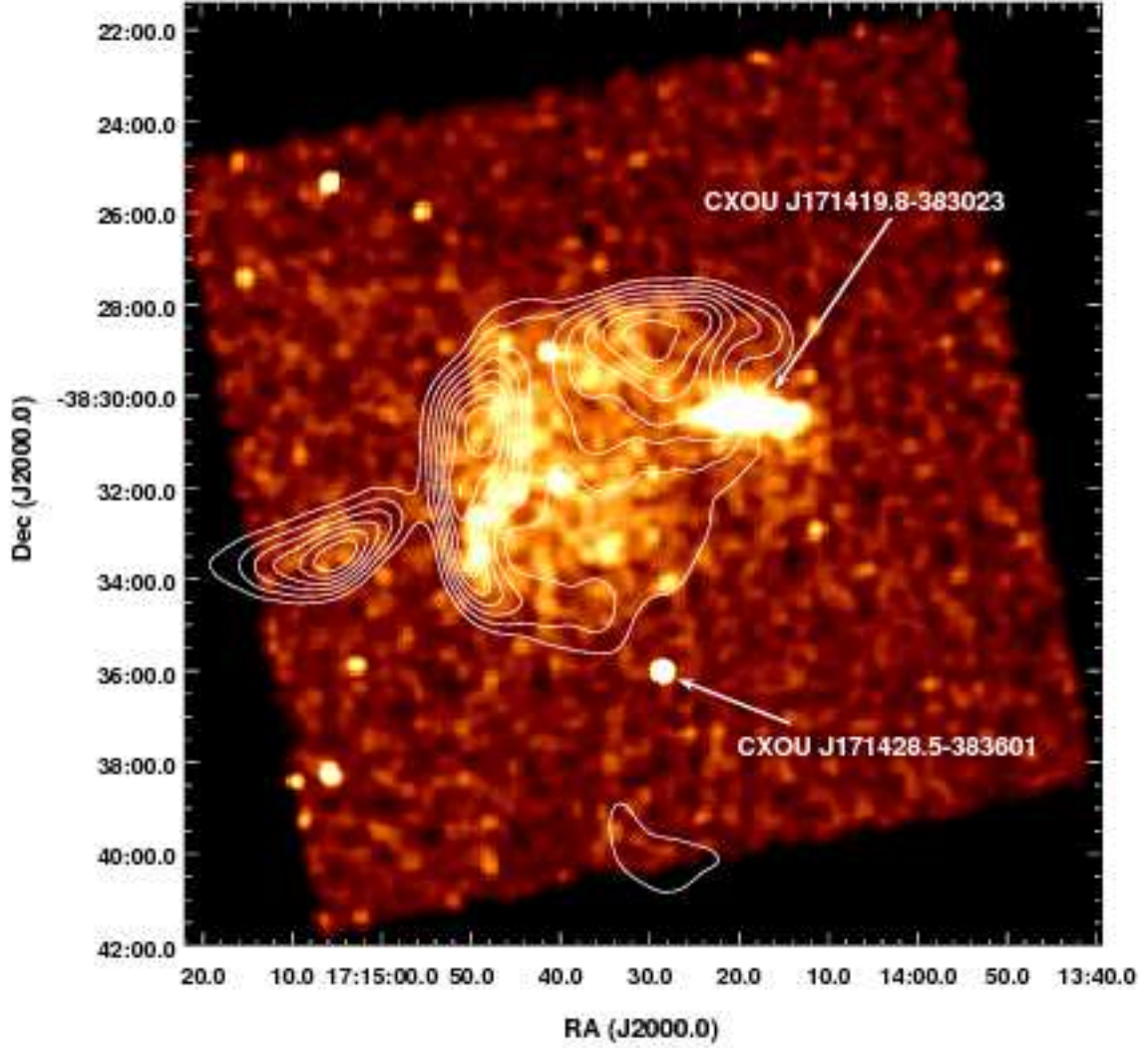


Fig. 19.— Exposure-corrected *Chandra* ACIS-I image of CTB37A (in color) for the energy range 0.5 to 10.0 keV. Radio emission (as detected with the MOST at a frequency of 843 MHz) is overlaid on the X-ray emission in white contours. The linear pixel range of the depicted X-ray emission is 0 to  $4 \times 10^{-7}$  photons  $\text{cm}^{-2} \text{s}^{-1} \text{pixel}^{-1}$ ; the X-ray emission has also been smoothed by a Gaussian with a radius of 1.5 arcseconds. The radio contours are at the same levels as those depicted in Figure 16. The locations of the X-ray source CXOU J171419.8–383023 (associated with the northwestern rim of the SNR) and CXOU J171428.5–383601 (the southern discrete hard X-ray source) are both indicated. Again, the crescent of radio emission seen to the east is the SNR G348.5–0.0. See Section 3.4.1.

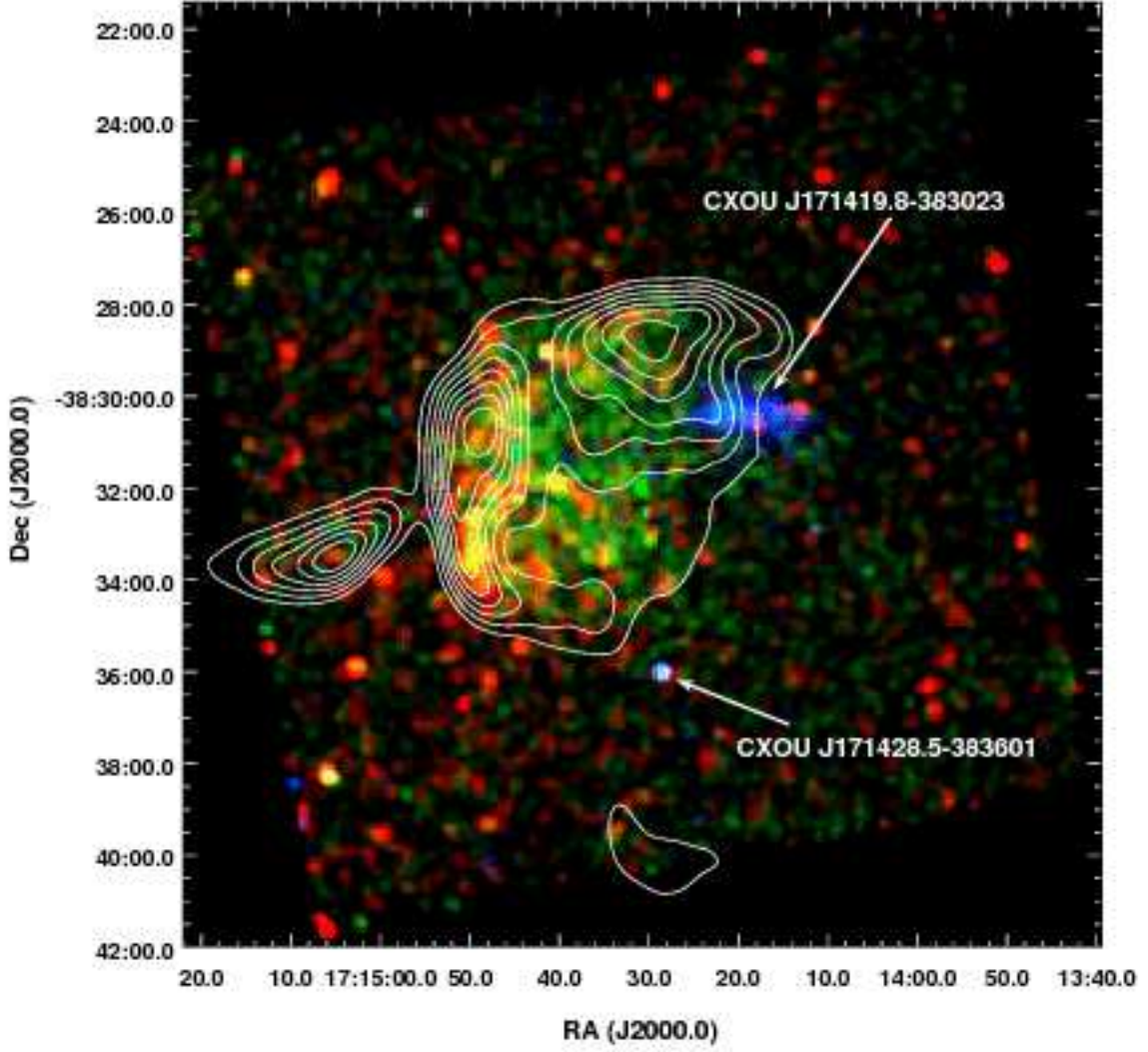


Fig. 20.— Three-color exposure-corrected and smoothed (with a Gaussian with a radius of 1.5 arcseconds) *Chandra* ACIS-I image of CTB 37A. This image has been made using monoenergetic exposure maps. Red, green and blue colors correspond to soft (0.5-1.5 keV), medium (1.5-2.5 keV) and hard (2.5-10.0 keV) emission, respectively. The linear pixel ranges of the depicted X-ray emission (in units of photons  $\text{cm}^{-2} \text{s}^{-1} \text{pixel}^{-1}$ ) are as follows:  $1 \times 10^{-8}$  to  $4 \times 10^{-8}$  for the soft emission,  $1 \times 10^{-8}$  to  $2 \times 10^{-7}$  for the medium emission and  $1 \times 10^{-9}$  to  $5 \times 10^{-9}$  for the hard emission. The white contours depict radio emission as observed with the MOST at a frequency of 843 MHz (the contour levels are the same as those depicted in Figure 19). The radio contours are at the level of 0.4, 0.6, 0.8, 1.0, 1.2, 1.4, 1.6, 1.8 and 2.0 Jy/beam. The locations of the X-ray source CXOU J171419.8–383023 (associated with the northwestern rim of the SNR) and CXOU J171428.5–383601 (the southern discrete hard X-ray source) are both indicated. Again, the crescent of radio emission seen to the east is the SNR G348.5–0.0. See Section 3.4.1.

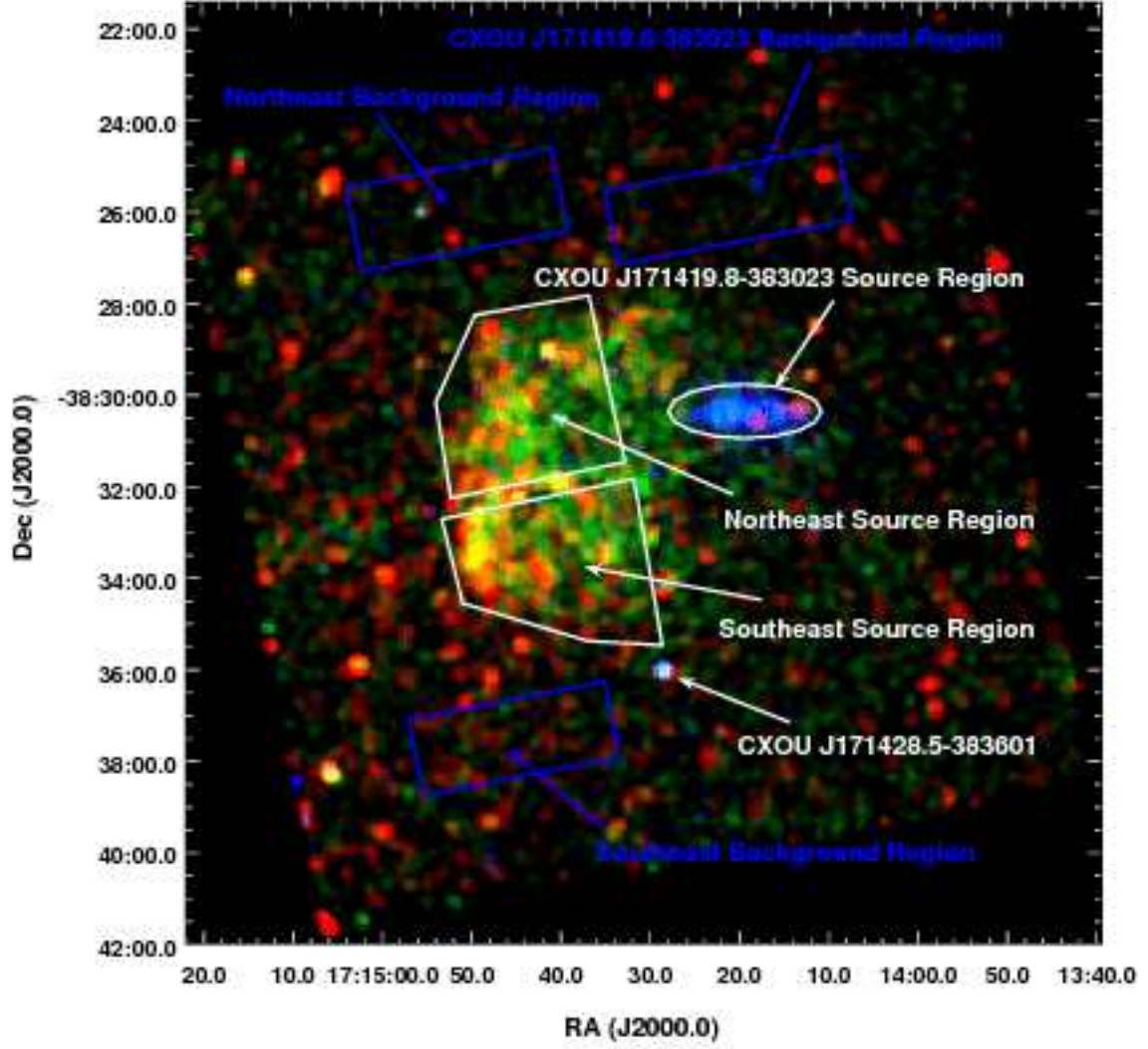


Fig. 21.— Same as Figure 20 but with the regions of spectral extraction indicated (source regions are depicted in white and background regions are depicted in blue). See Table 10 and Section 3.4.1.

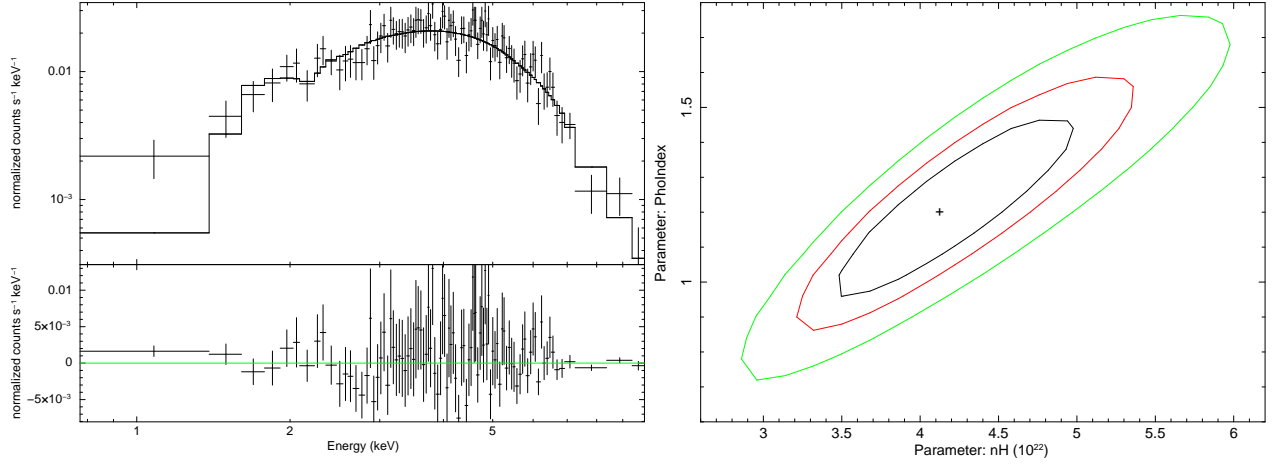


Fig. 22.— (left) *Chandra* ACIS-I spectrum of CXOU J171419.8-383023 as fit with a PHABS×POWER LAW model. (right) Confidence contour plot for column density  $N_H$  versus photon index  $\Gamma$ . See Table 10 and Section 3.4.1.

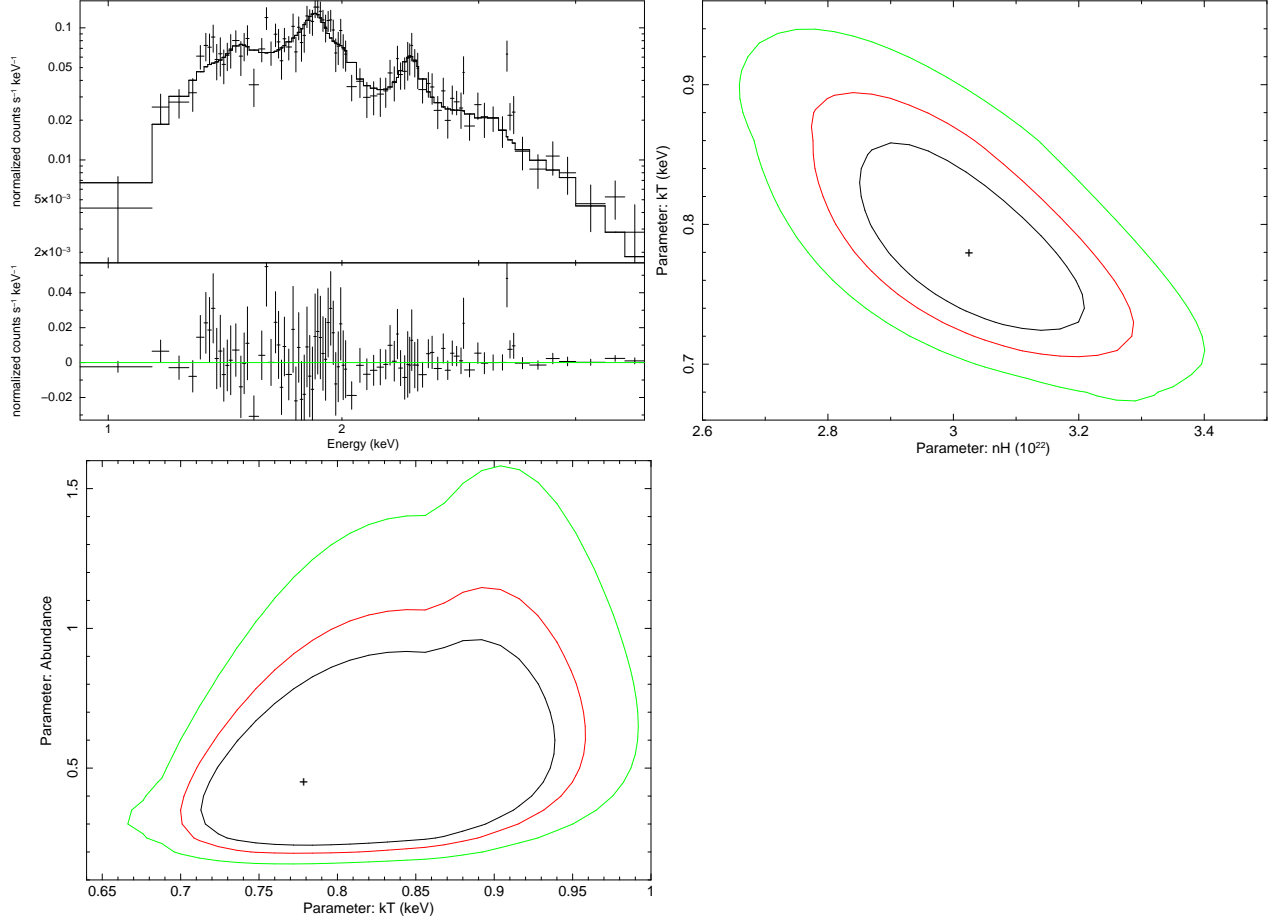


Fig. 23.— (top left) *Chandra* ACIS-I spectrum of the northeastern region of CTB 37A as fit with a PHABS×APEC model with variable abundance. (top right) Confidence contour plot for column density  $N_H$  versus temperature  $kT$ . See Table 10 and Section 3.4.1.

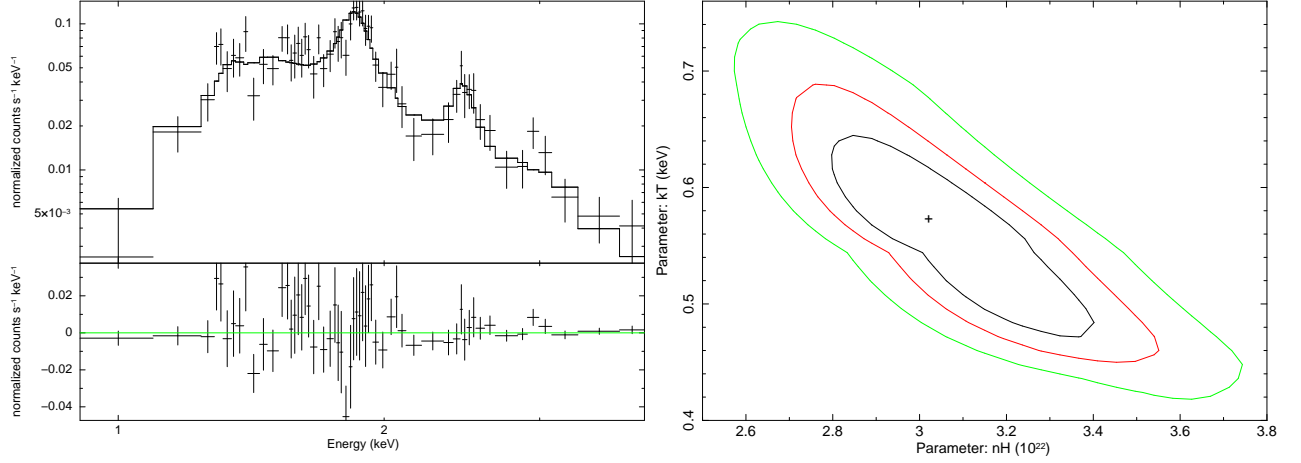


Fig. 24.— (left) *Chandra* ACIS-I spectrum of the southeastern region of CTB 37A as fit with a PHABS×APEC model. (right) Confidence contour plot for column density  $N_H$  versus temperature  $kT$ . See Table 10 and Section 3.4.1.

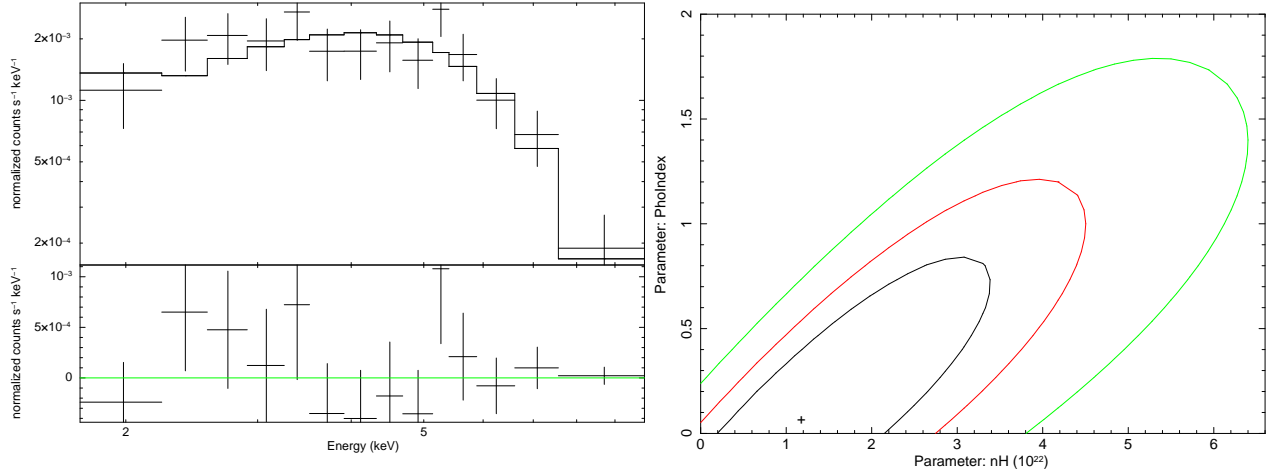


Fig. 25.— (left) Extracted ACIS-I spectrum of the hard source CXOU J171428.5–383601 – a discrete source seen toward the southern edge of the angular extent of CTB 37A – as fitted with a PHABS×Power Law model. (right) Confidence contour plot for the fit. See Section 3.4.1.



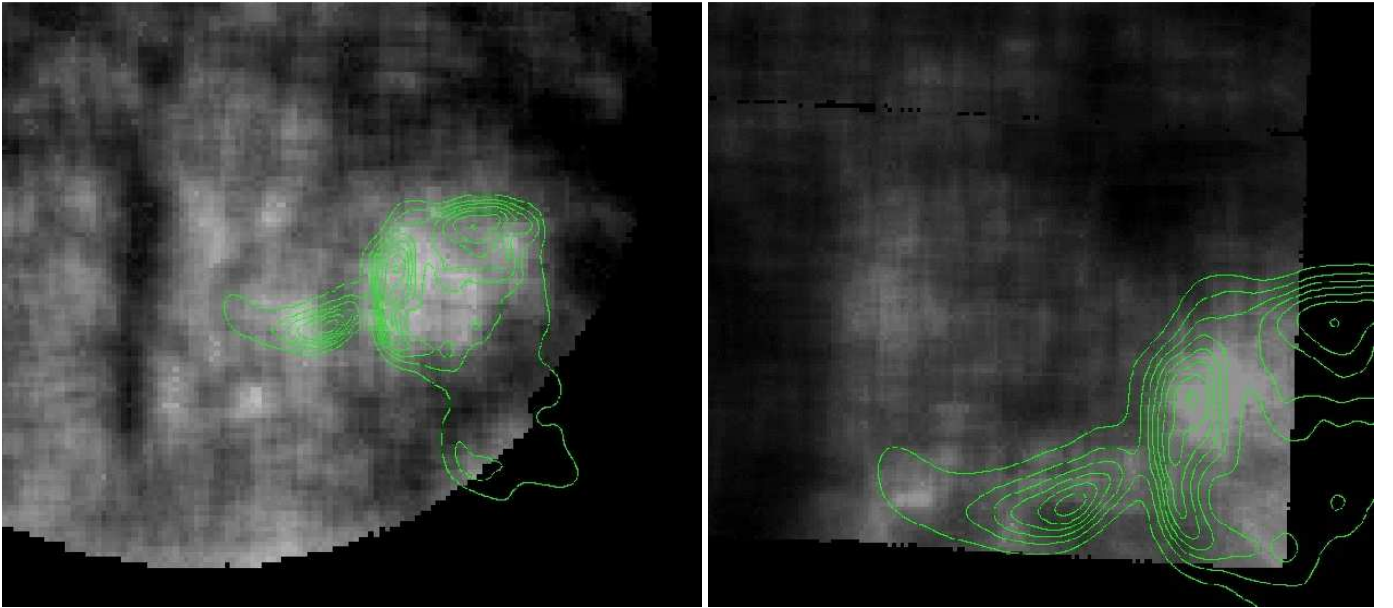


Fig. 26.— *ASCA* GIS (left) and SIS (right) images of CTB 37A and G348.5-0.0 with radio contours overlaid. The circular radio structure seen to the west is CTB 37A (which is visible in X-ray and radio) while the radio filament extending eastward (which lacks an X-ray counterpart) is G348.5-0.0. See Section 3.4.1.